Circuit-Quantum Electrodynamics (CQED) with Superconducting Flux Qubits

- Design and Fabrication of a Microwave Beam Splitter -

Andreas Emmert
Diploma Thesis

Advisor: Prof. Dr. R. Gross
Munich, the 21st of February 2006

TECHNISCHE UNIVERSITÄT MÜNCHEN

Abstract

The interaction of light and matter is a fundamental process in nature and has interested physicists at all times. In the field of Cavity Quantum Electrodynamics (CQED), the interaction of atoms with single photons – which define the quantized electromagnetic field – of a quantum mechanical resonator is investigated. Its constitutes an elegant method to investigate fundamentals in matter-light interaction.

The knowledge about the interaction between atoms and photons and its control is essential for the implementation of quantum information techniques as for example quantum communication and quantum information processing (QIP). In the past years, considerable progress has been achieved in quantum optics experiments. The problem of these implementations with respect to later applications in quantum information processing is scalability. Solid state based components could overcome this problem. Among the solid state realizations, superconducting Josephson devices are promising candidates as they are relatively independent from environmental noise because of three main reasons [1]: First, the superconducting ground state is separated and thus protected by an energy gap Δ of the order of meV from the quasiparticle excitation spectrum. Second, the superconducting state represents a macroscopic ground state. This makes it possible to design macroscopic quantum devices acting as artificial atoms whose properties can be almost arbitrarily determined by its design and fabrication parameters. And third, superconducting metals have a large electron density resulting in a short screening length to protect the system from perturbing screening charges.

In the present work, the design and fabrication of a superconducting hybrid ring as an solid state implementation of a quantum optical beamsplitter is presented, as well as measurements of its performance. The hybrid ring is the essential component of a detection scheme in the microwave regime capable to achieve a full state reconstruction of extremely weak quantum signals. In this sense, the detection scheme presented here is much more powerful than any classical amplification method. Used classically, the detection scheme presented in this work can also serve as a preamplification scheme using a local oscillator to directly overcome the noise floor of cold and even room temperature amplifiers.

The DFG (German Science Foundation) has set up a cooperative research center in Munich with the goal of developing solid-state based systems suitable for QIP. This work has been conducted within the scope of this research initiative (SFB 631).

Contents

Chapter 1

Introduction

1.1 Outline

In the first chapter, the motivation for this diploma thesis is given. The paper presented there will briefly explain how the hybrid ring - whose experimental realization was subject of this work - can be used as a microwave beam splitter. In this context, the hybrid ring is a central building block for a microwave quantum homodyning technique that hopefully enables the measurement of relevant observables of single photons and other weak quantum signals, realizing linear optics on a chip.

The second chapter is dedicated to the design of the hybrid ring. A general introduction to microwave engineering concepts for normal and superconducting materials is followed by a transmission line model of the hybrid ring, showing the working principle of such a MW device. As the hybrid ring is realized in a coplanar wave guide (CWG) design within this work, approximate formulas for the calculation of transmission line parameters of normal and superconducting CWGs are presented. This also includes the investigation of attenuation and dispersion. The content of this chapter allows the fast design of a hybrid ring made of CWG sections without using extensive numerical simulations.

The third chapter shows the possibilities, limitations and results of numerical simulations for the design of the hybrid ring made of CWG sections.

The fourth chapter will explain the fabrication of hybrid rings made out of niobium (Nb) on sapphire (Al_2O_3). Within this work, two different fabrication processes have been optimized. One process uses reactive ion etching (RIE), the other one is based on a lift-off process as the final step. The differences between these processes as well as their advantages and disadvantages will be pointed out.

The sixth chapter explains the measurement setup and results of the S-parameter measurements of a meander-like CWG transmission line and several hybrid rings down to a temperature of 4.2 K. There, also an outlook for future work on this topic is given.

At the end of this diploma thesis, a conclusion will be given.

1.2 Motivation

Quantum optics started in the microwave regime with the invention of the MASER, first established in 1954. With the rise of the LASER, the research interest in quantum optics concentrated on phenomena within the regime of visible light. Moreover, due to the smaller wavelength, experiments can be designed more compactly. Because of the energy of photons in the optical regime ($\lambda \approx 400 - 700$ nm) which corresponds to temperatures of $T = \hbar\omega/k_B \approx 2 \cdot 10^4$ K, experiments with microscopic quantum objects like single photons can be performed at room temperature. Microwave photons, however, with frequencies in the GHz-regime have energies that correspond to only ≈ 500 mK. Experiments on microscopic quantum effects thus have to be performed at cryogenic temperatures.

Recently however, research interest has been coming back to the microwave regime. This is also due to the present rise of interest in superconducting devices for quantum information processing. Superconducting quantum devices have energy levels that typically correspond to the microwave spectrum [1].

In the microwave regime, a lot of questions - especially related to the detection of quantum signals - are still not completely understood. Of course, a lot of theoretical methods can be applied developed for the optical regime. But there still exist important differences between microwave detection schemes and schemes used in the optical regime. Nevertheless, also in the microwave regime, the use of a beam splitter [2] seems to be indispensable for the detection of non-classical states. Therefore, within this work, a superconducting hybrid ring [3] was designed and fabricated that can serve as a beam splitter in the microwave regime . Moreover, prior to the *detection* of a microwave quantum signal, the signal has to be *generated* and guided to the detection scheme.

A proposal of a deterministic source of microwave single photons at the output of a superconducting resonator containing a flux qubit is presented in the following paper together with a *microwave quantum homodyning* detection scheme in which the superconducting hybrid ring acts as an on-chip microwave beam splitter. The proposal is submitted for publication. It constitutes the motivation for this diploma thesis. Experiments where a quantum object (in our case a radio-frequency superconducting quantum-interference device, RF SQUID) interacts with the quantized modes of a resonator (here, a superconducting CWG resonator) fall into the class of cavity quantum electrodynamics (CQED) experiments. If such experiments are realized in superconducting circuits, they belong to the subgroup of circuit CQED experiments.

Microwave Single Photons and Quantum Homodyning on a Chip

M. Mariantoni,[1, *] M.J. Storcz,[2] F.K. Wilhelm,[2] W.D. Oliver,[3]
A. Emmert,[1] A. Marx,[1] R. Gross,[1] H. Christ,[4] and E. Solano[4, 5]
[1] *Walther-Meissner-Institut, Bayerische Akademie der Wissenschaften, Walther-Meissner-Strasse 8, D-85748 Garching, Germany*
[2] *Department Physik, CeNS and ASC, LMU, Theresienstrasse 37, D-80333 München, Germany*
[3] *MIT Lincoln Laboratory, 244 Wood Street, Lexington, Massachussets 02420, USA*
[4] *Max-Planck Institute for Quantum Optics, Hans-Kopfermann-Strasse 1, D-85748 Garching, Germany*
[5] *Sección Física, Departamento de Ciencias, Pontificia Universidad Católica del Perú, Apartado 1761, Lima, Peru*

We propose the use of metastable flux-based qubits, coupled to superconductive resonators by means of a quantum-optical Raman excitation scheme, for the deterministic generation of stationary and propagating microwave single photons. We introduce also a suitable microwave quantum homodyning technique that enables the measurement of relevant observables of single photons and other weak quantum signals, realizing linear optics on a chip. These generation and measurement protocols are building blocks for the advent of quantum information in the field of circuit QED.

PACS numbers: 85.25.-j, 42.50.Pq, 42.50.Dv, 03.65.Wj

A two-level atom coupled to a single mode of a quantized electromagnetic field is arguably the most fundamental system exhibiting matter-radiation interplay. Their interaction, described by the Jaynes-Cummings (JC) model, arises naturally in the realm of cavity quantum electrodynamics (CQED) in the microwave [1] and optical domains [2]. There, a variety of nonclassical states (e.g., squeezed, Schrödinger cat, and Fock states [3]), among other important phenomena and applications (e.g., entanglement and quantum logic [4]), have been proposed and realized. Other physical systems, like trapped ions [5], can reproduce the JC dynamics and, consequently, exploit this analogy for similar purposes. The intracavity field in CQED and the motional field in trapped ions are typically detected through a suitable transfer of information to measurable atomic degrees of freedom [1, 5]. In the case of propagating fields, quantum homodyne detection [6], a technique requiring efficient photodetectors, can lead to quantum tomography [7].

Given its relevance for quantum communication, single-photon sources have been pursued in the optical domain [8, 9]. Recently, several CQED-related experiments have been performed in tunable, solid-state systems. Quantum dots in photonic band-gap structures have been used as single photon sources [10] and superconducting charge qubits [11] have been coupled to on-chip cavities [12, 13]. In addition, microwave squeezing with Josephson parametric amplifiers [14] and aspects of the quantum-statistical nature of GHz photons in mesoscopic conductors have been demonstrated [15].

In this Letter, we propose the implementation of a deterministic source of microwave single photons, or linear superpositions of them, at the output of a superconducting resonator containing a flux qubit. A Raman-like scheme [16] determines the coupling between the cavity and the qubit, consisting of two metastable states of a three-level system in a Λ-type configuration [17]. Furthermore, we show that these weak quantum signals can be measured by means of a suitably designed technique: *microwave quantum homodyning* (MQH). It is based on a superconducting hybrid ring [18] acting as an on-chip *microwave beam splitter* (MBS), and a measurement device consisting of quantum linear amplification plus power read-out (no microwave photodetector is available yet). The generation of propagating microwave quantum weak signals and an appropriate measurement apparatus represent building blocks to establish on-chip quantum information transfer between qubits.

A prototypical example of a flux-based quantum circuit is the radio-frequency (RF) superconducting quantum-interference device (SQUID) [19], whose Hamiltonian is

$$\hat{H}_{\mathrm{S}} = \frac{\hat{Q}^2}{2C_{\mathrm{j}}} + \frac{(\hat{\Phi}-\Phi_{\mathrm{x}})^2}{2L_{\mathrm{s}}} - E_{\mathrm{J}} \cos\left(2\pi\frac{\hat{\Phi}}{\Phi_0}\right), \quad (1)$$

where $\hat{Q}$ is the charge stored on the junction capacitor C_{j}, $\hat{\Phi}$ is the total flux threading the loop (with $[\hat{\Phi},\hat{Q}]=i\hbar$), Φ_{x} is an externally applied quasi-static flux bias, L_{s} is the self-inductance of the loop, $E_{\mathrm{J}} \equiv I_{\mathrm{c0}}\Phi_0/2\pi$ is the Josephson coupling energy, I_{c0} is the junction critical current, and $\Phi_0 = h/2e$ is the flux quantum. For appropriate design parameters, and close to half-integer values of Φ_{x}/Φ_0, the RF SQUID potential profile becomes a relatively shallow double well whose asymmetry can be tuned by setting Φ_{x} (see Fig. 1). In this case, the two lowest eigenstates $|\mathrm{g}\rangle$ and $|\mathrm{e}\rangle$ are metastable and localized in the left and right wells, respectively, whereas the excited state $|\mathrm{h}\rangle$ is delocalized with energy above the barrier. As will be shown later, these levels are suitable for implementing a Raman excitation scheme. The energy levels can be tuned by statically biasing Φ_{x} during the experiment, and transitions between states are driven by pulsed ac excitations. Other flux-based devices can also be used for the purposes of this work, for instance, persistent-

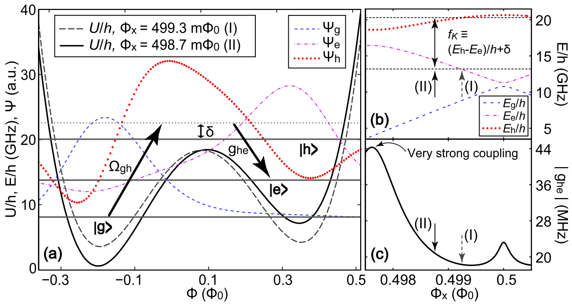

FIG. 1: (Color online) (a) Potential profile of the RF SQUID for two distinct values of Φ_x [(I) and (II)] and wave functions for the first three lowest energy levels ($|\mathrm{g}\rangle$, $|\mathrm{e}\rangle$, and $|\mathrm{h}\rangle$). Parameters are given in Table I. The Raman scheme is indicated with arrows. (b) RF SQUID energy-band diagram near $\Phi_0/2$ plotted vs. Φ_x. Zero detuning case, point (I), and large detuning case, point (II). (c) Absolute value of the vacuum Rabi frequency g_he as a function of Φ_x. The coupling reaches 40 MHz at the anticrossing between levels $|\mathrm{e}\rangle$ and $|\mathrm{h}\rangle$.

current (PC) qubits [20], which have been demonstrated to possess relatively large excited-state lifetimes [21].

The segment of superconducting coplanar waveguide (CWG) shown in Figs. 2 (a), (b), and (d) is one realization of a transmission line resonator. Such a resonator is characterized by eigenenergies with transition angular frequencies ω_k that are much larger than the thermal energy at cryogenic temperatures. Its Hamiltonian is $\hat{H}_\mathrm{C} = \sum_k \hbar\omega_k \left(\hat{a}_k^\dagger \hat{a}_k + 1/2\right)$, where $\hat{a}_k^\dagger$ and $\hat{a}_k$ are the bosonic creation and annihilation operators for mode k. Voltage and current, corresponding to electric and magnetic fields, respectively, are conjugate operators associated with the quantized resonator, $\hat{I}_\mathrm{C}(z,t) = (\partial/\partial t)\,\hat{\vartheta}(z,t)$, where z is the spatial coordinate for the superconducting inner strip and $\hat{\vartheta}(z,t)$ is the normal mode expansion of the cavity field. The vacuum rms current of a single mode $k = K$ of the cavity is $I^0_{\mathrm{c},K}(z) = \sqrt{\hbar\omega_K/2(Dl)}\ \left|\sin(2\pi z/D - K\pi/2)\right|$. Here, D is the length of the resonator and l is its total series inductance per unit length. The cavity is chosen to be a $\lambda/2$ open-circuited resonator operated at the second mode, $K = 2$, and coupled capacitively to a CWG transmission line. Such a cavity can reach external quality factors $Q_\mathrm{x} = 10^4$ at $f_K = \omega_K/2\pi \approx 10$ GHz [12], corresponding to a cavity decay rate $\kappa_\mathrm{c}/2\pi \approx 1$ MHz. Hence, at temperature $T_\mathrm{b} \approx 50$ mK, the mean number of thermal photons $\langle n_\mathrm{th}\rangle = [\exp(\hbar\omega_K/k_\mathrm{B}T_\mathrm{b}) - 1]^{-1} \approx 10^{-4}$ and the cavity mode can be considered in the vacuum state $|0\rangle$.

Embedding the RF SQUID in the CWG resonator [see Figs. 2 (a), (b) and (c)] allows a strong, inductive coupling between any two levels of the RF SQUID and the single cavity mode K. The resulting interaction Hamiltonian is $\hat{H}_\mathrm{I} = -M_\mathrm{cs}\hat{I}_{\mathrm{c},K}\hat{I}_\mathrm{s}$, where $\hat{I}_{\mathrm{c},K}$ and $\hat{I}_\mathrm{s}$ are resonator and RF SQUID current operators, respectively, and M_cs is their mutual inductance. Explicitly, we find

$$\hat{H}_\mathrm{I} \;=\; -\,(M_\mathrm{cs}/L_\mathrm{s})\, I^0_{\mathrm{c},K}(z)\; (\hat{\Phi} - \Phi_\mathrm{x})\; i\,[\hat{a}_K^\dagger(t) - \hat{a}_K(t)]. \quad (2)$$

The RF SQUID can be positioned near one of the antinodes of the vacuum current [Fig. 2 (a)] and can be biased to yield maximum coupling for any two of its eigenstates $|i\rangle$ and $|j\rangle$. The interaction matrix element between these levels represents their coupling strength with mode K and it is used to define the vacuum Rabi frequency $g_{ij} = -(M_\mathrm{cs}/L_\mathrm{s}) I^0_{\mathrm{c},K}(z)\langle i|\hat{\Phi}|j\rangle/h$. Moreover, when operating the system in the dispersive regime, the corresponding lifetimes become strongly enhanced and an effective decay rate $\gamma_{ij}^\mathrm{eff} \le \kappa_\mathrm{c} f_K^2 g_{ij}^2/(\delta_\mathrm{tr}^4)$ can be assumed, where $\delta_\mathrm{tr} \gg (\kappa_\mathrm{c}/2\pi)$ is the detuning between mode K and the transition under consideration. The coupling g_he, the effective decay rate $\gamma_\mathrm{he}^\mathrm{eff}/2\pi$, and other relevant quantities have been calculated for both RF SQUIDs and PC qubits and typical results are reported in Table I.

A main application of the system illustrated above is the generation of single photons at frequency f_K in a manner similar to a quantum-optical Raman scheme [9, 16]. After preparing the RF SQUID in level $|\mathrm{g}\rangle$, the transition $|\mathrm{g}\rangle \leftrightarrow |\mathrm{h}\rangle$ is driven by a classical excitation with Rabi frequency Ω_gh and detuned by the amount δ. The same transition is detuned from the resonator mode K by an amount $\Delta \gg \delta$, resulting in a comparatively negligible coupling. On the other hand, the $|\mathrm{h}\rangle \leftrightarrow |\mathrm{e}\rangle$ transition is the only one coupled to mode K, and it is also detuned by δ [see Figs. 1 (a) and (b)]. Choosing $\delta \gg \max\,[\Omega_\mathrm{gh}, g_\mathrm{he}]$, level $|\mathrm{h}\rangle$ can be adiabatically eliminated [9, 16], thus leading to the effective second-order Hamiltonian

$$\begin{aligned}\hat{H}_\mathrm{eff} \;&=\; \hbar\frac{\Omega_\mathrm{gh}^2}{\delta}|\mathrm{g}\rangle\langle\mathrm{g}| + \hbar\frac{g_\mathrm{he}^2}{\delta}|\mathrm{e}\rangle\langle\mathrm{e}|\hat{a}_K^\dagger\hat{a}_K + \\ &\quad + \hbar g_\mathrm{eff}\left(|\mathrm{g}\rangle\langle\mathrm{e}|\hat{a}_K + |\mathrm{e}\rangle\langle\mathrm{g}|\hat{a}_K^\dagger\right), \qquad (3)\end{aligned}$$

where $g_\mathrm{eff} = (\Omega_\mathrm{gh}/\delta) g_\mathrm{he}$ is the effective Raman coupling. The first two terms at the r.h.s. of Eq. (3) are ac Zeeman shifts, while the last term describes an effective anti-JC dynamics, inducing transitions within the $\{|\mathrm{g}\rangle|n\rangle, |\mathrm{e}\rangle|n+1\rangle\}$ subspaces. The ac Zeeman shifts associated with the transition of interest, $\{|\mathrm{g}\rangle|0\rangle, |\mathrm{e}\rangle|1\rangle\}$, can be compensated by retuning the classical driving frequency. When the strong-coupling regime is reached, $g_\mathrm{eff} \gtrsim \max\left[\kappa_\mathrm{c}/2\pi, \gamma_\mathrm{he}^\mathrm{eff}/2\pi\right]$, an effective π-pulse realizes a complete transfer of population from state $|\mathrm{g}\rangle|0\rangle$ to state $|\mathrm{e}\rangle|1\rangle$. This process leads to the creation of a microwave Fock state $|1\rangle$ inside the resonator that will leak out in a time $\sim 2\pi/\kappa_\mathrm{c}$. Alternatively, in the case of weak-coupling, the photon leaks to the outer world as soon as it is generated inside the cavity, thereby realizing a deterministic single-photon source. Tailoring the photon pulse shape would require a time-dependent classical driving $\Omega_\mathrm{gh}(t)$ [9].

Note that the proposed Raman scheme can produce single photons without initialization of the qubit in the excited state $|\mathrm{e}\rangle$ ($|\mathrm{g}\rangle|0\rangle$ is not a dark state of the anti-JC dynamics). Raman pulses are fast and exploit the well defined qubit-resonator coupling [9], while STIRAP techniques are slow (adiabatic) and, nevertheless, useful when relative insensitivity to coupling fluctuations is required [8]. The so-generated single photons can be guided through superconducting CWGs and transferred over appreciable distances, even beyond the few centimeters required for on-chip quantum communication.

If the initial qubit-cavity state is $(\cos\theta|\mathrm{g}\rangle + e^{i\phi}\sin\theta|\mathrm{e}\rangle)|0\rangle$, then, the above Raman π-pulse would map it on the cavity field ($|\mathrm{e}\rangle|0\rangle$ is a dark state of the anti-JC dynamics). In this way, we would produce an outgoing field state $\cos\theta|1\rangle + e^{i\phi}\sin\theta|0\rangle$, whose coherent properties we would want to observe.

Measurement schemes based on classical homodyning [18] are insufficient to resolve nonclassical field states. On the other hand, microwave single-photon detectors in mesoscopic systems do not exist to our knowledge. Here, we propose an on-chip MQH technique, able to measure relevant observables of weak quantum signals even at the level of single photons. It can be implemented in three main steps. First, at cryogenic temperatures, a signal (S) and a local oscillator (LO), characterized by the same angular frequency $\omega_{\mathrm{S}} = \omega_{\mathrm{LO}}$, are coherently superposed at a suitably designed MBS [Fig. 2 (a)]. Second, the microwave fields at the MBS outports are amplified at low temperatures (at this point, mixers and square-law detectors at room temperature may be also used). Finally, the output DC voltages, proportional to the powers P_{d} of the input signals, are measured with an oscilloscope. Adequate manipulation of these measurements will lead to signal information with minimal noise nuisance.

TABLE I: Typical parameters and calculated relevant quantities for the RF SQUID ($\Phi_{\mathrm{x}} = 0.499\ \Phi_0$) and the PC qubit ($\Phi_{\mathrm{x}} = 0.480\ \Phi_0$, $\alpha = 0.8$), coupled to a 50 Ω resonator [22].

	I_{c0} (μA)	C_{j} (fF)	L_{s} (pH)	M_{cs} (pH)	$\frac{\Delta E_{\mathrm{eh}}}{h}$ (GHz)	$I^0_{\mathrm{c},2}$ (nA)	$\lvert g_{\mathrm{he}}\rvert$ (MHz)	$\frac{\gamma^{\mathrm{eff}}_{\mathrm{he}}}{2\pi}$ (kHz)
RF SQUID	1.4	100	266	22	6.2	16.1	20	9.5
PC qubit	0.6	7	10	1	6	16.2	5.7	106.4

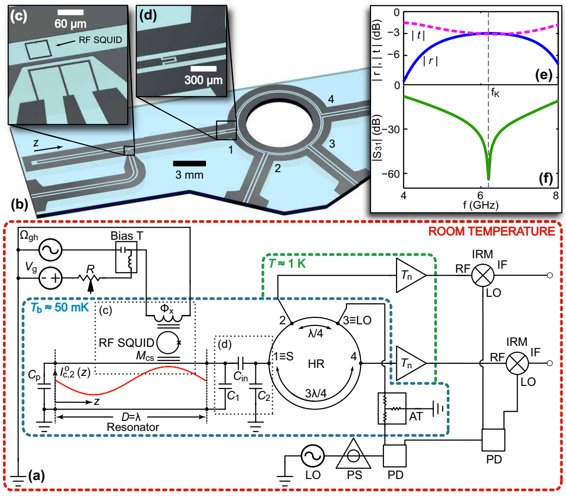

FIG. 2: (Color online) (a) Sketch of the entire generation and detection network (C_{in}, C_1, and C_2: capacitive Π network representing the resonator input port; C_{p}: parasitic capacitor at the cavity open-circuit ending; HR: hybrid ring; PS: phase shifter; PD: power divider; AT: attenuator). (b) Asymmetric CWG resonator with integrated HR. (c) On-chip antenna providing the classical driving Ω_{gh}. (d) Resonator-CWG coupling region. (e) The waves traveling around the HR interfere resulting in the plotted reflection and transmission amplitude patterns. (f) Isolation between ports three and one of the HR.

The MBS is realized using a superconducting four-port device: the hybrid ring, depicted in Fig. 2 (a). The advantageous coplanar design proposed here can be easily scaled and integrated with resonators in monolithic circuits that can be fabricated with Nb technology [see Fig. 2 (b)]. We now extend the classical theory of hybrid rings in Ref. [18] to the quantum regime by analogy with an optical beam splitter. With only the vacuum incident at ports two and four, and up to a global phase common to both input beams, the reduced quantum input-output relations of a (superconducting) lossless MBS are

$$\begin{bmatrix} \hat{a}_2 \\ \hat{a}_4 \end{bmatrix} = \begin{bmatrix} r & t \\ -t^* & r^* \end{bmatrix} \begin{bmatrix} \hat{a}_{\mathrm{S}} \\ \hat{a}_{\mathrm{LO}} \end{bmatrix}, \tag{4}$$

where r and t are the complex, frequency-dependent reflection and transmission coefficients, $\hat{a}_{\mathrm{S}}$ and $\hat{a}_{\mathrm{LO}}$ are the signal and LO port operators, respectively. The latter is chosen to be a classical coherent field which is characterized by its complex amplitude $\alpha_{\mathrm{LO}} = |\alpha_{\mathrm{LO}}|\exp(i\theta_{\mathrm{r}})$ [3], where $|\alpha_{\mathrm{LO}}|$ is the norm of the field amplitude and θ_{r} its relative phase with respect to S. The numerical simulations plotted in Fig. 2 (e) show that the MBS can be *balanced* over a broad bandwidth around the desired operation frequency f_K, i.e., $r = t = 1/\sqrt{2}$ (−3 dB), producing $\hat{a}_2 = (\hat{a}_S + \hat{a}_{\mathrm{LO}})/\sqrt{2}$ and $\hat{a}_4 = (-\hat{a}_S + \hat{a}_{\mathrm{LO}})/\sqrt{2}$.

At this point, standard optical quantum homodyning recommends the use of photodetectors to measure realizations of power P at each outport, proportional to realizations N of observable $\hat{n} = \hat{a}^\dagger\hat{a}$. After subtracting them, $P_{\mathrm{d},2} - P_{\mathrm{d},4} \propto N_2 - N_4 = 2|\alpha_{\mathrm{LO}}|X_{\theta_{\mathrm{r}}}$, where LO operators were replaced by their complex amplitudes, realizations of the quadrature $\hat{X}_{\theta_{\mathrm{r}}} \equiv (\hat{a}^\dagger_{\mathrm{S}}e^{i\theta_{\mathrm{r}}} + \hat{a}_{\mathrm{S}}e^{-i\theta_{\mathrm{r}}})/2$, amplified by a factor $2|\alpha_{\mathrm{LO}}|$, are obtained. Typically, the detector noise floor can be overcome by increasing the LO voltages. With the complete histogram of these measurements, averages $\langle\hat{X}^p_{\theta_{\mathrm{r}}}\rangle$, $\forall p$, and even full reconstruction of the associated Wigner function via quantum tomography [6], could be calculated. Unfortunately, microwave photodetectors, to our knowledge, are not available. Moreover, the MBS outport signals may need to cross linear amplifiers, mixers, and square-law detectors, in that order, before their voltage is measured at the oscilloscope. These conditions impose severe restrictions in the measurement process, mainly in terms of added noise in the linear amplification process [15, 23], requiring additional and specific theoretical considerations.

The output signals of the linear amplification can be written [23], referred to the input, as $\hat{X}_{\tilde{a}_2} = \hat{X}_{a_2} + \hat{X}_{\xi_2}$ and $\hat{X}_{\tilde{a}_4} = \hat{X}_{a_4} + \hat{X}_{\xi_4}$, where $\hat{X}_a \equiv (\hat{a} + \hat{a}^\dagger)/2$ and $\hat{X}_\xi \equiv (\hat{\xi} + \hat{\xi}^\dagger)/2$. The noise at each arm is uncorrelated from the other, and is characterized by (almost) the same noise temperature T_n, leading to a mean photon number $\langle \hat{n}_\xi \rangle = \langle \hat{\xi}^\dagger \hat{\xi} \rangle = k_\mathrm{B} T_\mathrm{n} / \hbar\omega_K$. Subtracting the powers, read with the oscilloscope after the square-law detectors, we measure realizations of the following observable

$$\begin{aligned}\hat{\tilde{a}}_2^\dagger \hat{\tilde{a}}_2 - \hat{\tilde{a}}_4^\dagger \hat{\tilde{a}}_4 = {} & \hat{a}_S^\dagger \hat{a}_\mathrm{LO} + \hat{a}_\mathrm{LO}^\dagger \hat{a}_S + \hat{\xi}_2^\dagger \hat{\xi}_2 - \hat{\xi}_4^\dagger \hat{\xi}_4 \\ & + \hat{\xi}_2^\dagger \frac{(\hat{a}_S + \hat{a}_\mathrm{LO})}{\sqrt{2}} + \hat{\xi}_2 \frac{(\hat{a}_S^\dagger + \hat{a}_\mathrm{LO}^\dagger)}{\sqrt{2}} \\ & + \hat{\xi}_4^\dagger \frac{(-\hat{a}_S + \hat{a}_\mathrm{LO})}{\sqrt{2}} + \hat{\xi}_4 \frac{(-\hat{a}_S^\dagger + \hat{a}_\mathrm{LO}^\dagger)}{\sqrt{2}}. \quad (5)\end{aligned}$$

If we repeat the measurement procedure, we can average

$$\langle \hat{\tilde{a}}_2^\dagger \hat{\tilde{a}}_2 - \hat{\tilde{a}}_4^\dagger \hat{\tilde{a}}_4 \rangle = 2|\alpha_\mathrm{LO}| \langle \hat{X}_{\theta_\mathrm{r}} \rangle, \tag{6}$$

given that $\langle \hat{\xi}_2 \rangle = \langle \hat{\xi}_4 \rangle = 0$ and the reasonable assumption $\langle \hat{n}_{\xi_2} \rangle \sim \langle \hat{n}_{\xi_4} \rangle$. Eq. (6) shows that the proposed MQH allows us to measure the amplified mean value of the quadrature $\hat{X}_{\theta_\mathrm{r}}$ with *negligible noise disturbance.* This important physical quantity realizes a phase-sensitive measurement: it is zero for any Fock state $|n\rangle$ and $\cos\theta_\mathrm{r}/2$ for the superposition $(|0\rangle + |1\rangle)/\sqrt{2}$. However, a straightforward extension of optical homodyning methods does not lead to a measurement of $\langle \hat{X}_{\theta_\mathrm{r}}^2 \rangle$. In our case, the amplifiers noise shadows the information contained in the signal. Instead, we propose to send both MBS outports through mixers using the same calibrated local oscillator, and then calculate the product average

$$\langle \hat{\tilde{X}}_{a_2,\theta_\mathrm{r}} \hat{\tilde{X}}_{a_4,\theta_\mathrm{r}} \rangle = -\frac{1}{2} \langle \hat{X}_{\theta_\mathrm{r}}^2 \rangle + \frac{1}{2} \langle \hat{X}_{\mathrm{LO},\theta_\mathrm{r}}^2 \rangle. \tag{7}$$

Here, expressions $\langle \hat{X}_{\xi_2} \hat{X}_{\xi_4} \rangle = \langle \hat{X}_{\xi_2} \rangle \langle \hat{X}_{\xi_4} \rangle = 0$ were used, and $\langle \hat{X}_\mathrm{LO}^2 \rangle$ is assumed to be known via calibration of the local oscillator. Eq. (7) shows a remarkably simple way of measuring $\langle \hat{X}_{\theta_\mathrm{r}}^2 \rangle$ with *minimal noise disturbance.* It is important to mention that, for the sake of our calculations, we have considered a full quantum description of mixers and square-law detectors [24].

A precise measurement of $\langle \hat{X}_{\theta_\mathrm{r}} \rangle$ and $\langle \hat{X}_{\theta_\mathrm{r}}^2 \rangle$, as shown in Eqs. (6) and (7), require random and uncorrelated noise, enough number of repetition measurements, and that the difference of $\langle \hat{n}_\xi \rangle$ ($\sim$ 20 around 10 K) for both amplification arms is sufficiently small. It is known that the knowledge of $\langle \hat{X}_{\theta_\mathrm{r}} \rangle$ and $\langle \hat{X}_{\theta_\mathrm{r}}^2 \rangle$ provides us with complete information about a Gaussian state, and a simple criterion for discriminating Fock states. Furthermore, we conjecture here on the possibility of measuring $\langle \hat{X}_{\theta_\mathrm{r}}^p \rangle$, $\forall p$, $\forall \theta_\mathrm{r}$, under the conditions described above [25]. This result would show that a complete reconstruction of the Wigner function through quantum homodyne tomography is possible.

In conclusion, we proposed a new scheme for the deterministic generation of intracavity and propagating microwave single photons or linear superpositions of them. We showed also how to realize MQH for measuring first and second-order field quadrature moments. These proposals are essential tools for the implementation of quantum-optical CQED and linear optics in the microwave domain on a chip. Moreover, they represent an important step for the advent of quantum information in the field of circuit QED [26].

The authors would like to acknowledge K. R. Brown and D. E. Oates for fruitful discussions. MM and WDO thank T. P. Orlando and M. Gouker for their support during the early stages of this work. This work has been partially supported by the DFG through SFB 631. ES acknowledges EU support through RESQ project.

---

[*] Electronic address: `Matteo.Mariantoni@wmi.badw.de`

[1] J.M. Raimond, M. Brune, and S. Haroche, Rev. Mod. Phys. **73**, 565 (2001).
[2] H. Mabuchi and A.C. Doherty, Science **298**, 1372 (2002).
[3] *Theory of Nonclassical States of Light*, edited by V.V. Dodonov and V.I. Man'ko (Taylor & Francis, London, 2003).
[4] M.A. Nielsen and I.L. Chuang, *Quantum Computation and Quantum Information*, (Cambridge University Press, Cambridge, 2000).
[5] D. Leibfried, R. Blatt, C. Monroe, and D. Wineland, Rev. Mod. Phys. **75**, 281 (2003).
[6] U. Leonhardt, *Measuring the Quantum State of Light* (Cambridge University Press, Cambridge, 1997).
[7] A.I. Lvovsky *et al.*, Phys. Rev. Lett. **87**, 050402 (2001).
[8] A. Kuhn, M. Hennrich, and G. Rempe, Phys. Rev. Lett. **89**, 067901 (2002).
[9] M. Keller *et al.*, Nature **431**, 1075 (2004).
[10] A. Badolato *et al.*, Science **308**, 1158 (2005).
[11] Y. Makhlin, G. Schön, and A. Shnirman, Rev. Mod. Phys. **73**, 357 (2001).
[12] A. Wallraff *et al.*, Nature **431**, 162 (2004).
[13] I. Chiorescu, P. Bertet, K. Semba, Y. Nakamura, C.J.P.M. Harmans, and J.E. Mooij, Nature **431**, 159 (2004).
[14] R. Movshovich *et al.*, Phys. Rev. Lett. **65**, 1419 (1990).
[15] J. Gabelli *et al.*, Phys. Rev. Lett. **93**, 056801 (2004).
[16] M. França Santos, E. Solano, and R.L. de Matos Filho, Phys. Rev. Lett. **87**, 093601 (2001).

[17] J. Siewert *et al.*, e-print cond-mat/0509735.
[18] R.E. Collin, *Foundations for Microwave Engineering*, 2nd ed. (Wiley-IEEE Press, New Jersey, 2000).
[19] J.R. Friedman *et al.*, Nature **406**, 43 (2000).
[20] C.H. van der Wal *et al.*, Science **290**, 773 (2000).
[21] Y. Yu *et al.*, Phys. Rev. Lett. **92**, 117904 (2004).
[22] E.g., conductor width $W = 118\ \mu$m, slot $S = 80\ \mu$m, capacitance and inductance per unit length $c \approx 0.17$ nFm^{-1} and $l \approx 435$ nHm^{-1}, resp., and length $D \approx 18.4$ mm.
[23] C. M. Caves, Phys. Rev. D **26**, 1817 (1982).
[24] G. Giedke, M. Mariantoni, W.D. Oliver, H. Christ, and E. Solano, in preparation.
[25] W.D. Oliver, M. Mariantoni, H. Christ, and E. Solano, in preparation.
[26] J.Q. You and F. Nori, Phys. Rev. B **68**, 064509 (2003).

Chapter 2

Design of the Superconducting Hybrid Ring

2.1 Introduction

It is well known that microwave problems are governed by the Maxwell equations. They are commonly solved to design microwave components by aid of a so called field analysis. Analytical solutions of the full Maxwell equations are limited to very simple problems. For more complex applications the Maxwell equations are either solved numerically or simplified by problem dependent assumptions. The latter approach provides equations that can often be solved analytically. Most of these approaches are based on a dimensional analysis of the characteristic length scales of the electromagnetic waves and the geometry of the microwave component

One example is elementary circuit theory, where problems are solved by applying Kirchhoff's rules. This theory is applicable when the wavelength is much larger than the device structure. The other extreme is the field of geometrical optics, where the wavelength is much smaller then the structures interacting with the electromagnetic radiation.
In the field of microwave engineering, one often has to deal with problems which are in between these extrema since one has to deal with frequencies in the GHz regime, resulting in wavelengths in the vacuum of approximately

$$\lambda = \frac{c}{f} = \frac{3 \cdot 10^8\,\mathrm{m/s}}{10\,\mathrm{GHz}} = 3\,\mathrm{cm}.$$

which is of the order of magnitude of the microwave components treated within this work.
The *transmission line theory* is an often used instrument to gain basic insight into the behaviour of microwave components. As the hybrid ring is a component that works in this critical regime, it will firstly described using transmission line theory, which is independent from the technological realisation.
Secondly the concrete realisation of the hybrid ring by a coplanar waveguide (CWG) technique are discussed. There, the basic properties of CWGs will be presented.
In the end of this chapter, results of numerical simulations performed with commercial tools are presented.

2.2 Basic Microwave Engineering Concepts

Before applying the transmission line theory to the hybrid ring, the main ideas of this theory will be introduced in this section.

2.2.1 Maxwell's Equations

Electric and magnetic phenomena at the macroscopic level can be described by the Maxwell equations. Their differential form:

$$\begin{aligned}
\nabla \times \vec{\mathcal{E}} &= \frac{-\partial \vec{\mathcal{B}}}{\partial t} - \vec{\mathcal{M}}, & (2.1)\\
\nabla \times \vec{\mathcal{H}} &= \frac{\partial \vec{\mathcal{D}}}{\partial t} + \vec{\mathcal{J}}, & (2.2)\\
\nabla \cdot \vec{\mathcal{D}} &= \rho, & (2.3)\\
\nabla \cdot \vec{\mathcal{B}} &= 0. & (2.4)
\end{aligned}$$

The script quantities are time-varying vector fields and are real functions of the spatial coordinates x, y, z and the time t. These quantities are defined as:

$\vec{\mathcal{E}}$	is the electric field amplitude in [V/m]
$\vec{\mathcal{H}}$	is the magnetic field amplitude in [A/m]
$\vec{\mathcal{D}}$	is the electric flux density in [C/m^2]
$\vec{\mathcal{B}}$	is the magnetic flux density in [Wb/m^2]
$\vec{\mathcal{M}}$	is the fictitious magnetic current density in [V/m^2]
$\vec{\mathcal{J}}$	is the electric current density in [A/m^2]
ρ	is the electric charge density in [C/m^3]

Assuming a harmonic time dependence $e^{j\omega t}$, the electric field can be expressed in the form:

$$\vec{\mathcal{E}}(x,y,z,t) = \Re\left(\vec{E}(x,y,z)e^{j\omega t}\right) \quad (2.5)$$

with the phasor $\vec{E}(x,y,z) = \hat{x}E_1 e^{j\Phi_1} + \hat{y}E_2 e^{j\Phi_2} + \hat{z}E_3 e^{j\Phi_3}$. If one substitutes (2.5) into (2.1)-(2.2) Maxwell's equations in the phasor form become

$$\begin{aligned}
\nabla \times \vec{E} &= -j\omega\vec{B} - \vec{M}, & (2.6)\\
\nabla \times \vec{H} &= j\omega\vec{D} + \vec{J}, & (2.7)\\
\nabla \cdot \vec{D} &= \rho, & (2.8)\\
\nabla \cdot \vec{B} &= 0. & (2.9)
\end{aligned}$$

These equations are complemented by material equations which relate the flux densities to the field amplitudes. In a linear medium, the electric polarisation is linearly related to the applied field such as

$$\vec{P_e} = \varepsilon_0 \chi_e \vec{E}, \quad (2.10)$$

where χ_e is called the electric susceptibility. This leads to an electric flux density of

$$\vec{D} = \varepsilon_0\vec{E} + \vec{P_e} = \varepsilon_0(1 + \chi_e)\vec{E} = \varepsilon\vec{E}, \quad (2.11)$$

where

$$\varepsilon = \varepsilon' - j\varepsilon'' = \varepsilon_0(1 + \chi_e) \tag{2.12}$$

is the complex permittivity of the medium. The imaginary part of ε is responsible for dielectric damping of propagating waves.

Dielectric damping can not be distinguished from damping due to losses caused in a material with a conductivity $\sigma \neq 0$. In a conducting material, applying an electric field will cause a current density $\vec{J} = \sigma\vec{E}$. Substituting into (2.7) gives

$$\begin{aligned}
\nabla \times \vec{H} &= j\omega\vec{D} + \vec{J} && (2.13)\\
&= j\omega\varepsilon\vec{E} + \sigma\vec{E} && (2.14)\\
&= j\omega\varepsilon'\vec{E} + (\omega\varepsilon'' + \sigma)\vec{E} && (2.15)
\end{aligned}$$

The ratio between the real and the imaginary part of the total replacement current defines the so called loss tangent which is a frequency dependent value

$$\tan(\delta) = \frac{\omega\varepsilon'' + \sigma}{\omega\varepsilon'}. \tag{2.16}$$

The loss tangent and the real permittivity $\varepsilon' = \varepsilon_r\varepsilon_0$ are often used to characterize materials in microwave engineering.

The relation between the magnetic flux $\vec{B}$, the magnetic field amplitude $\vec{H}$ and the magnetic polarization $\vec{P_m}$ is

$$\vec{P_m} = \chi_m\vec{H}, \tag{2.17}$$

where χ_m is called the magnetic susceptibility. This leads to a magnetic flux density

$$\vec{B} = \mu_0(\vec{H} + \vec{P_m}) = \mu_0(1 + \chi_m)\vec{H} = \mu\vec{H}, \tag{2.18}$$

where

$$\mu = \mu' - j\mu'' = \mu_0(1 + \chi_m) \tag{2.19}$$

is the complex permeability of the medium. The imaginary part of μ is again responsible for damping of electromagnetic waves in the material. In contrast to damping due to the finite conductivity in a conductor, there is no magnetic conductivity, since there is no real magnetic current.

2.2.2 Plane Waves in a General Lossy Medium

In this section, the basics of plane wave propagation in a general lossy medium is repeated as the definitions will be used in the following.

In a source-free, linear, isotropic, homogeneous, lossy and conductive material, Maxwell's curl equations in phasor form can be written from (2.6),(2.7) and (2.13) as

$$\begin{aligned} \nabla \times \vec{E} &= -j\omega\mu\vec{H}, && (2.20) \\ \nabla \times \vec{H} &= j\omega\varepsilon\vec{E} + \sigma\vec{E}. && (2.21) \end{aligned}$$

Taking the curl of (2.20) and using (2.21) results in

$$\nabla \times \nabla \times \vec{E} = (\omega^2\mu\varepsilon - j\omega\mu\sigma)\vec{E}. \tag{2.22}$$

Using the vector identity $\nabla \times \nabla \times \vec{A} = \nabla(\nabla \cdot \vec{A}) - \nabla^2\vec{A}$ gives the Helmholtz wave equation for $\vec{E}$

$$\nabla^2\vec{E} + \omega^2\mu\varepsilon\left(1 - j\frac{\sigma}{\omega\varepsilon}\vec{E}\right) = 0, \tag{2.23}$$

since $\nabla \cdot \vec{E} = 0$ in a source-free region. In an analogous way the wave equation for $\vec{H}$ may be derived

$$\nabla^2\vec{H} + \omega^2\mu\varepsilon\vec{H} = 0. \tag{2.24}$$

The complex propagation constant for the medium then is

$$\gamma = \alpha + j\beta = j\omega\sqrt{\mu\varepsilon\left(1 - j\frac{\sigma}{\omega\varepsilon}\right)}. \tag{2.25}$$

α is attenuation constant of the wave. β is the wave number or propagation constant. The wavelength is $\lambda = 2\pi/\beta$. The phase velocity is defined as $v_p = \omega/\beta$.

Finally, one can define the intrinsic wave impedance η as the ratio of the $\vec{E}$ and $\vec{H}$ fields. For plane waves, this impedance is also the intrinsic impedance of the medium. In free-space, $\eta = \sqrt{\mu_0/\varepsilon_0} = 377\ \Omega \equiv \eta_0$. In a general lossy media the wave impedance is related to the propagation constant

$$\eta = \frac{j\omega\mu}{\gamma}. \tag{2.26}$$

$\vec{E}$ and $\vec{H}$ are orthogonal to each other and orthogonal to the direction of propagation denoted by $+\hat{z}$ or $+\hat{z}$ depending on the direction of propagation along the z-axis.

The complex propagation constant of a good conductor with $\sigma \gg \omega\varepsilon$ or equivalently $\varepsilon'' \gg \varepsilon'$ can be approximated as

$$\gamma = \alpha + j\beta \simeq j\omega\sqrt{\mu\varepsilon(\frac{\sigma}{j\omega\varepsilon})} = (1 + j).\sqrt{\frac{\omega\mu\sigma}{2}} \tag{2.27}$$

A plane wave can penetrate the material only by a characteristic length, the so called skin depth, which is

$$\delta_s = \frac{1}{\alpha} = \sqrt{\frac{2}{\omega\sigma\mu}}. \tag{2.28}$$

The amplitude of the wave decays by an amount 1/e after travelling a distance of δ_s into the material.
For a frequency $f = \frac{\omega}{2\pi} = 10$ GHz and a conductivity of $\sigma \simeq 10^7$ S/m for a good metallic non-magnetic ($\mu = \mu_0$) conductor at room temperature one calculates $\delta_s \simeq 1.6 \cdot 10^{-6}$ m $= 1.6\mu$m. This shows, that only the surface of conductors is important for the losses. Moreover a single metallic conductor could never support propagating microwaves as they would be damped exponentially, in contrast to a low frequency current. Therefore, microwave guides for electromagnetic wave propagation always consist of at least two metallic conductors. The field of the propagating waves 'lives' in between these conductors.
By introducing the intrinsic wave impedance inside a good conductor as

$$\eta = \frac{j\omega\mu}{\gamma} \simeq (1+j)\sqrt{\frac{\omega\mu}{2\sigma}} = (1+j)\frac{1}{\sigma\delta_s}, \tag{2.29}$$

one can calculate the power dissipation in the surface layer of a good conductor.
Figure 2.1 shows an infinitely thick slab consisting of a good conductor. There is an electromagnetic wave perpendicularly hitting the surface of the slab, inducing a surface current in x-direction. As the frequency ω is chosen so that $\omega\tau_{em} \gg 1$, nearly all the current in the material is confined to within a skin depth δ_s close to the surface. Therefore, the current density is modelled to be uniform within a depth δ_s from the surface as shown in Figure 2.1. Moreover, there is approximately no current in the slab for distances exceeding δ_s. With the dimensions given in Figure 2.1, one can calculate the equivalent resistance, the current $I = |\vec{j}\delta_s\Delta z|$ has to pass, when flowing in x-direction through an area $A = \delta_s\Delta z$ assuming a conductivity σ:

$$R = \frac{\Delta x}{\sigma\delta_s\Delta z}. \tag{2.30}$$

The power dissipated within this resistor per unit area is

$$P_{diss} = \frac{I^2R}{\Delta x\Delta z} = \frac{I^2}{\sigma\delta_s(\Delta z)^2} = I_S^2R_S, \tag{2.31}$$

which can be interpreted as a surface current $I_S = \frac{I}{\Delta z}$ passing through the so called surface resistance

$$R_S \equiv \frac{1}{\delta_s\sigma} = \sqrt{\frac{\pi f\mu}{\sigma}} = \sqrt{\frac{\omega\mu}{2\sigma}} = \Re(\eta). \tag{2.32}$$

This surface resistance is responsible for the power dissipation P_{diss} within the surface because of the finite conductivity σ. This model gives exactly the same result as a more realistic calculation assuming a current that is exponentially decaying with increasing distance from the surface. This means that the skin-effect resistance of the semi-infinite plane conductor is the same as the DC resistance of a layer of thickness δ_s with a uniform current density j. The dimension of R_S is $[\Omega/\text{m}^2]$.

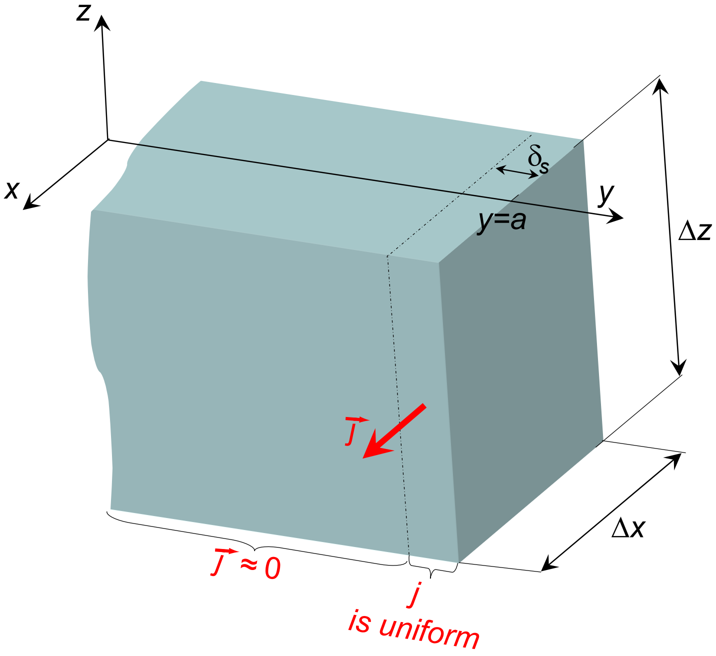

Figure 2.1: An approximative model of the current distribution in an ohmic slab to qualitatively deduce the surface resistance.

The surface resistance is equal to the real part of the surface impedance

$$Z_S \equiv \eta = \left.\frac{\vec{E}_x}{\vec{H}_z}\right|_{y=a} \simeq (1+j)\frac{1}{\delta_s \sigma} = (1+j)\sqrt{\frac{\omega\mu}{2\sigma}} = \sqrt{j\frac{\omega\mu}{\sigma}}. \tag{2.33}$$

In analogy, one can associate the imaginary part of the surface impedance with a surface reactance $\omega L_S = \frac{1}{\delta_s \sigma}$ (where L_S is called surface inductance), which yields to

$$Z_S = R_S + j\omega L_S. \tag{2.34}$$

The local approach given here is very simple, but nevertheless, also valid for more complex fields and conductors of arbitrary shape, as long as bends or corners have radii of the order of a skin depth or larger. The method is also quite accurate, as the only approximation is that $\eta \ll \eta_0 = 377\ \Omega$ [4], which is a good approximation. As an example, copper at 1 GHz has $|\eta| = 0.012\ \Omega$.

Finally, the time-average of the electric and magnetic energy stored in a Volume V in the case of a harmonic time dependence $e^{j\omega t}$ is given by

$$W_e = \frac{1}{2} \cdot \frac{1}{2} \Re \left(\int_V \vec{E} \cdot \vec{D}^* dv \right) \tag{2.35}$$

$$W_m = \frac{1}{2} \cdot \frac{1}{2} \Re \left(\int_V \vec{H} \cdot \vec{B}^* dv \right) \tag{2.36}$$

The extra $\frac{1}{2}$-term in both equations is due to time averaging. If calculations are done in a quasi static limit, this factor drops out.
These relations will be used to link the general field theory to the basic circuit theory in order to derive the transmission line theory in section 2.2.6 for an arbitrary wave guide.

2.2.3 Quasi static Approximation and Characteristic Timescales

If the characteristic length scale l of a structure is much smaller than the characteristic wavelength of an electromagnetic field interacting with it, the coupling between the associated electric and magnetic field is weak and a quasi static approximation is appropriate. This quasi static criterion based on spatial dimensions can be quantified [5]:

$$l \ll \lambda = \frac{2\pi c}{\omega} \tag{2.37}$$

where λ is the wavelength, ω is the angular frequency and $c = \frac{1}{\sqrt{\mu\varepsilon}}$ the velocity of the propagating wave on the structure.
Apart from this, a time-based quasi static criterion may be given, linking the angular frequency ω to a characteristic time, the so called *electromagnetic coupling time* τ_{em} which is defined as

$$\tau_{em} \equiv \frac{l}{c} = l\sqrt{\mu\varepsilon} \tag{2.38}$$

If

$$\omega\tau_{em} \ll 1, \tag{2.39}$$

it is possible to solve the dominant field quantities without using the wave equation as there is no wave propagation. If the dominant field is an electric field, most of the electromagnetic energy in the system is stored in capacitive elements. The system is then called an electro quasi static (EQS) system. If the dominant field is a magnetic one, meaning most of the electromagnetic energy in the system is stored by inductive components, one has to deal with a magneto quasi static (MQS) system. Whether the system can be described by an EQS or a MQS model, is highly dependent on the structure itself, whose geometry, conductivity, permeability and permittivity are essential.

Using conservation of charge, Ohm's law and Gauss's law together with the assumption of non dispersive material properties, one can deduce the following equation for the time evolution of the electric field in an EQS problem [5]:

$$\left(1 + \frac{\varepsilon}{\sigma_0}\frac{\partial}{\partial t}\right) \nabla\vec{E} = 0. \tag{2.40}$$

The coefficient of the time derivative is the time associated with the natural electrodynamics of the system. The time constant for an EQS system

$$\tau_e \equiv \frac{\varepsilon}{\sigma_0} \tag{2.41}$$

is called charge relaxation time and is analogous to the capacitive time constant τ_{RC} for a lumped parallel R-C circuit $\tau_{RC} = RC$.

For a MQS system, one can find another time constant in a more complicated calculation [5]. The so called magnetic diffusion time τ_m is defined by

$$\tau_m \equiv \mu\sigma_0 l^2. \tag{2.42}$$

This time constant is equivalent to the inductive time constant τ_{RL} for a lumped serial R-L circuit $\tau_{RL} = L/R$. If one speaks in terms of characteristic length scales instead of times and frequencies, one has to point out, that a comparison of ω with $1/\tau_m$ is equivalent to comparing the skin depth $\delta_s(\omega)$ as defined in 2.28 with the characteristic length scale l of the system, since

$$\omega\tau_m = \omega\mu\sigma_0 l^2 = 2l^2/\delta_s(\omega)^2. \tag{2.43}$$

From $\omega\tau_m \ll 1$ it follows that $l \ll \delta_s(\omega)$, this means that electromagnetic waves can penetrate deeply into the ohmic material, the dissipation is high. In a lumped serial R-L circuit, this situation corresponds to the case of low frequency, where most of the voltage falls across the dissipative resistance R. From $\omega\tau_m \gg 1$ it follows that $l \gg \delta_s(\omega)$. Here, the electromagnetic wave is stopped at the surface of the structure. Most of the voltage drops across the non dissipative inductance.
It is obvious that

$$\tau_{em} = \sqrt{\tau_e \tau_m}. \tag{2.44}$$

Thus τ_{em} is equivalent to $\tau_{LC} \equiv \sqrt{LC} = \sqrt{\tau_{RL}\tau_{RC}}$, the inverse of the resonance frequency of an L-C network. Equation (2.44) also shows that in the quasi static approximation, a system can only be either EQS or MQS.
In Figure 2.2, a summary of all relevant quasi static regimes as well as lumped element representations of the corresponding systems are given.
Taking into account the different time scales is also very helpful for the determination of the propagation parameters and the characteristic impedance of a CWG. It is convenient to split the CWG problem in a problem in z direction and x-y direction as shown in Figures 2.20 and 2.21. This is due to two important aspects: first, the translation symmetry in

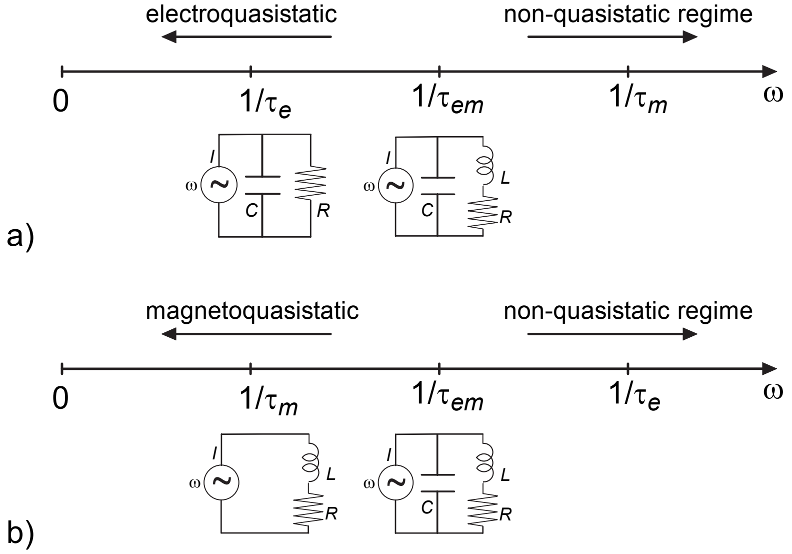

Figure 2.2: Possible orderings of the characteristic frequencies of the different quasi static regimes and lumped element representations of the corresponding quasi static systems; (a) the electro quasi static case and (b) the magneto quasi static case.

z direction and second the fact that in x-y direction a quasi static approach is valid up to very high frequencies, as the dimensions of a CWG perpendicular to the propagation direction z are much smaller than the propagation wave length λ. The CWGs presented in this thesis have typical dimensions of $100\,\mu$m in x-y direction, corresponding to a frequency $f = \frac{c}{\lambda} = \frac{3\cdot 10^{-7}\,\mathrm{m/s}}{100\mu\mathrm{m}} = 300$ GHz, where c was supposed to be only $\frac{1}{10}$ of the speed of light in vacuum. Even in the worst case, the quasi static approximation would be valid for frequencies up to several ten GHz.

It is also clear, that the system in the x-y plane is in the EQS regime, as the fields of interest between the inner strip and the ground electrodes are propagating in a nearly perfectly isolating material (air and substrate) and hence $1/\tau_e \to 0$. This means that most *energy* (*second* order in the corresponding field term) in the system is stored in electrical fields (nevertheless, magnetic fields are not negligible, otherwise the Poynting vector[1] would be zero and no power could be transferred by the transmission line) .

For the description of the system in z direction, a quasi static model is not valid. However, in this case transmission line theory can be applied as λ is of the order of the transmission line length (see section 2.2.6). Nevertheless, also in this direction, one can be confronted with important time scales which are connected to both, the material and the geometry of the structure. Both aspects and their interplay will be elucidated in the following subsection.

---

[1] also *first* order in electrical and magnetic field

2.2.4 Normal Conductor, Perfect Conductor and Superconductor

From an engineers point of view, superconductivity has two important macroscopic features, which have to be considered when designing superconducting circuits:

1. the perfect DC conductivity, and

2. the Meissner effect.

In this section, only the first aspect will be considered. Classically it can be described by the first London equation [6] . If one also wants to take into account the Meissner effect as the flux expelling property of a superconductor in an applied external magnetic field, one has to introduce the second London equation. Perfect conductors instead are not flux expelling, but rather flux conserving media.
To better understand perfect DC conductivity, one usually starts from normal conductivity that allows to introduce two further time scales. These will help to understand the mechanism of a superconducting transmission line in the microwave regime.
It is possible to extract Ohm's law of conduction from the Drude model [7, 8]:

$$\vec{J}(\omega) = \sigma(\omega)\vec{E} = \sigma_0 \frac{1}{1 + j\omega\tau_{tr}} \vec{E}(\omega), \tag{2.45}$$

where

$$\sigma_0 \equiv \frac{nq^2\tau_{tr}}{m} \tag{2.46}$$

is the DC conductivity. ω is the frequency with which a source drives the system, n is the number density of carriers in the material, q is the charge of the carriers, m the mass of the carriers and τ_{tr} is a characteristic time of the material, the so called scattering time. It is the mean time of free motion of a carrier between two collisions of the carrier with a scatterer.

Neglecting parasitic capacitances, a piece of conductor may be modelled as a serial connection of a resistor R and an inductance L as shown in Figure 2.2 (b) for the MQS regime. As known from basic lumped circuit analysis, the complex resistance $\bar{Z} = \bar{U}/\bar{I} = R + jX$ of such a circuit is the sum of the complex resistances of the resistor $\bar{Z}_R = R$ and the inductance $\bar{Z}_L = j\omega L$:

$$\bar{Z} = \bar{Z}_R + \bar{Z}_L = R + j\omega L \;\Rightarrow\; \bar{Y} = 1/\bar{Z} = \frac{1}{R}\left(\frac{1}{1 + j\omega\frac{L}{R}}\right) = \frac{1}{R}\left(\frac{1}{1 + j\omega\tau_{RL}}\right) \tag{2.47}$$

$\bar{Y} = \bar{I}/\bar{U}$ is the complex admittance and can be interpreted as a transfer function between the input $\bar{U}$ and the output $\bar{I}$. By comparing (2.47) with (2.45), one can make the following useful analogies:

$$\begin{aligned} R &\Leftrightarrow \frac{1}{\sigma_0} = \frac{m}{nq^2\tau_{tr}}, & (2.48)\\ \tau_{RL} &\Leftrightarrow \tau_{tr}, & (2.49)\\ L &\Leftrightarrow \frac{\tau_{tr}}{\sigma_0} = \frac{m}{nq^2}. & (2.50) \end{aligned}$$

For $\omega = 0$ it is now possible to model perfect DC conductivity by setting $\sigma_0 \to \infty$. For $\omega \neq 0$ however, one has to pay attention when assuming $\sigma_0 \to \infty$, as also the denominator in (2.45) tends to ∞ as $\tau_{tr} \propto \sigma_0$. This means that it is not sufficient to simply set $\sigma_0 = \infty$ and neglect the frequency dependent part of $\sigma(\omega)$.
To overcome the problem of modelling perfect conductivity by carefully taking the limit $\sigma_0 \to \infty$ or $\tau_{tr} \to \infty$ in (2.45), Heinz and Fritz London *postulated* in 1935 a constitutive law equivalent to Ohm's law but - by construction - already valid for the limit $\tau_{tr} \to \infty$. It was postulated to be valid for a new kind of carriers with unknown mass m^*, charge q^* and number density n^*. The law is called first London equation [2]

$$\vec{E} = \frac{\partial}{\partial t}(\Lambda_L \vec{I}), \qquad (2.51)$$

where Λ_L is a material constant

$$\Lambda_L \equiv \frac{m^*}{n^*(q^*)^2}. \qquad (2.52)$$

Today we know that the postulated new carriers are Cooper pairs with $m^* = 2m_e$ and $q^* = 2e$.
The first London equation shows, that even a perfect conductor will develop a voltage drop across it when driven by an AC current [5]. This voltage is due to the inertia of the Cooper pairs. Because of this inertia, the Cooper pairs cannot follow the external driving; the phase difference between the driving source and the motion of the carriers gives rise to a voltage across the perfect conductor. It is important to stress, that no energy is dissipated by this process. This is analogous to the AC voltage drop across an inductance which is a non dissipative element. Comparing (2.52) with (2.50) shows that the inertia of the Cooper pairs can indeed be modelled by an inductance L with the analogy

$$L \Leftrightarrow \Lambda. \qquad (2.53)$$

This is equivalent to setting $R = 0$ in Figure 2.2 (b) for the MQS regime. Thus, in the case of the perfect conductor, the characteristic frequency $1/\tau_{tr} = 0$ is useless as ω will always

---

[2] Here, the kinetic energy of the carriers is neglected. This is equivalent to $|\vec{E}| \gg |\vec{v}_s||\vec{B}|$, which - in turn - is equivalent to the assumption that the magnetic contribution to Lorentz's law can be neglected compared to the electric one

be longer than zero. If one speaks again about characteristic length scales instead of times and frequencies as done for the skin depth $\delta_s(\omega)$ in (2.43), it seems reasonable, that for a perfect conductor, the characteristic length scale is *not* dependent on the frequency ω. The characteristic length scale of a perfect conductor is called London penetration depth and is defined as

$$\lambda_L \equiv \sqrt{\frac{\Lambda}{\mu_0}} \tag{2.54}$$

which is indeed independent of frequency in contrast to the skin depth $\delta_s(\omega)$. Applied fields can penetrate the perfect conductor over a distance λ_L. Although the perfect conductor allows the applied field to penetrate, the energy associated with these fields is reactive. Thus, the perfect conductor stores energy associated with the magnetic field but releases this energy completely when the applied field is removed. There can never be any power transfer into the material and the perfect conductor will appear lossless for all frequencies. In other words, the magnetic field in the ohmic case penetrates as a damped wave while the field in the perfectly conducting case is evanescent.

Together with (2.54), (2.51) can be written in phasor form in analogy to Ohm's law

$$\vec{I} = \frac{1}{j\omega\mu_0\lambda_L^2}\vec{E}. \tag{2.55}$$

2.2.5 Two-Fluid Model for Superconductors

The two-fluid model describes the electromagnetic behaviour of a superconductor up to very high frequencies. It treats a superconductor as a mixture of a normal and a perfect conductor. In fact, for $T \leq T_c$, there is a coexistence of Cooper pairs maintaining the supercurrent $\vec{I_s}$ and unpaired electrons maintaining the normal (ohmic) current $\vec{I_n}$. Both contribute to the conductivity. Hence, a lumped element representation of a superconductor within the two-fluid model is a parallel circuit consisting of a superconducting channel and a normal channel as shown in Figure 2.3. The total current through a superconductor then writes (2.45),(2.55)

$$\vec{I} = \vec{I_n} + \vec{I_s} = \left(\frac{\widetilde{\sigma}_0(T)}{1 + j\omega\tau_{tr}} + \frac{1}{j\omega\mu_0(\lambda_L(T))^2}\right)\vec{E}. \tag{2.56}$$

In this equation, the temperature dependence of $\lambda_L(T)$ and $\widetilde{\sigma}_0(T)$ is depicted expressly since the number density of Cooper pairs $n^*(T)$ and the density of normal conducting electrons

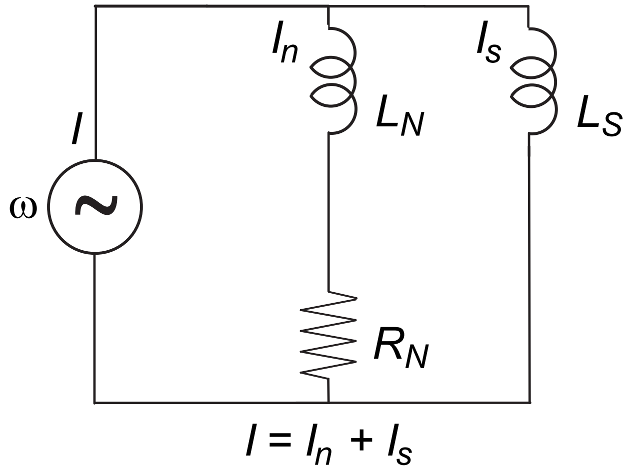

Figure 2.3: Lumped element representation of a superconductor in the two-fluid model. I_n is the current through the normal (ohmic) channel, I_s the current through the superconducting channel.

$n(T)$ are temperature dependent corresponding to the *empirical two-fluid approximation* [9]

$$n(T) = n_{tot}\left(\frac{T}{T_c}\right)^4 \qquad \text{for } T \leq T_c \tag{2.57}$$

$$n^*(T) = \frac{1}{2}n_{tot}\left(1 - \left(\frac{T}{T_c}\right)^4\right) \qquad \text{for } T \leq T_c \tag{2.58}$$

where $n_{tot} = n(T) + 2n^*(T)$ for all T is the temperature independent density of electrons contributing to conduction in the normal state of the material. The temperature dependence is shown in Figure 2.4. The expressions for $\lambda_L(T)$ and $\widetilde{\sigma}_0(T)$ are obtained by substituting (2.57) in (2.46) and (2.58) in (2.52), (2.54):

$$\lambda_L(T) = \sqrt{\frac{\Lambda_L(T)}{\mu_0}} = \frac{1}{\sqrt{\mu_0}}\left(\frac{m}{n_{tot}e^2}\left(\frac{1}{1-(T/T_c)^4}\right)\right)^{\frac{1}{2}} \qquad \text{for } T \leq T_c \tag{2.59}$$

$$\widetilde{\sigma}_0(T) = \frac{n_{tot}e^2\tau_{tr}}{m}\left(\frac{T}{T_c}\right)^4 \qquad \text{for } T \leq T_c \tag{2.60}$$

By comparing the lumped element circuit in Figure 2.3 which represents the two-fluid model to the lumped circuits in Figure 2.2, one can see that there are two important time constants in the two-fluid model. They are found by exploiting the analogies

$$\frac{L_n}{R_n} \Leftrightarrow \tau_{tr} \tag{2.61}$$

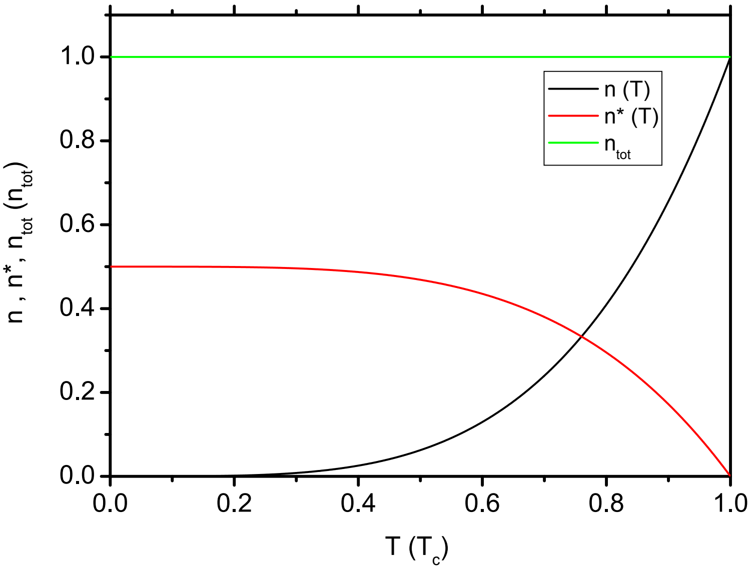

Figure 2.4: The temperature dependence of $n(T)$, $n^*(T)$ and n_{tot}.

λ_0	$\widetilde{\sigma}_0(T_c)$	$n_{tot} = 2\frac{2m_e}{4\lambda_0^2 e^2 \mu_0}$	$1/\tau_{tr} = \frac{n_{tot}e^2}{\widetilde{\sigma}_0(T_c)m_e}$	$1/\tau_{chan}$ (T = 4.2 K)
39 ± 5 nm [11]	$1.4 \cdot 10^9$ ($\Omega^{-1}\mathrm{m}^{-1}$) [10]	$1.9 \cdot 10^{28}$ m^{-3}	370 GHz	8.4 THz

Table 2.1: Calculated values for $1/\tau_{tr}$ and $1/\tau_{chan}$ for niobium.

and

$$\frac{L_s}{R_n} \Leftrightarrow \widetilde{\sigma}_0(T)\Lambda_L(T) \equiv \tau_{chan}, \tag{2.62}$$

where a new characteristic time constant τ_{chan} has been introduced (*chan* means *channel*). From (2.62) one can deduce

$$\tau_{chan} = \tau_{tr}\left(\frac{(T/T_c)^4}{1-(T/T_c)^4}\right) \qquad \text{for } T \leq T_c. \tag{2.63}$$

Within this work, the structures will be fabricated in niobium, therefore τ_{tr} and τ_{chan} are estimated for niobium in table 2.1 [3].

Table 2.1 shows that both characteristic frequencies (τ_{tr} and $1/\tau_{chan}$) are much higher than the operation frequency of the hybrid, which will approximately be between 3 and 10 GHz. Firstly, this means that in the normal channel, the inductance due to the inertia of the normal electrons is negligible compared to the resistance ($\omega \ll 1/\tau_{tr}$). Secondly, for an operation temperature of 4.2 K, most of the current will be a suppercurrent ($\omega \ll 1/\tau_{chan}$). This means

---

[3] $\widetilde{\sigma}_0(T_c)$ was calculated by $\widetilde{\sigma}_0(T_c) = \frac{\omega\mu}{2R_s(T_c)^2}$, using the measured surface resistance $R_s(T_c = 9.2\text{ K})$ at $2\pi\omega = 27.45$ GHz [10].

that ohmic losses due to the normal channel will play a minor role. Only very close to the critical temperature, one should expect a considerable contribution of the normal current for frequencies above 6 GHz. In this case, the complex conductivity in (2.56) reduces to

$$\vec{I} = \vec{I}_n + \vec{I}_s = \left(\widetilde{\sigma}_0(T) - j\frac{1}{\omega\mu_0(\lambda_L(T))^2}\right)\vec{E} \equiv (\sigma_1 - j\sigma_2)\vec{E} \equiv \sigma_{eff}\vec{E}. \tag{2.64}$$

Now, also the formula for the surface impedance for a good conductor (2.33) may be adopted, too. Using the complex conductivity (2.64), as well as (2.57), (2.58), (2.60), (2.59), (2.32) and a binomial expansion, equation (2.33) becomes

$$\begin{aligned} Z_S &\simeq j\omega\mu_0\lambda_L\left(1 - j\frac{\omega\tau n}{2n^*}\right) = \frac{\omega^2\mu_0^2\lambda_L^3 n\widetilde{\sigma}_0}{2n_{tot}} + j\omega\mu_0\lambda_L = \frac{2}{\delta_s\widetilde{\sigma}_0}\left(\frac{\lambda_L}{\delta_s}\right)^3 + j\omega\mu_0\lambda_L \\ &= 2R_S\left(\frac{\lambda_L}{\delta_s}\right)^3 + j\omega\mu_0\lambda_L \equiv R_{S,sc} + j\omega L_{S,sc}, \end{aligned} \tag{2.65}$$

where explicit temperature dependences have been suppressed. R_S is the surface resistance of the normal conducting electrons as defined in (2.32). The superconducting surface resistance $R_{S,sc}$ is reduced (λ_L/δ_s) to the power of three compared to the ohmic case. This is the reason for the reduced power dissipation in superconductors if $\lambda_L \ll \delta_s$.

A comparison of the London penetration depth $\lambda_L(T)$ of (2.59) to the skin depth $\delta_s(T)$ for 3, 100 and 1000 GHz (2.28), (2.60) for niobium is displayed in Figure 2.5. Numerical values for this figure have been taken from table 2.1. Only for frequencies higher than 1000 GHz, λ_L gets comparable to δ_s at 4.2 K. At 3 GHz and 4.2 K, $R_{S,sc}$ is reduced by a factor of approximately $8 \cdot 10^{-6}$ compared to the ohmic case.

Finally, another characteristic frequency ω_{pair} is given by the temperature dependent energy gap $2\Delta(T)$ separating the Cooper pairs from the spectrum of the quasi particles. Irradiation with photons with more than the gap energy will break up Cooper pairs and thus destroy superconductivity. Assuming $2\Delta(0) \approx 3$ meV in niobium [10], the minimum frequency for the photons to split the Cooper pairs is $f_{min} = 2\pi\omega_{pair} = \frac{2\Delta(0)}{h} \approx 725$ GHz. This is far away from the operation frequency.

2.2.6 Transmission Line Theory

2.2.6.1 Lumped Element Representation

A transmission line is often represented as a two-wire line, since transmission lines for TEM wave propagation always require at least two conductors. A piece of line of infinitesimal length Δz shown in Figure 2.6 can be modelled as a lumped element circuit, as shown in Figure 2.7. A lumped element representation and thus the application of the basic circuit theory is valid since one can neglect any phase change of the propagating wave within the infinitesimal length Δz.

The variables in Figure 2.7 represent the following physical magnitudes:

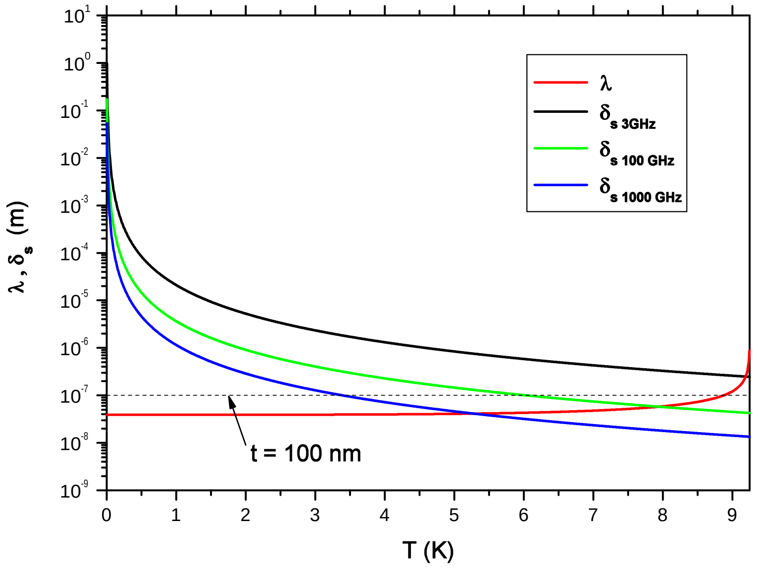

Figure 2.5: Comparison of the penetration depth $\lambda_L(T)$ of niobium with its skin depth $\delta_s(T)$ for 3, 100 and 1000 GHz.

Figure 2.6: Voltage and current definitions for an infinitesimal length of transmission line.

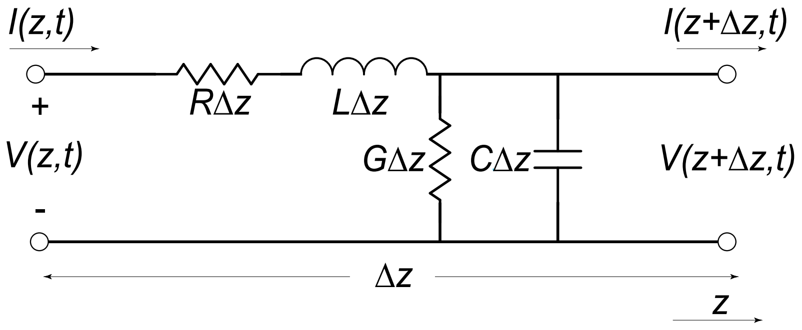

Figure 2.7: A lumped element representation of an infinitesimal length of a transmission line.

R is the series resistance per unit length for both conductors in [Ω/m].
L is the series inductance per unit length for both conductors in [H/m].
G is the shunt conductance per unit length in [S/m].
C is the shunt capacitance per unit length in [F/m].
R and G are responsible for losses in the transmission line. R is due to finite conductivity of the conductors, whereas G is due to dielectric losses in the material between the conductors.

Applying Kirchhoff's laws to the lumped element circuit leads to

$$V(z,t) - R\Delta z I(z,t) - L\Delta z \frac{\partial I(z,t)}{\partial t} - V(z+\Delta z,t) = 0, \tag{2.66}$$

$$I(z,t) - G\Delta z V(z+\Delta z,t) - C\Delta z \frac{\partial V(z+\Delta z,t)}{\partial t} - I(z+\Delta z,t) = 0. \tag{2.67}$$

V and I are voltage and current at the positions of the lumped element representation of the transmission line as shown in Figure 2.7.
Dividing (2.66) and (2.67) by Δz, taking the limit $\Delta z \longrightarrow 0$ and assuming a $e^{j\omega t}$ time dependence (thus basically replacing the time derivatives by $j\omega$) leads to

$$\frac{dV(z)}{dz} = -(R + j\omega L)I(z), \tag{2.68}$$

$$\frac{dI(z)}{dz} = -(G + j\omega C)V(z). \tag{2.69}$$

This set of differential equations can be decoupled simultaneously ending up with wave equations for $I(z)$ and $V(z)$

$$\frac{d^2V(z)}{dz^2} - \gamma^2 V(z) = 0, \tag{2.70}$$

$$\frac{d^2I(z)}{dz^2} - \gamma^2 I(z) = 0. \tag{2.71}$$

with the complex propagation constant

$$\gamma = \alpha + j\beta = \sqrt{(R + j\omega L)(G + j\omega C)}. \tag{2.72}$$

The wave equations can be solved by the ansatz

$$V(z) = V_0^+ e^{-\gamma z} + V_0^- e^{\gamma z}, \tag{2.73}$$

$$I(z) = I_0^+ e^{-\gamma z} + I_0^- e^{\gamma z}. \tag{2.74}$$

The first terms represent waves propagating in the $+z$ direction, whereas the second summands represent waves propagating in the $-z$ direction.
Applying (2.68) to (2.73) gives the current in the line $I(z) = \frac{\gamma}{R+j\omega L} V_0^+ e^{-\gamma z} - V_0^- e^{\gamma z}$. Com-

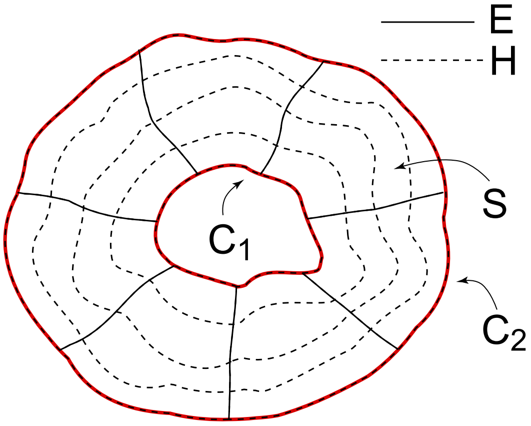

Figure 2.8: Cross section of an arbitrary uniform TEM transmission line.

paring this to (2.74) one can relate the voltage and current amplitudes of the left- and right-travelling waves and define the characteristic impedance Z_0 by

$$Z_0 = \frac{V_0^+}{I_0^+} = \frac{-V_0^-}{I_0^-} = \frac{R + j\omega L}{\gamma} = \sqrt{\frac{R + j\omega L}{G + j\omega C}}. \tag{2.75}$$

The current can then be written in the form

$$I(z) = \frac{V_0^+}{Z_0} e^{-\gamma z} - \frac{V_0^-}{Z_0} e^{\gamma z}. \tag{2.76}$$

Once being able to link field theory to the present transmission line theory, one can calculate R, L, G and C for an arbitrary transmission line. This can be done by comparing the time-averaged magnetic and electric energy stored in a section of a uniform transmission line as shown in Figure 2.8, where S is the area of the line. C_1 and C_2 are the contours of the area S.

Elementary circuit theory gives for the time-averaged magnetic energy

$$W_m = \frac{1}{2} \cdot \frac{1}{2} L \mid I_0 \mid^2 . \tag{2.77}$$

This is equal to the field theoretical result given by (2.36). Together with the material equations (2.11) and (2.18), the self-inductance per unit length is

$$L = \frac{\mu}{\mid I_0 \mid^2} \int_S \vec{H} \cdot \vec{H}^* ds. \tag{2.78}$$

Since superconducting transmission lines are almost always driven below the superelectron plasma frequency (see e.g. reference [5]), electric fields within a superconductor are negligible and one only has to take care about *inductive* contributions from inside the superconducting material to the propagation parameters of a superconducting transmission line. In addition, there will also be the contribution from the electric and magnetic fields outside the conducting material.
It is often convenient to distinguish the inductances related to the internal and external flux and call them external inductance L_{ext} and internal inductance L_int, respectively [12]. Such a separation is also used in the derivation in section 2.4.2.
The capacitance per unit length can be calculated in an analogous way by

$$C = \frac{\varepsilon}{\mid V_0 \mid^2} \int_S \vec{E} \cdot \vec{E}^* ds. \tag{2.79}$$

In a field theoretical calculation of R, one has to consider the conductor power loss P_c per unit length due to the surface current $\vec{I_s}$ that is induced when a wave penetrates the conductor with finite conductivity σ over the skin depth δ_s inducing a surface current $\vec{I_s}$ (see section):

$$P_c = \frac{R_s}{2} \int_{C_1+C_2} \vec{I_s} \cdot \vec{I_s^*} dl = \frac{R_s}{2} \int_{C_1+C_2} \vec{H_t} \cdot \vec{H_t^*} dl. \tag{2.80}$$

C_1 and C_2 are the contours shown in Figure 2.8, R_s is the surface resistance defined by $R_s = \frac{1}{\sigma\delta_s} = \sqrt{\frac{\omega\mu}{2\sigma}}$ and $\vec{H_t}$ the tangential magnetic field component. $\vec{I_s}$ and $\vec{H}$ are related by $\vec{I_s} = \hat{n} \times \vec{H}$, where $\hat{n}$ is the unit vector perpendicular on the surface S shown in Figure 2.8.

Circuit theory models power dissipation due to ohmic losses by $P_c = R \mid I_0 \mid^2 /2$. Therefore, the series resistance per unit length

$$R = \frac{R_s}{\mid I_0 \mid^2} \int_{C_1+C_2} \vec{H} \cdot \vec{H}^* dl \tag{2.81}$$

can be calculated.
The time-averaged power dissipation per unit length in a lossy dielectric is

$$P_d = \frac{\omega\varepsilon''}{2} \int_S \vec{E} \cdot \vec{E}^* ds. \tag{2.82}$$

Circuit theory provides for the power dissipation due to losses in the dielectric $P_d = G \mid$

$V_0 |^2 /2$. Therefore, the shunt capacitance per unit length is

$$G = \frac{\omega\varepsilon''}{| V_0 |^2} \int_S \vec{E} \cdot \vec{E}^* ds. \tag{2.83}$$

2.2.6.2 Low Loss Transmission Line

A low loss transmission line is characterized by $R \ll \omega L$ and $G \ll \omega C$. In this case, the complex propagation constant γ may be expanded in a Taylor series to give the first higher order term for γ

$$\gamma \simeq j\omega \sqrt{LC} \left[1 - \frac{j}{2} \left(\frac{R}{\omega L} + \frac{G}{\omega C} \right) \right] = \alpha + j\beta \tag{2.84}$$

with

$$\alpha \simeq \left(R \sqrt{\frac{C}{L}} + G \sqrt{\frac{L}{C}} \right), \beta \simeq \omega \sqrt{LC}. \tag{2.85}$$

It is important to note, that low losses can be introduced by just adding a real part to the propagation constant γ, or equivalently by the substitution $\beta \to \beta - i\alpha$.
In the low loss case, the phase velocity defined as

$$v_{ph} \equiv \frac{\omega}{\beta} \tag{2.86}$$

is

$$v_{ph} = \frac{1}{\sqrt{LC}}. \tag{2.87}$$

Up to the same order of approximation, Z_0 can be expressed by the value of the lossless case

$$Z_0 = \sqrt{\frac{R + j\omega L}{G + j\omega C}} \simeq \sqrt{\frac{L}{C}}. \tag{2.88}$$

2.2.6.3 Terminated Transmission Line

To build networks from sections of transmission lines and arbitrary impedance loads, it is essential to understand the behaviour of a transmission line terminated by a load impedance Z_L as shown in Figure 2.9.
The total voltage and current at the load ($z = 0$) are related by the load impedance (2.74), (2.76)

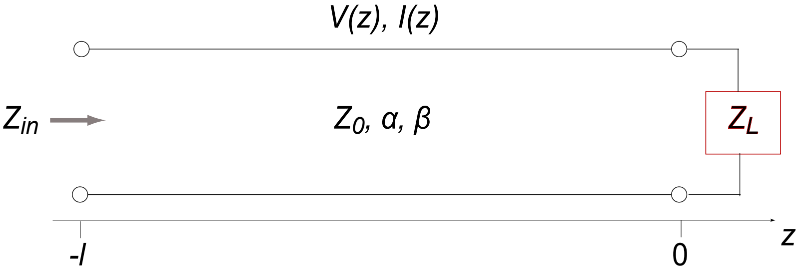

Figure 2.9: A lossy transmission line terminated by a load impedance Z_L.

$$Z_L = \frac{V(0)}{I(0)} = \frac{V_0^+ + V_0^-}{V_0^+ - V_0^-} Z_0. \tag{2.89}$$

Solving for V_0^- gives $V_0^- = \frac{Z_L - Z_0}{Z_L + Z_0} V_0^+$. The voltage reflection coefficient Γ is defined as the amplitude of the reflected voltage divided by the amplitude of the incident voltage

$$\Gamma = \Gamma(\mathrm{z} = 0) = \frac{V_0^-}{V_0^+} = \frac{Z_L - Z_0}{Z_L + Z_0}. \tag{2.90}$$

A matched load is characterized by $Z_L = Z_0$. $\Gamma = 0$ then means, that waves incident on the load Z_L are not reflected.

The so called return loss RL is defined by $RL = -20 \log \mid \Gamma \mid$ dB. In the case of a matched load, $RL \to \infty$ dB.

Using Γ, $V(z)$ and $I(z)$ can be expressed by

$$V(z) = V_0^+ \left[e^{-\gamma z} + \Gamma e^{\gamma z}\right], \tag{2.91}$$

$$I(z) = \frac{V_0^+}{Z_0} \left[e^{-\gamma z} - \Gamma e^{\gamma z}\right]. \tag{2.92}$$

The input impedance Z_{in} at a distance l from the load impedance Z_L is then given by

$$Z_{in} = \frac{V(-l)}{I(-l)} = Z_0 \frac{Z_L + Z_0 \tanh(\gamma\, l)}{Z_0 + Z_L \tanh(\gamma\, l)}. \tag{2.93}$$

One can also generalize $\Gamma = \Gamma(z = 0)$ to any point $z = -l$:

$$\Gamma(l) = \frac{V_0^+ \Gamma e^{-\gamma l}}{V_0^+ e^{\gamma l}} = \Gamma e^{-2\gamma l} \tag{2.94}$$

Two cases will be of special interest for the transmission line analysis of the hybrid ring: a

short ($Z_L = 0$) and an open ($Z_L = \infty$) load.
For these cases, (2.93) becomes

$$Z_{in}^{sc} = \lim_{Z_L \to 0} \left(Z_0 \frac{Z_L + Z_0 \tanh(\gamma\, l)}{Z_0 + Z_L \tanh(\gamma\, l)} \right) = Z_0 \tanh(\gamma\, l) \quad \text{for a short,} \tag{2.95}$$

$$Z_{in}^{oc} = \lim_{Z_L \to \infty} \left(Z_0 \frac{Z_L + Z_0 \tanh(\gamma\, l)}{Z_0 + Z_L \tanh(\gamma\, l)} \right) = Z_0 \coth(\gamma\, l) \quad \text{for an open.} \tag{2.96}$$

The inverse of the impedance is called admittance $Y = 1/Z$. One then speaks about input admittances as well as characteristic admittances.

2.2.7 Theory of Small Reflections and Tapered Lines

In this section, a very simple but very important concept for designing complex microwave structures is presented. The theory of small reflections. When designing a microwave circuit, one often has the problem of impedance matching, when connecting a load with impedance Z_L to a transmission line with characteristic impedance Z_0. Reflections occur if Γ in (2.90) is non zero, i.e. $Z_L \neq Z_0$. To avoid reflections in the case $\Gamma \neq 0$, one has to place a matching network between the load and the transmission line. As long as the load impedance Z_L has some non zero real part, a matching network can always be found [4]. Numerous publications exist about the different realizations of matching networks for microwave applications, see e.g. references [3,4,13]. When realizing a matching network, one has to deal with the following aspects: Complexity, bandwidth, implementation and adjustability. It would go far beyond the scope of this work to treat the matching network problem in great detail and generality. The discussion given here is thus restricted to tapered lines, as they are a useful tools for impedance matching in coplanar waveguide structures, focusing on the requirements of the present work. They are simple to design, have accurate bandwidth and their implementation is quite easy. They are not tunable, but this is not needed, as the operating frequency of the experiment is well defined and restricted by the design and performance of the hybrid ring.

To understand the principle of tapered lines, it is useful to refer to the theory of small reflections which is very similar to the Born approximation in quantum mechanics. To get the total reflection coefficient Γ of an arbitrary impedance $Z(z)$ for $0 \leq z \leq L$, one sums up the incremental reflection coefficients $\Delta\Gamma(z)$ that occurs because of infinitesimal impedance mismatches $\Delta Z(z)$ along the infinitesimal distance Δz. The situation is shown in Figure 2.10.

$\Delta\Gamma(z)$ can be expressed quantitatively refering to (2.90)

$$\Delta\Gamma(z) = \frac{(Z(z) + \Delta Z(z)) - Z(z)}{(Z(z) + \Delta Z(z)) + Z(z)} \simeq \frac{\Delta Z(z)}{2Z(z)}. \tag{2.97}$$

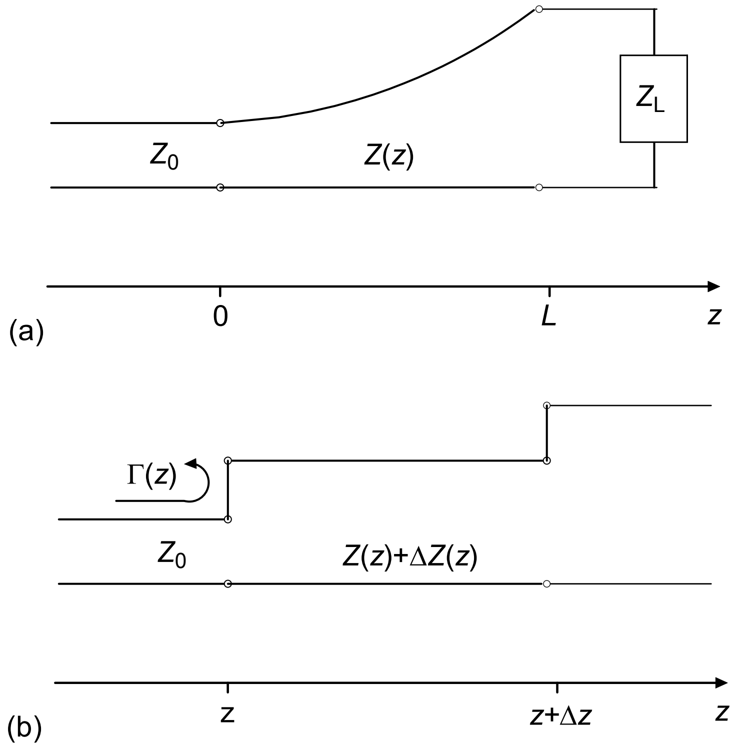

Figure 2.10: A tapered transmission line matching section and the model for the tapered line. (a) The tapered transmission line matching section. (b) Model for an incremental step change in impedance of the tapered line.

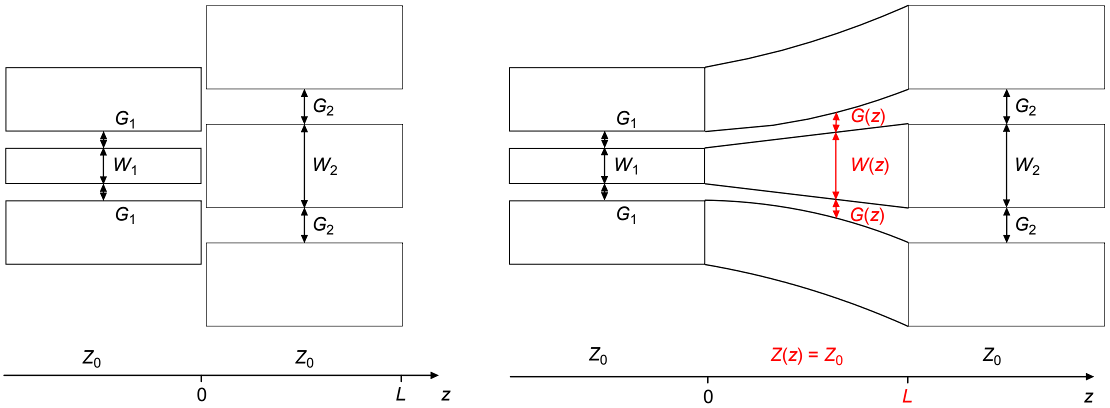

Figure 2.11: (a) Illustration of a design problem, where two coplanar waveguide transmission lines with the same characteristic impedance Z_0, but with very different geometries have to be interconnected. (b) The solution for problem (a) may be tapered lines as shown schematically. $W(z)$ and $G(z)$ should be chosen to assure $Z(z) = Z_0$ along the complete transmission line.

In the limit $\Delta z \to 0$, an exact differential is obtained

$$d\Gamma(z) = \frac{dZ(z)}{2Z(z)} = \frac{1}{2}\frac{d(\ln Z(z)/Z_0)}{dz}dz, \tag{2.98}$$

since

$$\frac{d(\ln f(z))}{dz} = \frac{1}{f}\frac{df(z)}{dz}. \tag{2.99}$$

The total reflection coefficient at $z = 0$ can be found by summing all the partial reflections $d\Gamma(z)$ together with the appropriate phase shifts

$$\Gamma(\theta) = \frac{1}{2}\int_{z=0}^{L} e^{-2j\beta z}\frac{d}{dz}\ln\frac{Z(z)}{Z_0}dz, \tag{2.100}$$

where $\theta = 2\beta l$. $Z(z)$ may be designed, so that $\Gamma(\theta)$ gets minimal for a given operation frequency, Z_L, L and Z_0. For coplanar wave guides, this can be achieved by adjusting the aspect ratio adequately.

A trivial but often occurring problem is the case of two coplanar waveguide transmission lines with the same characteristic impedance Z_0, but with very different geometries as shown for example in Figure 2.11. Connecting these structures directly would result in a short cut or at least a huge geometrical discontinuity with reflections, losses into parasitic modes or even radiative losses. Therefore, one inserts a piece of coplanar wave guide which varies in geometry, but has a characteristic impedance of $Z(z) = Z_0$ along the whole distance $0 \leq z \leq L$, resulting in $\Gamma(\theta) = 0$ referring to (2.100). $Z(z) = Z_0$ has to be ensured

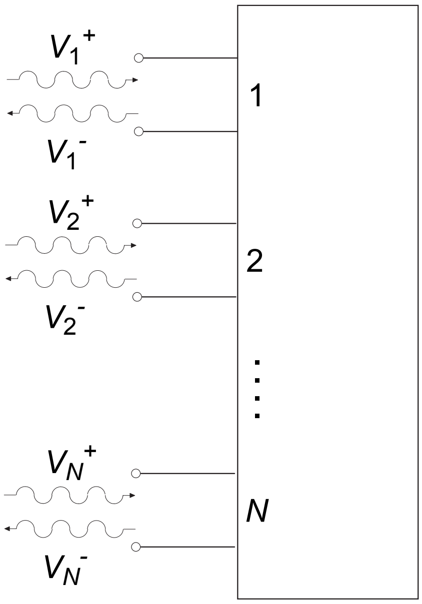

Figure 2.12: Arbitrary N-port network.

by appropriate choice of $W(z)$ and $G(z)$ (see also section 2.4.2).

The model of small reflections is only an approximation as in reality, tapered lines are always a kind of discontinuity, giving rise to reflections. To model a discontinuity more exactly, other methods have to be applied. A very instructive treatment of a CWG T-junction discontinuity with air bridges is given in [14]. There, discontinuities are modelled as extra inductances or capacitances in an equivalent circuit representation. The extra inductances or capacitances are calculated in the quasi static approximation using the spectral domain formulation [15] in conjunction with the method of moments [16].

2.2.8 The Scattering Matrix

To compare an experiment to theory and vice versa, the so called scattering matrix is a very helpful tool. As we will make intense use of the scattering matrix in experiment, theory and numerical simulations, its concept will be briefly introduced here.

Solving Maxwell's equations for a given microwave circuit reveals all information about a system. But for complex systems, this is not always possible and relevant. Instead, it is often sufficient to know only global values about the behaviour of a certain microwave component by considering it as a black box with N microwave connectors as shown in Figure 2.12.

Such a device is then called N-port network. It can be characterized by a $N \times N$ matrix called scattering matrix $S = S_{mn}$ that gives the ratio between the amplitude of the voltage wave V_n^+ incident on port n and the amplitude of the voltage wave V_m^- transmitted to port m (Note, if $m = n$, V_n^- is the amplitude of the voltage wave reflected from port n).

The scattering matrix can be written as follows:

$$\begin{bmatrix} V_1^- \\ V_2^- \\ \vdots \\ V_N^- \end{bmatrix} = \begin{bmatrix} S_{11} & S_{12} & \cdots & S_{1N} \\ S_{21} & S_{22} & \cdots & S_{2N} \\ \vdots & \cdots & \cdots & \vdots \\ S_{N1} & S_{N2} & \cdots & S_{NN} \end{bmatrix} \begin{bmatrix} V_1^+ \\ V_2^+ \\ \vdots \\ V_N^+ \end{bmatrix} \tag{2.101}$$

or in short form

$$[V^-] = [S][V^+] \tag{2.102}$$

where

$$S_{mn} = \frac{V_m^-}{V_n^+}\bigg|_{V_l^+=0,\, for\ l\neq n}. \tag{2.103}$$

Experimentally, S_{mn} (also referred to as S-parameter) can be determined by driving port n with an incident wave of voltage V_n^+ and measuring the wave amplitude V_m^- at port m. The incident wave amplitudes at all other ports $l \neq n$ have to be zero. Therefore, these ports have to be terminated by matched loads in order to avoid reflections that could contribute to the measured scattering matrix element S_{mn}.

It is important to emphasize that the reflection coefficient Γ looking into port n is not equal to S_{nn}, unless all other ports are matched. Similarly, the transmission coefficient from port m to port n is not equal to S_{nm}, unless all other ports are matched. The S-parameters of a network are inherent properties of the network, and are *defined* under the condition that all ports are matched.

S-parameter measurements can be performed in frequency and time domain using a network vector analyzer (NVA). A short explanation of the functionality of a NVA can be found in reference [4]. For a more detailed introduction see references [17] and [18].

For the practical work with a NVA, it is important to know how to convert S-parameters from linear scale (as defined in this section) to S-parameters given in dB (as normally done in practical microwave engineering). The conversions are defined as

$$\begin{aligned} S[dB]_{mn} &\equiv 20 \cdot \log(|S_{mn}|) = 20 \cdot \log(|V_m^-/V_n^+|) && (2.104) \\ S[dB]_{mn} &\equiv 10 \cdot \log(|P_m^-/P_n^+|) = 10 \cdot \log(|V_m^{-2}R/V_n^{+2}R|) && (2.105) \\ &= 10 \cdot \log(|V_m^-/V_n^+|)^2 && (2.106) \\ |S_{mn}| &\equiv 10^{\frac{S[dB]_{mn}}{20}} && (2.107) \end{aligned}$$

For a reciprocal network, the S matrix is symmetric ($S^T = S$). The S matrix for a lossless network is unitary ($S^\dagger = S^{-1}$).

In the case of a two-port network, it makes sense to define a so called transmission or *ABCD* matrix. It is very useful when connecting several two-port networks in series. Such

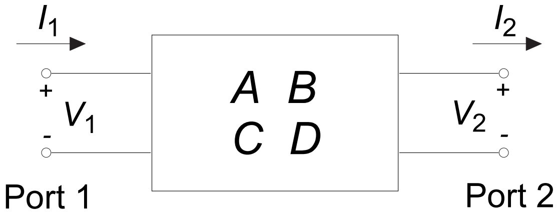

Figure 2.13: Two-port network and corresponding total voltages and currents used for the definition of the *ABCD* matrix.

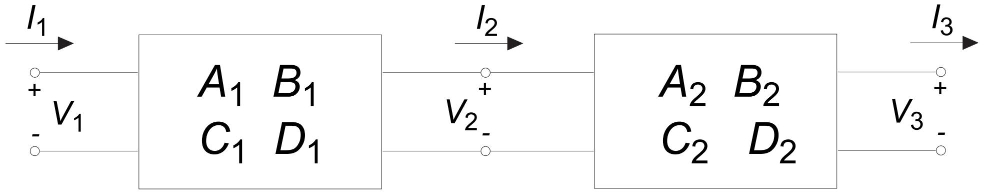

Figure 2.14: A cascade of two two-port networks and corresponding total voltages and currents used for the calculation of the ABCD matrix of the cascade of networks.

a cascade of two-port networks can be described by the product of the *ABCD* matrices of the connected two-port networks. The *ABCD* matrix is defined in terms of the total voltages and currents as shown in Figure 2.13 by

$$V_1 = A\, V_2 + B\, I_2, \tag{2.108}$$

$$I_1 = C\, V_2 + D\, I_2. \tag{2.109}$$

In matrix form it can be written as

$$\begin{bmatrix} V_1 \\ I_1 \end{bmatrix} = \begin{bmatrix} A & B \\ C & D \end{bmatrix} \begin{bmatrix} V_2 \\ I_2 \end{bmatrix} \tag{2.110}$$

.

Note that this definition differs from the definition of the scattering matrix. In a cascade of two-port networks as shown in Figure 2.14, the current I_2 flows *out* of port 2 of network one *into* port 2 of the the second network.

Therefore the ABCD matrix of the whole cascade may be found by matrix multiplication such as

$$\begin{aligned}\begin{bmatrix} V_1 \\ I_1 \end{bmatrix} = \begin{bmatrix} A_1 & B_1 \\ C_1 & D_1 \end{bmatrix} \begin{bmatrix} V_2 \\ I_2 \end{bmatrix} &= \begin{bmatrix} A_1 & B_1 \\ C_1 & D_1 \end{bmatrix} \begin{bmatrix} A_2 & B_2 \\ C_2 & D_2 \end{bmatrix} \begin{bmatrix} V_3 \\ I_3 \end{bmatrix} \\ &= \begin{bmatrix} A & B \\ C & D \end{bmatrix} \begin{bmatrix} V_3 \\ I_3 \end{bmatrix}, \end{aligned} \tag{2.111}$$

where $\begin{bmatrix} A & B \\ C & D \end{bmatrix}$ is the *ABCD* matrix of the cascade of the two networks. It can be shown that the scattering matrix S of the whole system can be calculated from the *ABCD* matrix by the following formulas:

$$S_{11} = \frac{A + B/Z_0 - CZ_0 - D}{A + B/Z_0 + CZ_0 + D} \tag{2.112}$$

$$S_{12} = \frac{2(AD - BC}{A + B/Z_0 + CZ_0 + D} \tag{2.113}$$

$$S_{21} = \frac{2}{A + B/Z_0 + CZ_0 + D} \tag{2.114}$$

$$S_{22} = \frac{-A + B/Z_0 - CZ_0 + D}{A + B/Z_0 + CZ_0 + D} \tag{2.115}$$

Also used in electrical engineering are the impedance matrix [Z] and the admittance matrix [Y]. The definition of [Z] is

$$\begin{bmatrix} V_1 \\ V_2 \\ \vdots \\ V_N \end{bmatrix} = \begin{bmatrix} Z_{11} & Z_{12} & \cdots & Z_{1N} \\ Z_{21} & Z_{22} & \cdots & Z_{2N} \\ \vdots & \cdots & \cdots & \vdots \\ Z_{N1} & Z_{N2} & \cdots & Z_{NN} \end{bmatrix} \begin{bmatrix} I_1 \\ I_2 \\ \vdots \\ I_N \end{bmatrix}, \tag{2.116}$$

or in short form

$$[V] = [Z][I], \tag{2.117}$$

where

$$Z_{ij} = \frac{V_i}{I_j}\Big|_{I_k=0 for\ k\neq j}, \tag{2.118}$$

and V_n and I_n are the total voltage and current at the nth port

$$V_n = V_n^+ + V_n^- \qquad \text{and} \qquad I_n = I_n^+ + I_n^-. \tag{2.119}$$

The definition of [Y] in short form is given by:

$$[I] = [Y][V]. \tag{2.120}$$

2.3 Transmission Line Theory of the Hybrid Ring

In the following section, the hybrid ring will be modelled by using the transmission line theory. This theory can be applied as the characteristic wavelengths of microwaves are of the order of the hybrid ring dimensions, as it will be figured out.
A schematic representation of the hybrid ring is shown in Figure 2.15. The ports are numbered clockwise from 1 to 4. The arms of the ring are assumed to be equal in length and in their characteristic impedance $Z_c = 1/Y_c$. The CWG ring has the impedance $Z_1 = 1/Y_1$. The phase difference of a wave propagating on the ring is $\theta_1 = \beta U/6 = \beta 2\pi R/6$ between ports 1 and 2, 2 and 3, 3 and 4. Here, R is the Radius of the ring and U the circumference. β is the wave vector of a wave propagating on the ring. The ring is symmetric with respect to the plane E.
In the case where $\theta_1 = \pi/2$ the phase difference between ports 1 and 4 becomes $\theta_2 = 3\theta_1$. The operating principle of the ring is easy to understand for this special case, which is also shown in Figure 2.15 (b):
A wave incident on port 1 will be split into two components with the same amplitude, one wave travelling clockwise, the other one counter clockwise around the ring. The amplitude of these two waves is $1/\sqrt{2}$ (= 3 dB) times the amplitude of the incident wave to fulfil energy conservation. When one chooses $\theta_1 = \pi/2$ and $\theta_2 = 3\pi/2$, then the two waves will interfere constructively at ports 2 and 4 and destructively at port 3. As a consequence Ports 2 and 4 are 3-dB coupled to port 1, whereas port 3 is isolated from port 1.
To understand the frequency behaviour of the hybrid ring, it may be investigated using transmission line theory. To find a lumped circuit representation of the hybrid ring, one makes use of its symmetry. For this reason, it is useful to investigate a symmetric and an antisymmetric excitation of the hybrid in reference to the symmetry plane E shown in Figure 2.15 (a). Once having found the corresponding S-parameters, the solutions can be superimposed to determine the full S matrix of the hybrid ring for a general excitation.

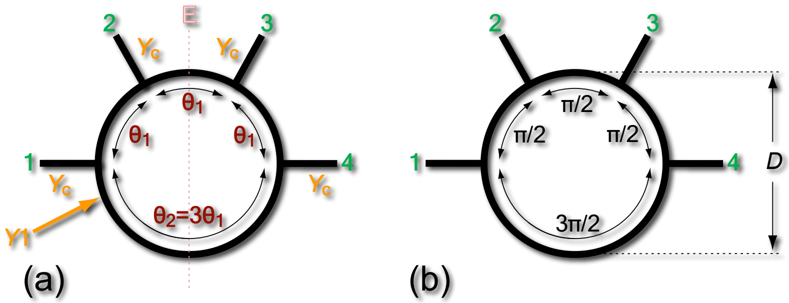

Figure 2.15: Schematic of the 180° hybrid ring, also called rat race. (a) General case. Also shown, the symmetry plane E of the hybrid ring. (b) Case of constructive interference at ports 2 and 4 of a wave incident on port 1. For this case, the wave incident on port 1 interferes destructively at port 3.

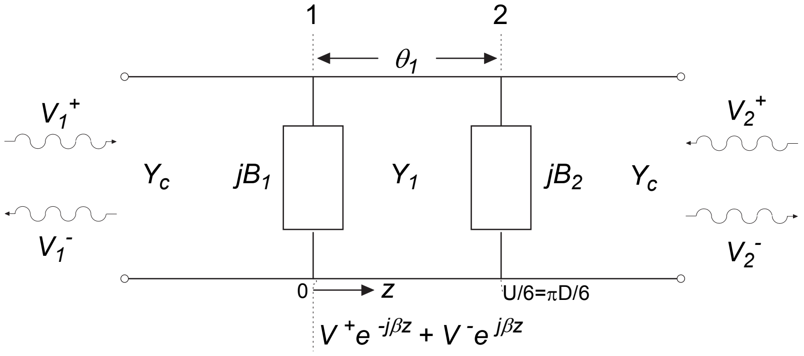

Figure 2.16: Equivalent lumped circuit model used to find the two-port S matrix parameters for one-half of the hybrid ring.

In the case of an antisymmetric excitation

$$V_4^+ = -V_1^+ \quad \text{and} \quad V_3^+ = -V_2^+, \tag{2.121}$$

the electric fields at the symmetry plane E must be zero, i.e. E is acting as a perfectly electrically conducting (PEC) wall causing short cuts at the intersection points of the plane E with the hybrid ring. It is then sufficient to solve the problem only on one side of plane E, for example the left side. Hence, the four port element reduces to a two-port element. The corresponding lumped circuit model is shown in Figure 2.16.

In the case of an antisymmetric excitation, input port 1 in Figure 2.16 is shunted by an admittance $jB_1 \equiv jB_1^{sc} = -jY_1 \cot 3\theta_1/2$ due to the short cut at the end of the section of the hybrid ring having an electrical length of $3\theta_1/2$. The output port 2 is shunted by an admittance $jB_2 \equiv jB_2^{sc} = -jY_1 \cot \theta_1/2$ due to the short at the end of the section of the hybrid ring with an electrical length of $\theta_1/2$. The hybrid ring section between these two admittances is modeled as a transmission line with an electrical length θ_1 and the same characteristic admittance Y_1. Also shown are the incident and scattered wave amplitudes V_n^+ and V_n^- for port $n = 1$ or $n = 2$. The scattering matrix of this two-port element can therefore be written as

$$\begin{bmatrix} V_1^- \\ V_2^- \end{bmatrix} = \begin{bmatrix} S_{11}^{sc} & S_{12}^{sc} \\ S_{21}^{sc} & S_{22}^{sc} \end{bmatrix} \begin{bmatrix} V_1^+ \\ V_2^+ \end{bmatrix}. \tag{2.122}$$

For the other half of the hybrid ring, one can deduce from the symmetry conditions (2.121) and the fact that the hybrid is excited anti symmetric

$$\begin{bmatrix} V_4^- \\ V_3^- \end{bmatrix} = \begin{bmatrix} S_{11}^{sc} & S_{12}^{sc} \\ S_{21}^{sc} & S_{22}^{sc} \end{bmatrix} \begin{bmatrix} V_4^+ \\ V_3^+ \end{bmatrix} = \begin{bmatrix} S_{11}^{sc} & S_{12}^{sc} \\ S_{21}^{sc} & S_{22}^{sc} \end{bmatrix} \begin{bmatrix} -V_1^+ \\ -V_2^+ \end{bmatrix}, \tag{2.123}$$

since port 4 corresponds to port 1 and port 3 to port 2.

In the case of a symmetric excitation

$$V_4^+ = V_1^+ \quad \text{and} \quad V_3^+ = V_2^+, \tag{2.124}$$

the magnetic fields at the symmetry plane E must be zero, i.e. E is acting as a perfectly magnetically conducting wall causing an open at the intersection points of the plane E with the hybrid ring. For this reason, the shunt admittances have to be changed. jB_1^{sc} is replaced by $jB_3^{oc} = jY_1 \tan 3\theta_1/2$ and jB_2^{sc} is replaced by $jB_4^{oc} = jY_1 \tan \theta_1/2$. For this case, the scattering matrix writes

$$\begin{bmatrix} V_1^- \\ V_2^- \end{bmatrix} = \begin{bmatrix} S_{11}^{oc} & S_{12}^{oc} \\ S_{21}^{oc} & S_{22}^{oc} \end{bmatrix} \begin{bmatrix} V_1^+ \\ V_2^+ \end{bmatrix} \tag{2.125}$$

and

$$\begin{bmatrix} V_4^- \\ V_3^- \end{bmatrix} = \begin{bmatrix} S_{11}^{oc} & S_{12}^{oc} \\ S_{21}^{oc} & S_{22}^{oc} \end{bmatrix} \begin{bmatrix} V_4^+ \\ V_3^+ \end{bmatrix} = \begin{bmatrix} S_{11}^{oc} & S_{12}^{oc} \\ S_{21}^{oc} & S_{22}^{oc} \end{bmatrix} \begin{bmatrix} V_1^+ \\ V_2^+ \end{bmatrix}. \tag{2.126}$$

If one now superimposes the antisymmetric (2.122 + 2.123) and the symmetric (2.125 + 2.126) excitations, one can deduce eight of the 16 parameters of the entire scattering matrix for a general excitation:

$$\begin{bmatrix} V_1^- \\ V_2^- \end{bmatrix} = \frac{1}{2} \begin{bmatrix} S_{11}^{oc} + S_{11}^{sc} & S_{12}^{oc} + S_{12}^{sc} \\ S_{21}^{oc} + S_{21}^{sc} & S_{22}^{oc} + S_{22}^{sc} \end{bmatrix} \begin{bmatrix} V_1^+ \\ V_2^+ \end{bmatrix} = \begin{bmatrix} S_{11} & S_{12} \\ S_{21} & S_{22} \end{bmatrix} \begin{bmatrix} V_1^+ \\ V_2^+ \end{bmatrix}, \tag{2.127}$$

and

$$\begin{bmatrix} V_4^- \\ V_3^- \end{bmatrix} = \frac{1}{2} \begin{bmatrix} S_{11}^{oc} - S_{11}^{sc} & S_{12}^{oc} - S_{12}^{sc} \\ S_{21}^{oc} - S_{21}^{sc} & S_{22}^{oc} - S_{22}^{sc} \end{bmatrix} \begin{bmatrix} V_1^+ \\ V_2^+ \end{bmatrix} = \begin{bmatrix} S_{41} & S_{42} \\ S_{31} & S_{32} \end{bmatrix} \begin{bmatrix} V_1^+ \\ V_2^+ \end{bmatrix}. \tag{2.128}$$

The rest of the 16 scattering matrix parameters is obtained by symmetry considerations: $S_{11} = S_{44}$, $S_{22} = S_{33}$, $S_{12} = S_{43} = S_{34}$, $S_{32} = S_{23}$, $S_{31} = S_{13}$, $S_{41} = S_{14}$ and $S_{42} = S_{24}$. Now it remains to find the two-port scattering-matrix elements $S_{12}^{sc} = S_{21}^{sc}$, S_{11}^{sc}, S_{22}^{sc} and $S_{12}^{oc} = S_{21}^{oc}$, S_{11}^{oc}, S_{22}^{oc}, respectively, for the lumped element circuit in Figure 2.16.
On the connecting line with characteristic length θ_1 and characteristic admittance Y_1 we assume the existence of a forward and backward propagating wave $V^+e^{-j\beta z} + V^-e^{j\beta z}$ with associated current waves $V^+Y_1e^{-j\beta z} - V^-Y_1e^{j\beta z}$.

The continuity of the voltage at ports 1 and 2 gives

$$V_1^+ + V_1^- = V^+ + V^-, \tag{2.129}$$

$$V_2^+ + V_2^- = V^+e^{-j\theta_1} + V^-e^{j\theta 1}, \tag{2.130}$$

whereas the continuity of the current at the ports gives

$$(V_1^+ - V_1^-)Y_c = (V^+ - V^-)Y_1 + (V_1^+ + V_1^-)jB_1, \tag{2.131}$$

$$(V^+e^{-j\theta_1} - V^-e^{j\theta 1})Y_1 = -(V_2^+ - V_2^-)Y_c + (V_2^+ + V_2^-)jB_2. \tag{2.132}$$

Solving (2.129) for V^+ and V^- and substituting the solutions in (2.131) allows to solve for V_1^- and V_2^- in terms of V_1^+ and V_1^+ and thus to calculate the two-port scattering matrix parameters for the antisymmetric case. After a lengthy calculation, one obtains

$$S_{11}^{sc} = \frac{1}{\Delta}\Big[Y_c^2 - Y_1^2 + B_1B_2 - Y_1(B_1 + B_2)\cot\theta_1 + jY_c(B_2 - B_1)\Big], \tag{2.133}$$

$$S_{12}^{sc} = S_{21}^{oc} = -\frac{2jY_cY_1\csc\theta_1}{\Delta}, \tag{2.134}$$

$$S_{22}^{sc} = S_{11}^{oc} + \frac{2jY_c(B_1 - B_2)}{\Delta}, \tag{2.135}$$

$$\tag{2.136}$$

where

$$\Delta = Y_c^2 - B_1B_2 + Y_1(B_1 + B_2)\cot\theta_1 + Y_1^2 + jY_c(B_1 + B_2 - 2Y_1\cot\theta_1),$$
$$B_1 = -Y_1\cot\tfrac{3\theta_1}{2} \qquad \text{and} \qquad B_2 = -Y_1\cot\tfrac{\theta_1}{2}.$$

To get S_{11}^{oc}, S_{22}^{oc} and $S_{12}^{oc} = S_{21}^{oc}$ one has to replace B_1 by $B_3 = Y_1\tan\frac{3\theta_1}{2}$ and B_2 by $B_4 = Y_1\tan\frac{\theta_1}{2}$.

For the special case $\theta_1 = \pi/2$, the terms simplifies to

$$S_{11} = S_{22} = S_{33} = S_{44} = \frac{Y_c^2 - 2Y_1^2}{Y_c^2 + 2Y_1^2}, \tag{2.137}$$

$$S_{31} = S_{42} = 0, \tag{2.138}$$

$$S_{21} = S_{43} = -S_{41} = S_{32} = \frac{-2jY_cY_1}{Y_c^2 + 2Y_1^2}. \tag{2.139}$$

As expected the ports 1 and 3 are isolated from each other. Ports 2 and 4 are both coupled to port 1, but there is a phase difference of π between ports 2 and 4 as $S_{21} = -S_{41}$.
The input reflection parameters S_{ii} are zero (meaning that there is no return loss at ports 1 to 4 if $Y_c^2 - 2Y_1^2 = 0$ or

$$Z_1 = \sqrt{2}Z_c. \tag{2.140}$$

If (2.140) is valid, then $|S_{21}| = |S_{41}| = \sqrt{1/2}$. This means that power entering the hybrid ring at port 1 is equally divided and transmitted without losses to port 2 and port 4. One obtains the four-port scattering-matrix of a so called 3-dB directional coupler or 180° hybrid junction:

$$[S] = \frac{-j}{\sqrt{2}} \begin{bmatrix} 0 & 1 & 0 & -1 \\ 1 & 0 & 1 & 0 \\ 0 & 1 & 0 & 1 \\ -1 & 0 & 1 & 0 \end{bmatrix}. \tag{2.141}$$

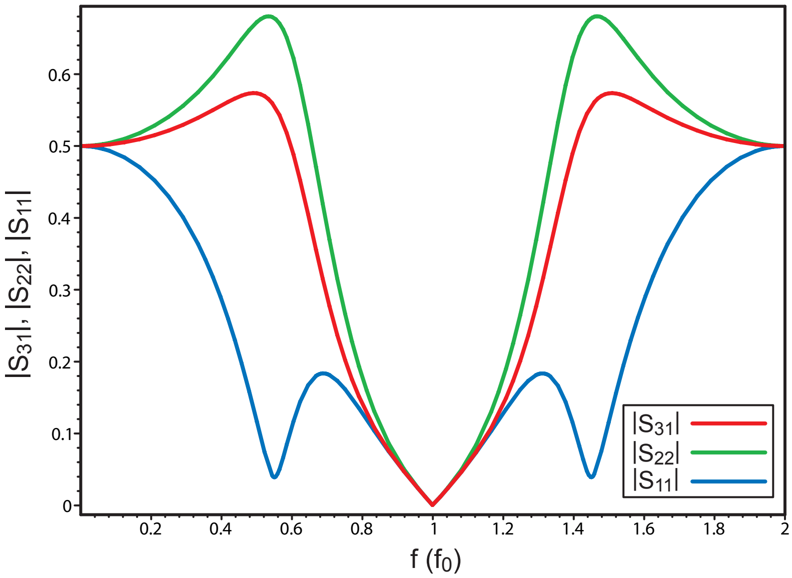

Figure 2.17: $|S_{11}|$- , $|S_{22}|$- and $|S_{31}|$-parameters for the hybrid ring calculated by transmission line theory as a function of frequency.

For arbitrary θ_1, the resulting S-parameters can be plotted as shown in Figure 2.17 and 2.18 as a function of a non dimensional frequency $f/f_0 = 2\theta_1/\pi$, where f_0 is the operation frequency f_0 of the hybrid ring. f_0 only depends on the diameter D of the hybrid ring (see Figures 2.15 and 2.16):

$$f_0 = \frac{v_p}{\lambda_0} = \frac{v_p \beta_0}{2\pi} = \frac{6 v_p \theta_1}{2D\pi^2} = \frac{3 v_p}{2D\pi}. \tag{2.142}$$

In Figure 2.19 the function $F(\theta_1) = |1/4\cos(\theta_1\pi) + 1/4\cos(2\theta_1\pi)|$ is plotted. F represents two superposed waves with the same amplitude of 1/4 but with arguments that differ by a factor of 2. This function has a minimum at $f/f_0 = 1$ as well as the $|S_{31}|$-parameter of the hybrid ring. On the other hand, this model of the two superposed waves describes the behaviour of the hybrid ring only for $f = f_0$. For other frequencies, the behaviour of the hybrid is of course more complicated. So far, dissipative losses have been neglected. They can be taken into account by the substitution $\beta \to \beta - i\alpha$ as shown in section 2.2.6.2.

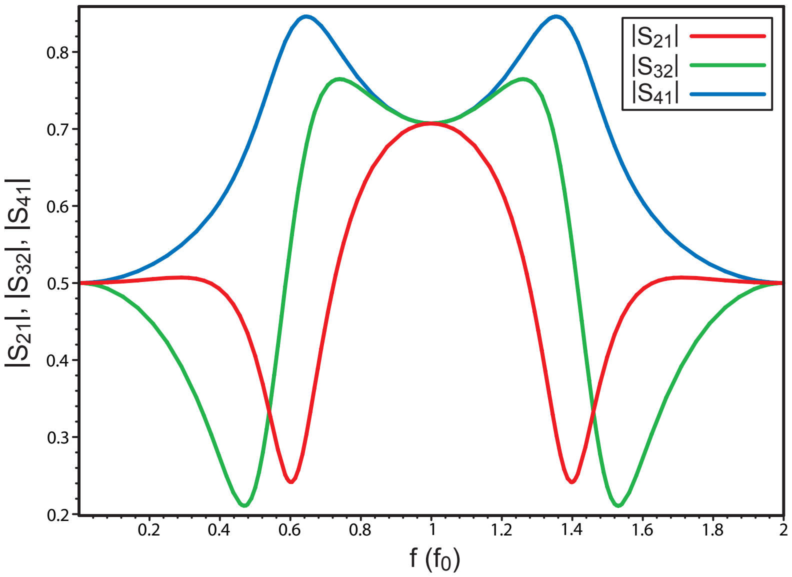

Figure 2.18: $|S_{21}|$-, $|S_{32}|$- and $|S_{41}|$-parameters for the hybrid ring calculated by transmission line theory as a function of frequency.

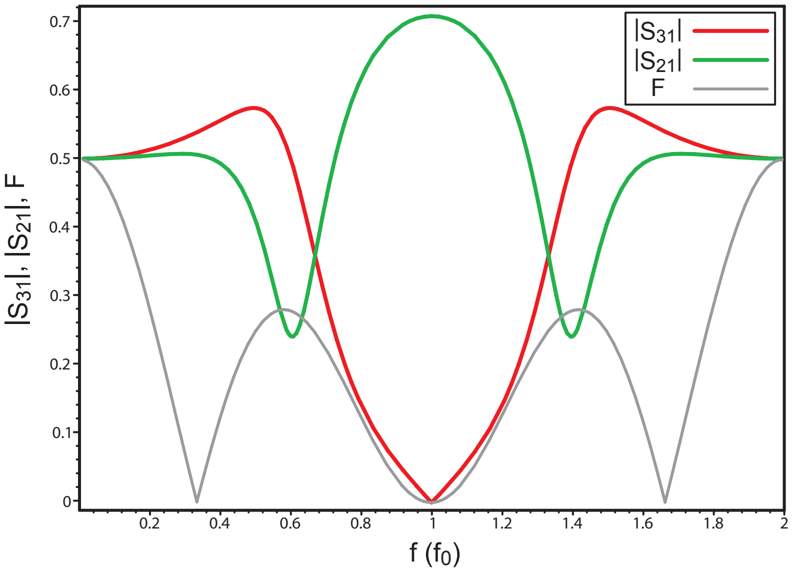

Figure 2.19: $|S_{31}|$- and $|S_{21}|$-parameters for the hybrid ring calculated by transmission line theory in comparison to function F (see text).

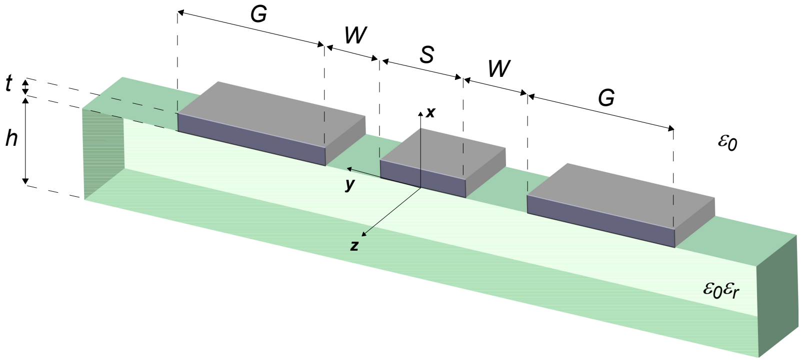

Figure 2.20: Cross section of a conventional coplanar wave guide with finite-extend ground planes.

2.4 Theory of Superconducting Coplanar Waveguides

The transmission line theory of the hybrid ring in the previous section was developed independently of a concrete realization of the transmission lines. In this section, accurate formulas will be presented for the calculation of characteristic properties of superconducting (SC) coplanar waveguides (CWGs), such as characteristic impedance and propagation constant. Furthermore, losses and dispersion within SC CWGs will be treated, too.

Only some words will be spent on the numerous ways to mathematically treat of CWGs as it would by far exceed the scope of this work. The interested reader may find further information about different types of CWGs and references to publications on their appropriate mathematical treatment in reference [19].

Explicit numerical simulations used to extract the characteristic properties of CWGs will be presented in Chapter 3.

2.4.1 Introduction

The CWG was first proposed in the Ph.D. thesis of R. F. Frazita in 1965 [20] and by C.P. Wen in 1969 [21]. A CWG consists of a strip of thin metallic film on the surface of a dielectric slab with two infinite-extended ground planes running adjacent and parallel to the strip. In practice, finite-extend ground planes are normally used, as seen in Figure 2.20. In addition to this basic structure, one can find several variations. Important within this work is especially a conductor-backed coplanar waveguide shielded by a top metal cover as seen in Figure 2.21.

Beside microstrip transmission lines, CWGs have been the most studied transmission lines because of their quasi-TEM propagation mode and their planar structure [22–25]. CWGs offer several advantages:

- simple fabrication,
- facilitation of shunt and series surface mounting of active and passive devices,

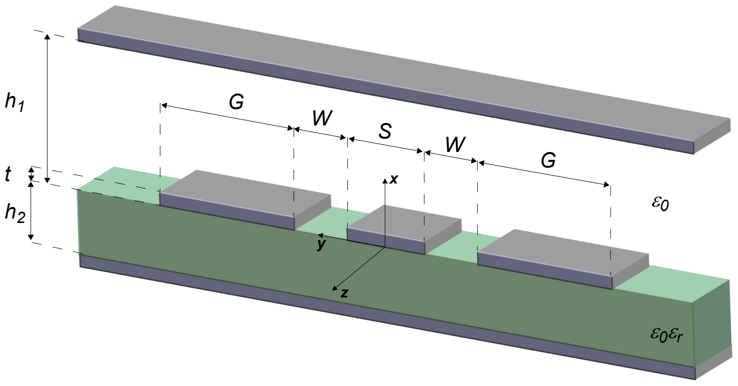

Figure 2.21: Cross section of a conductor-backed coplanar wave guide with a top metal cover.

- no need for wraparound and via holes,
- reduction of radiation loss [26],
- possibility of size reduction as the characteristic impedance is predominantly determined by the aspect ratio $S/(S+2W)$ (expecting higher losses [19]),
- and finally the possibility to pack different transmission lines closely together [27].

As a result, CWGs are ideally suited for microwave integrated circuit (MIC) as well as monolithic microwave integrated circuit (MMIC) applications.

Moreover, a controllable strong coupling between a superconducting CWG resonator and a charge or flux Qubit is possible as shown in Chapter 1 and [28]. This makes (superconducting) CWGs also ideally suited for applications in quantum information processing and quantum information communication in the microwave regime at cryogenic temperatures.

In general, one can distinguish between two main concepts of treating a CWG mathematically: a quasi static approach (see e.g. [27, 29–33]) where one assumes the frequency of the propagating electromagnetic waves to be almost zero and full-wave or spectral-domain methods (see e.g. [34–37]) with which characteristic properties can be deduced as a function of frequency.

While full-wave methods are the most accurate tools for obtaining transmission line characteristics but are analytically extensive, quasi static methods are quite simple and lead to closed-form expressions suitable for computer-aided design (CAD) software packages. However they do not consider the dispersive nature of generic transmission lines. Consequently, the approximation of quasi static methods becomes worse as the transmission line becomes dispersive. However, as in the dispersion analysis of CWG presented by Knorr and Kuchler [34], the CWG parameters are only slightly sensitive to variations of frequency for CWGs with dimensions that do not exceed the substrate thickness over almost the entire microwave region. Therefore, quasi-static methods provide a simulation accuracy that is comparable with full-wave methods for frequencies up to 20 GHz [30]. Present experiments with superconducting quantum devices, do not exceed this frequency limit of 20 GHz, a quasistatic approach can be sufficient by adequately choosing the CWG dimensions. Especially the CWGs fabricated within this work meet the requirements for such an approach as one will see in section 2.4.2.

The number of publications analysing coplanar wave guides is huge. The easiest descriptions are quasi static descriptions. The comparison between the wavelength and the spatial dimensions of the CWG is the most important aspect to consider, as it allows to decide whether a quasi static description is valid or whether a full-wave method has to be chosen. Instead of wavelengths and dimensions, one can also look at characteristic frequencies or time scales of CWGs. The topic of characteristic frequencies and time scales has therefore been treated in a more general way in sections 2.2.3, 2.2.4 and 2.2.5.

2.4.2 Design of Superconducting Coplanar Waveguides

In this section simple formulas will be presented that allow to design CWGs and to obtain an estimation for the most important transmission line parameters as characteristic impedance Z_0 and the complex propagation constant $\gamma = \alpha + i\beta$.

As already mentioned in the introduction of this section, CWGs have been analysed experimentally and theoretically extensively in the last years. A good summary of different types of CWGs and appropriate publications are given in reference [19]. The task for the experimentalist is to choose an adequate model for the CWG. CWGs designed in this thesis have typical transversal dimensions of less than 200 μm and have to support waves with a frequency of less than 10 Ghz. Thus it is possible to apply a quasi static model.

As already seen in section 2.2.3, another characteristic time or length scale is given by the skin depth δ_s or London penetration depth λ_L for normal and superconducting CWGs, respectively. In a typical CWG, its thickness t can be referred to one of these characteristic length scales.

Very often, quasi static models treat the attenuation constant α and the propagation constant β separately, by doing assumptions that are not consistent. For the derivation of α, e.g. in reference [3], it is assumed that the thickness t of the metal layer (denoted as *metalization thickness* in the following) is much greater than the skin depth δ_s which is assumed to be unequal to zero because neither ω nor σ are infinite. This makes it possible to apply the bulk surface-impedance concept to the centre strip conductor (see reference [38], chapter 3.16).

On the other hand, for the calculation of β, the thickness is assumed to be zero, making it easier to perform a conformal mapping of the cross section of the CWG. Nevertheless, such an approach is valid as β is not very strongly dependent on the thickness t of the metallization in contrast to α, which one can see exemplary in Figures 2.22 and 2.23 from

reference [39]. Qualitatively, this can be understood when having a look at (2.84) where $\beta \simeq \omega\sqrt{LC}$. Often it is convenient [12] to distinguish between magnetic fields *within* the conductor - contributing according to (2.78) to a so called internal (or kinetic) inductance L_{int} - and fields *outside* the conductor contributing to an external inductance L_{ext}. The internal inductance accounts for magnetic energy storaged within the conductor by means of the kinetic energy of the Cooper pairs. β can then be written as $\beta \simeq \omega\sqrt{LC} = \omega\sqrt{(L_{int} + L_{ext})C}$. If the conductor is thin compared to the other transversal dimensions of the transmission line, the internal magnetic field can be neglected in comparison to the outer field and β is primarily determined by L_{ext}. This argument is not valid for the attenuation constant which is dependent on the series resistance R of the transmission line which gets smaller by increasing the thickness of the conductor according to (2.30), if one takes $t \propto \Delta z$.
Analogously to the inductance, one can separate the characteristic impedance Z_0 into an internal and an external contribution:

$$Z_0 = \sqrt{\frac{L}{C}} = \frac{L}{\sqrt{LC}} = \frac{L}{v_{ph}} \equiv \frac{L_{int}}{v_{ph}} + \frac{L_{ext}}{v_{ph}} = Z_{int} + Z_{ext}, \tag{2.143}$$

where v_{ph} is the phase velocity defined in (2.86). By introducing the effective permittivity ε_{eff}, which is defined as

$$\varepsilon_{\text{eff}} \equiv c^2 v_{ph}^2 \quad (c \text{ is the vacuum speed of light}), \tag{2.144}$$

(2.143) becomes

$$Z_0 = \frac{L\,c}{\sqrt{\varepsilon_{\text{eff}}}} = \frac{L_{int}\,c}{\sqrt{\varepsilon_{\text{eff}}}} + \frac{L_{ext}\,c}{\sqrt{\varepsilon_{\text{eff}}}}. \tag{2.145}$$

β can now be calculated as $\beta \approx (\omega/c)\sqrt{\varepsilon_{\text{eff}}}$.
[40] gives an explicit formula for the kinetic inductance of a conventional superconducting CWG with dimensions given in Figure 2.20:

$$L_{int} = \mu_0 \lambda_L(T) \frac{C}{4ADK(k)} \left[\frac{1.7}{\sinh(t/2\lambda_L(T))} + \frac{0.4}{\sqrt{[(B/A)^2 - 1][1 - (B/D)^2]}} \right], \tag{2.146}$$

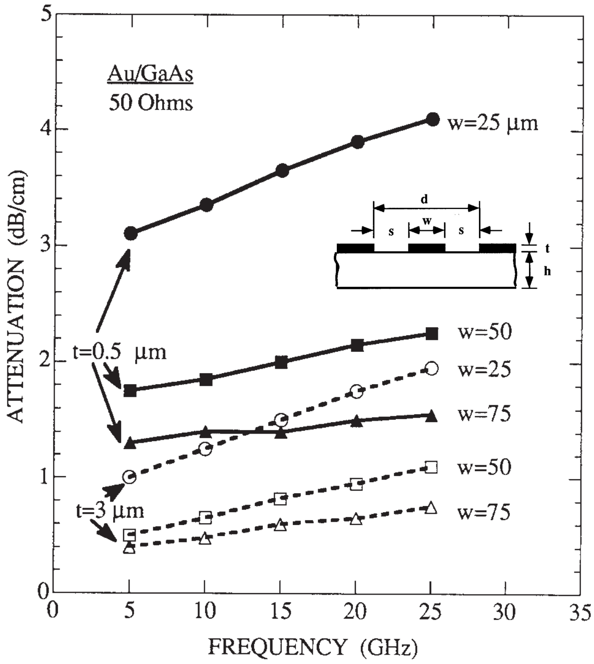

Figure 2.22: Measured impedance for coplanar lines of different dimensions and two metallization thickness on GaAs. The inset shows the geometry parameters: w width of the center strip line, s gap width, $d = w + 2s$, t metalization thickness, h substrate height.

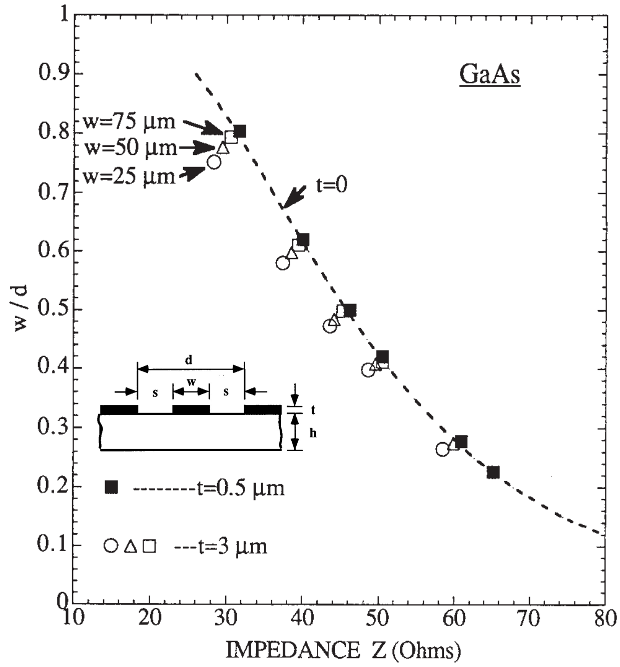

Figure 2.23: Measured attenuation α of coplanar 50 Ω lines on GaAs for two gold metallization thickness. The inset shows the geometry parameters: w width of the center strip line, s gap width, $d = w + 2s$, t metalization thickness, h substrate height.

with

$$
\begin{aligned}
A &= -\frac{t}{\pi} + \frac{1}{2}\sqrt{\left(\frac{2t}{\pi}\right)^2 + S^2}, && (2.147)\\
B &= \frac{S^2}{4A}, && (2.148)\\
C &= B - \frac{t}{\pi} + \sqrt{\left(\frac{t}{\pi}\right)^2 + W^2}, && (2.149)\\
D &= \frac{2t}{\pi} + C, && (2.150)
\end{aligned}
$$

and $K(k)$ is the elliptic integral of the first kind.

This formula is also a very good approximation for the internal inductance for a conductor-backed CWG (see Figure 2.21) as the magnetic fields within the conductor can be considered as independent of the ground-plane as long as the thickness of the dielectric is much larger than the metallization thickness.

Note that – as already mentioned in section 2.2.6 – electric fields within a superconducting transmission line are negligible, when driven below the superelectron plasma frequency. Therefore internal capacitance may be neglected as they are proportional to the square of the electric field E^2.

For the external inductance however, one has to use a formula for a conductor-backed CWG as the external fields are changed significantly by adding an extra ground plane:

$$
\begin{aligned}
\varepsilon_{eff} &= \frac{1 + \varepsilon_r \frac{K(k')}{K(k)} \frac{K(k_3)}{K(k_3')}}{1 + \frac{K(k')}{K(k)} \frac{K(k_3)}{K(k_3')}}, && (2.151)\\
Z_{ext} &= \frac{60\pi}{\sqrt{\varepsilon_{eff}}} \frac{1}{\frac{K(k)}{K(k')} + \frac{K(k_3)}{K(k_3')}}, && (2.152)\\
& && (2.153)
\end{aligned}
$$

where

$$
\begin{aligned}
k &= a/b, && (2.154)\\
k_3 &= \frac{\tanh(\pi a/2h)}{\tanh(\pi b/2h)}, && (2.155)\\
k' &= \sqrt{1 - k^2}, && (2.156)\\
k_3' &= \sqrt{1 - k_3^2}. && (2.157)
\end{aligned}
$$

Further assumptions entering formula () are: zero metallization thickness, infinite ground planes, and the absence of a top metal cover. Following the calculations done in [27], these assumptions are valid under the following restrictions (for dimensions see Figure 2.24):

- Although the minimum cover height needed to avoid significant impedance lowering by the top metal cover depends on the line impedance itself, as a conservative estimate, the cover height should be at least $h_l = 4b$ according to Figure 2.25(a).
- A finite ground-plane width leads to a slight increase of the line impedance with respect to the ideal case ($c \to \infty$, or $b/c \to 0$). The amount of this effect is rather critical, since as is shown in Figure 2.25(b) ($h/b = 1$, b/c ranging from 0.3 to 1.0), for very narrow lateral ground planes, the impedance variation is big. As a conservative estimate, one should have at least $c/b = 4$ in order to ensure a negligible variation.
- For high h/b values, the impedance depends only on a/b. The minimum substrate thickness needed to make the line independent from h depends on the impedance itself. A rough estimate for a 50 Ω-line suggests that $h/b > 3$ is a reasonable assumption. The error with respect to $h/b \to \infty$ is less than 2 percent, see Figure 2.25(c).

G. Ghione and C. U. Naldi [27] also investigated the line-to-line coupling. The results are shown in Figure 2.26.

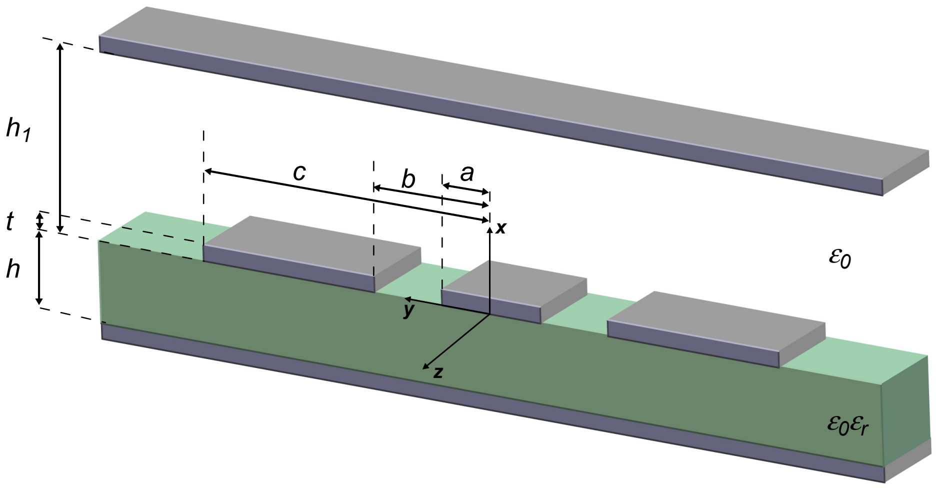

Figure 2.24: Cross section of a conductor-backed coplanar wave guide with a top metal cover. Dimensions are chosen as in reference [27]. The relatios to the dimensions of Figure 2.21 are $a = S/2$, $b = (S + 2W)/2$ and $c = (S + 2W + 2G)/2$.

a

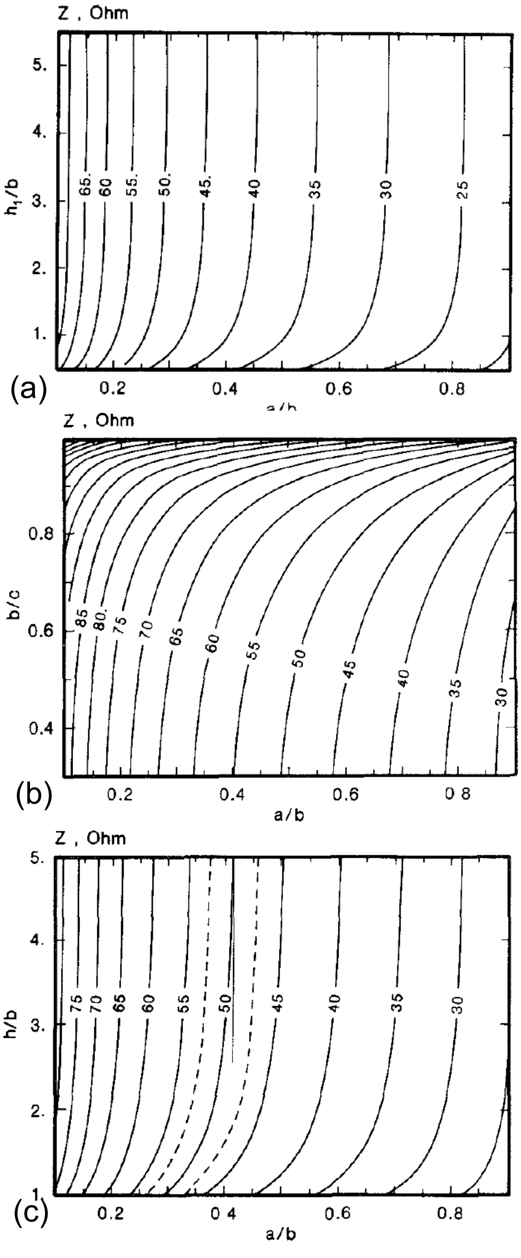

Figure 2.25: (a) Constant-impedance curves for a conductor-backed coplanar waveguide with upper shielding as a function of the shape ratio a/b and the cover height h_1/b with substrate thickness $h/b = 1$. (b) Constant-impedance curves for a coplanar waveguide with finite ground planes as a function of the shape ratio a/b and the inverse of the ground plane width b/c with substrate thickness $h/b = 1$. (c) Constant-impedance curves for a conductor-backed coplanar waveguide without upper shielding as a function of the shape ratio a/b and the substrate thickness h/b. The substrate permittivity in all the cases is $\varepsilon_r = 13$ and the thickness of the metallization is assumed to be zero. From reference [27].

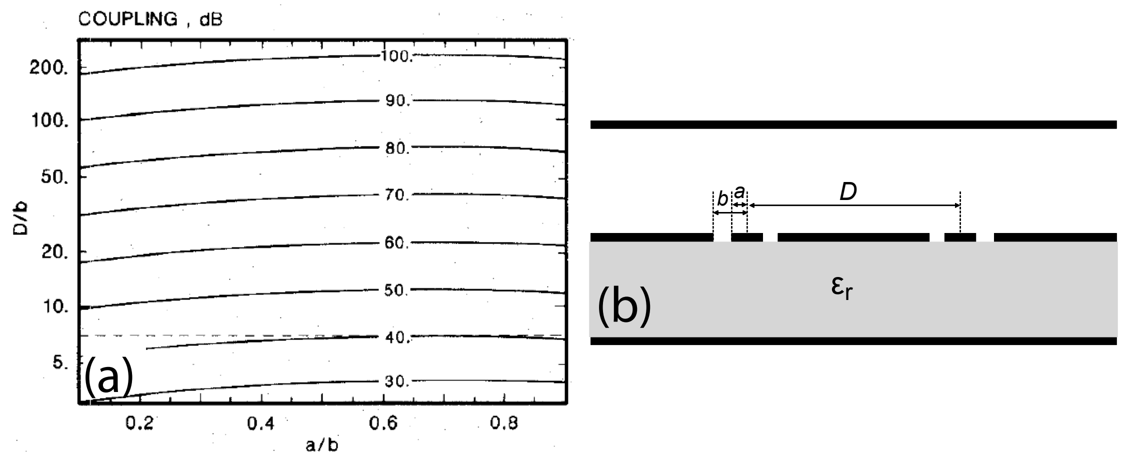

Figure 2.26: (a) Constant-coupling curves for parallel coplanar lines on infinitely thick substrate without top metal cover as a function of the shape ratio a/b and the normalized distance D/b. The dimensions are shown in (b) ($\varepsilon_r = 13, t = 0$). A maximum coupling of 40 dB would require a line spacing of at least $D/b = 7$. For $D/b = 5$, the coupling is about 35 dB. From reference [27].

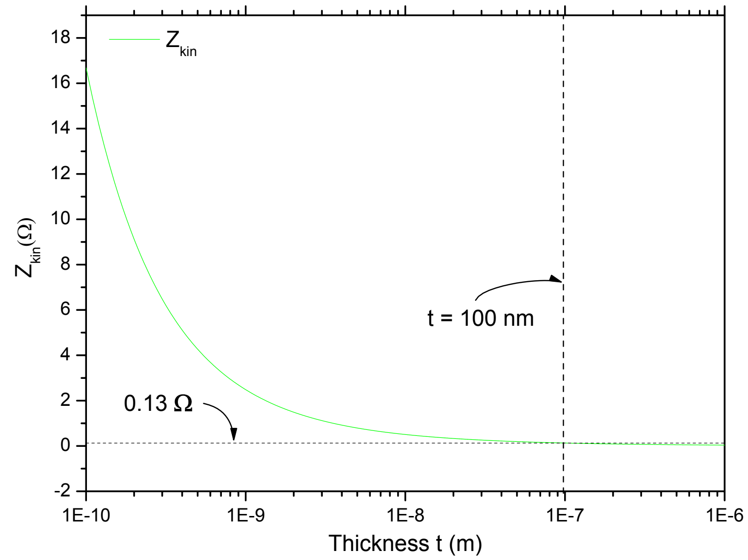

(a) Z_{kin} as a function of the metallization thickness t. For thicknesses larger than 10 nm, Z_{kin} is $\approx 0.13\ \Omega$, which is negligible in comparison to $Z_{ext} \approx 50\ \Omega$.

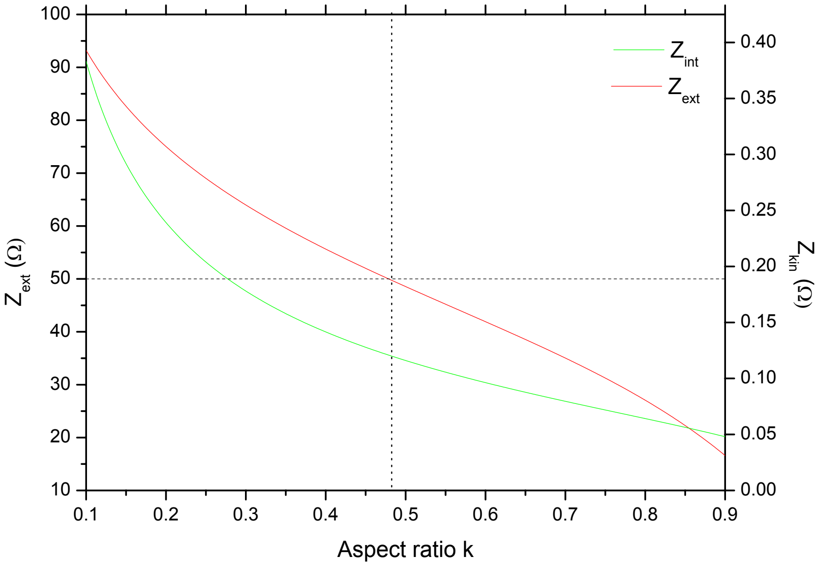

(b) Z_{kin} and Z_{ext} as a function of the aspect ratio k. For Z_{ext} to be approximately 50 Ω, the aspect ratio should be approximately 0.5. Z_{ext} strongly depends on the aspect ratio at can be set to almost arbitrary values by choosing appropriate k.

Figure 2.27: Kinetic and external impedance (Z_{kin} and Z_{ext}) as a function of different CWG parameters. If not varied, the parameters chosen for the plots are: T = 4.2 K, S = 200 μm, W = 125 μm, H = 500 μm. The material constants for Nb entering the numerical calculations can be found in Table 2.1.

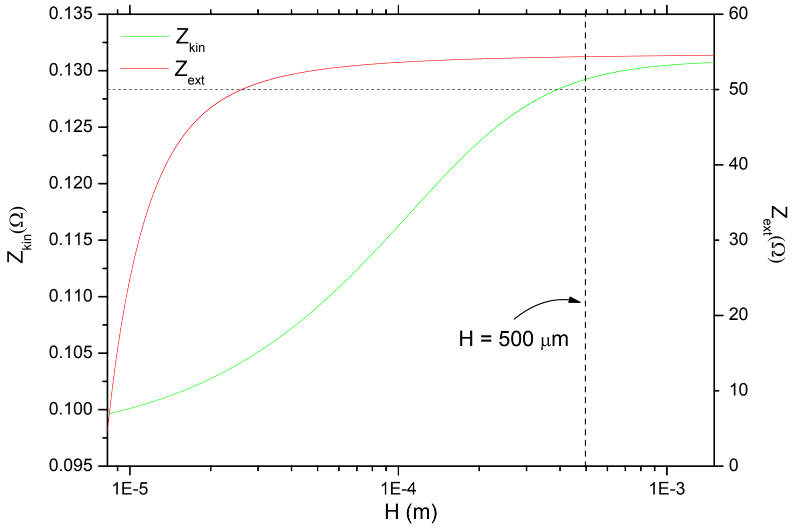

(a) Z_{kin} and Z_{ext} as a function of the substrate height H. For H larger than 100 μm, Z_{ext} is almost independent from H, where Z_{kin} reaches its asymptote at approximately 0.13 Ω for $H > 1$ mm.

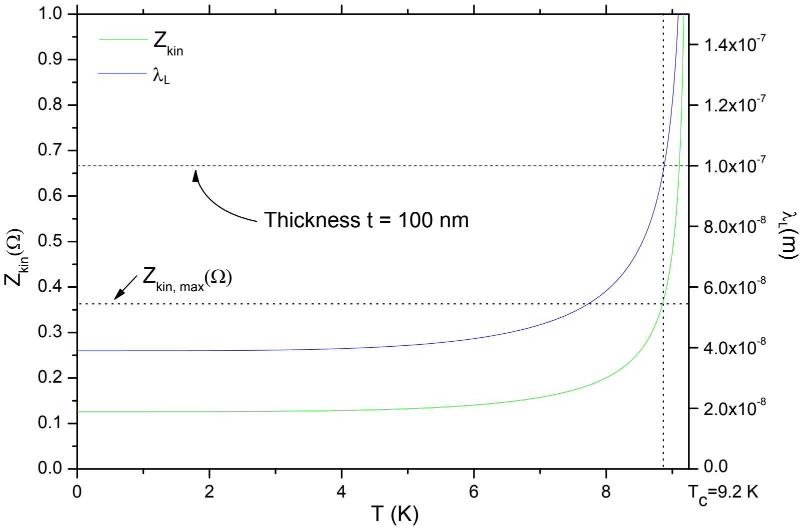

(b) Z_{kin} and λ_L as a function of temperature T. The dashed line shows the metalization thickness t. Z_{kin} and λ_L are constant unless T approaches T_c. Theoretically, for $T \rightarrow T_c$, Z_{kin} and $\lambda_L \rightarrow \infty$. Practically however, Z_{kin} is restricted to approximately 0.4 Ω because λ_L is restricted to approximately the thickness t of the metalization layer. Theory is not applicable for $\lambda_L \gg t$.

Figure 2.28: Kinetic and external impedance (Z_{kin} and Z_{ext}) and London penetration depth λ_L as a function of different CWG parameters. If not varied, the parameters chosen for the plots are: $T = 4.2$ K, $S = 200$ μm, $W = 125$ μm, $H = 500$ μm. The material constants for Nb entering the numerical calculations can be found in Table 2.1.

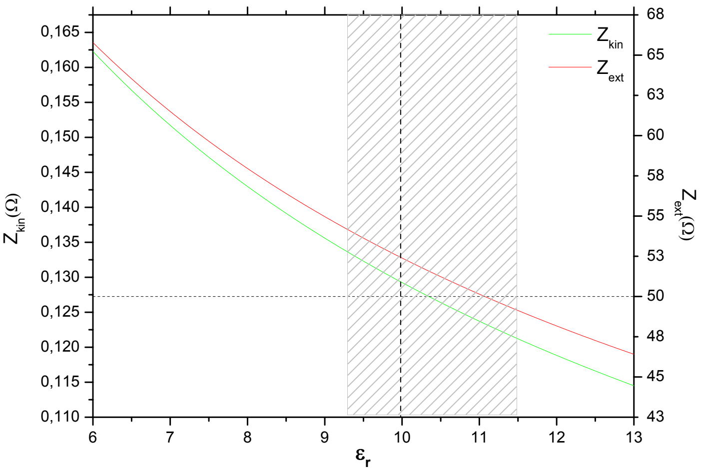

Figure 2.29: Z_{kin} and Z_{ext} as a function of the dielectric constant ε_r of the substrate. Z_{kin} and Z_{ext} crucially depend on ε_r. As ε_r depends also on temperature and frequency, this strong dependence is unfavourable for the design of matched circuits unless ε_r at its temperature dependence is well known. The gray area represents the span of literature values given for ε_r of sapphire Al_2O_3. This span also results in the anisotropy of ε_r of sapphire, resulting in an diagonal ε_r-matrix with $\varepsilon_{r,x} = \varepsilon_{r,y} \approx 9.3$ (a,b-axis) and $\varepsilon_{r,z} = 11.5$ (c-axis) [41]. $\varepsilon_r \approx 10$ is a kind of mean value for different literature values and assuming sapphire is isotropic.

2.5 Attenuation Constant α for Superconducting Coplanar Waveguides

The attenuation constant α of a CWG consists of several contributions ([12], p. 414):

$$\alpha = \alpha_c + \alpha_d + \alpha_{rl} + \alpha_{sl} \tag{2.158}$$

where

$$\begin{aligned} &\alpha_c && \text{is due to losses in the conductor,} \qquad (2.159)\\ &\alpha_d && \text{is due to losses in the dielectric,}\\ &\alpha_{rl} && \text{is due to radiation losses, and}\\ &\alpha_{sl} && \text{is due to scattering losses.} \end{aligned}$$

In this section, formulas for α_c and α_d will be given as α_{rl} and α_{sl} can be neglected in the frequency regime below 10 GHz of interest for this thesis [12, 26].

2.5.1 Attenuation α_c due to losses in the conductor

The attenuation constant α_c for superconducting CWGs as shown in (2.20) has been investigated among others by E. F. Kuester, C. L. Holloway and J. C. Booth [42, 43]. There, an expression for the attenuation constant is given which is valid for arbitrary conductor thickness. This expression takes into account losses occurring in the center strip conductor and in the two ground planes which are assumed to be extended to infinity. This means that it is strictly valid only for conventional CWGs. Under the restrictions given in section 2.4.2, these formulas can also be applied to conductor-backed CWGs. They are in any case a good approximation for the CWGs fabricated within this work.
The expression for the attenuation constant given in references [42, 43] is:

$$\alpha_c \approx \frac{R_{sm} b^2}{16 Z_0 [K^2(a/b)](b^2 - a^2)} \left(\frac{1}{a} \ln\left(\frac{2a(b-a)}{\Delta(b+a)} \right) + \frac{1}{b} \ln\left(\frac{2b(b-a)}{\Delta(b+a)} \right) \right) \quad \text{(neper/meter)}, \tag{2.160}$$

where a and b are definded according to Figure 2.24 and $K(a/b)$ is the complete elliptic integral of the first kind. Z_0 is the characteristic impedance of the CWG and R_{sm} is a modified surface impedance for a superconducting sheet of thickness t, which is given by:

$$R_{sm} = \mu_0 \omega t \Im \left(\frac{\cot(k_c t) + \csc(k_c t)}{k_c t} \right). \tag{2.161}$$

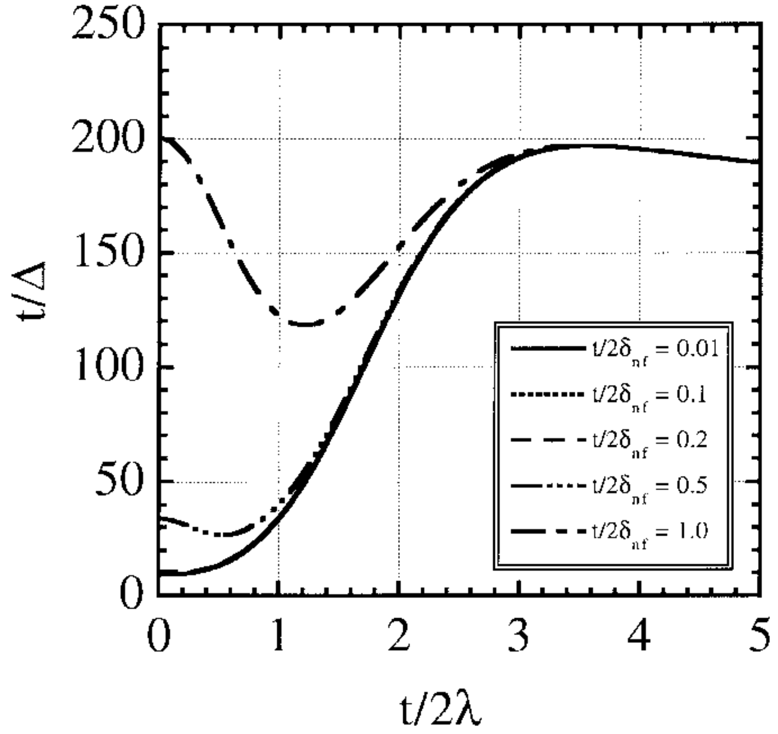

Figure 2.30: Calculated values for the normalized inverse stopping distance t/Δ as a function of $t/2\lambda_L$ and the ratio $t/2\delta_s$ as a parameter ($\theta = 90°$). From reference [42].

k_c is the complex wavenumber in a superconductor

$$k_c^2 = (1/\lambda_L)^2 + 2j(1/\delta_s)^2, \tag{2.162}$$

whereas λ_L is the London penetration depth and δ_s is the skindepth.
In the expression for α_c the *stopping distance* Δ is entering, which is a function of the edge profile θ (in this work $\theta = 90°$ is assumed, since θ of the real structures is not known and Δ is not changing much by varying θ), the metalization thickness t and the material properties of the metalization. The latter enter the theory through the complex conductivity (2.56) which can be finally expressed by the London penetration depth λ_L (2.54) and the skin depth δ_s (2.28) according to (2.64). Δ is a numerical value. A table of numerically calculated values for Δ as a function of the normalized thickness $t/2\lambda_L$ and the ratio $t/2\delta_s$ as a parameter is presented in reference [19], p. 232. These values are graphically given Figure in 2.30. As the stopping distance is sensitive to the ratio $t/2\lambda_L$ but insensitive to small values of $t/2\delta_s$, one can assume $t/2\delta_s \approx 0$ (for Nb at 4.2 K the ratio is 0.077 according to the values given in Table 2.1). For niobium at 4.2 K and for a Frequency of 3 GHz, the ratio is approximately 0.05 (see Figure 2.5).
Evaluating this expression for a CWG made from Nb (see Table 2.1) at 10 GHz and 4.2

K with the dimensions given in Figures 2.28 leads to an attenuation constant due to the conductor $\alpha_c \approx 1.9 \cdot 10^{-3}$ np/m $\approx 1.6 \cdot 10^{-2}$ dB/m[4]. For a structure of length 4 cm, this gives an attenuation of $6.4 \cdot 10^{-4}$ dB. The ratio of the propagation constant β and twice the attenuation 2α defines the Q-factor of the transmission line:

$$Q = \frac{\beta}{2\alpha} = \frac{\beta\,[1/\mathrm{m}]}{2\alpha\,[1/\mathrm{m}]} = \frac{\beta\,[1/\mathrm{m}]}{2\alpha[\mathrm{dB/m}]} \cdot 8.686\,[\mathrm{dB/neper}]. \tag{2.163}$$

The Q-factor is temperature and frequency dependent. Its temperature dependence for a structure with dimensions given above is plotted in Figure 2.31 for 10 GHz.

For temperatures below 2.5 K, Q $> 10^6$. This is very high, allowing to design superconducting coplanar resonators with very high quality factors up to 10^6 [44]. This is important to reach the strong coupling regime in circuit QED between the resonator and a Qubit positioned inside the resonator [28]. Measuring the transmission parameter $|S_{12}|$ of such a resonator allows to determine β and α in an accurate way. Measuring the attenuation directly by measuring the transmission parameter of a transmission line of reasonable length is hardly possible. It is surely impossible with the measurement scheme used in this work as one will see in Chapter 5.

Figure 2.31 shows Q as a function of frequency f at 4.2 K. The attenuation α_c increases faster with increasing frequency than β which results in a decreasing Q with increasing f.

2.5.2 Attenuation α_d due to losses in the dielectric

An expression can also be given for the attenuation constant α_d in the dielectric as shown in [3]:

$$\alpha_d = \frac{\pi}{\lambda_0} \frac{\varepsilon_{\mathrm{eff}} - 1}{\sqrt{\varepsilon_{\mathrm{eff}}}} \tan\delta_e \qquad \text{(neper/meter)}. \tag{2.164}$$

λ_0 is the free space wave length. δ_e is the dielectric loss tangent of the substrate.

This expression is strictly valid only for a conventional CWG (meaning infinite ground planes, zero metalization thickness, finite substrate thickness, no conductor backing). As one is now interested in power dissipation and thus fields *outside* the conductor, the zero metalization thickness is a good approximation. The assumption of infinite ground planes and finite substrate thickness is valid under the circumstances given in section 2.4.2. To take into account the effect of the conductor backing, the expression in reference [3] is modified by taking the effective dielectric constant $\varepsilon_{\mathrm{eff}}$ as defined in (2.4.2) for conductor backed CWGs.

The dielectric loss tangent δ_e of sapphire at 21.3 GHz [45] is shown in Figure 2.32. As losses increase with increasing frequency, the values given there can be taken as an upper worst case limit for the frequencies of interest within this thesis. It can be seen that the loss tangent is already lower than $5 \cdot 10^{-8}$ at 20 K. Assuming realistic values for CWG

---

[4] 1 neper = 8.686 dB

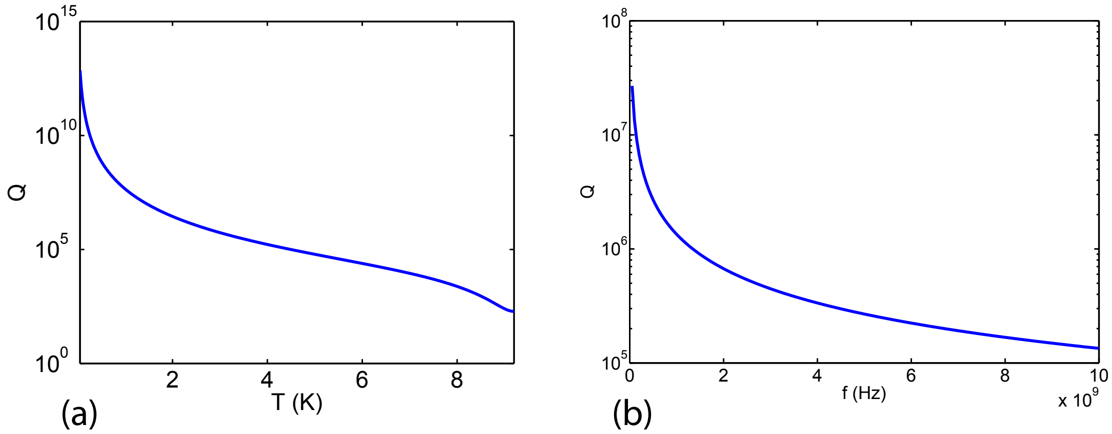

Figure 2.31: Temperature and frequency dependence of the Q-factor of a CWG taking into account only conductor losses α_c. (a) Q-factor as a function of temperature T at 10 GHz. (b) Q-factor as a function of frequency f at 4.2 K.

made from Nb structures in analogy to the one taken for Figures 2.28, one ends up with the following parameters for a frequency of 10 GHz and temperatures below 20 K: $\lambda_0 = 3.0$ cm, $\varepsilon_{\text{eff}} = 5.6$. This results in a dielectric attenuation constant[5] of $\alpha_d = 1.0 \cdot 10^{-5}$ np/m $\approx 8.7 \cdot 10^{-5}$ dB/m . For a structure of length 4 cm, this gives an attenuation of $3.5 \cdot 10^{-6}$ dB. This is negligible in comparison to α_c at 10 GHz and 4.2 K. The corresponding Q-factor is $Q = \beta/2\alpha = 2.5 \cdot 10^7$. Apart from the very low dielectric losses of sapphire, the substrate is very well suited also for cryogenic purposes as it has a very good heat conductivity at low temperatures. Because of these two reasons, the CWG structures within this work were fabricated on sapphire substrates.

2.6 Dispersion in Superconducting Coplanar Waveguides

For using the hybrid ring and CWG circuitry in conjunction with single microwave photons, the dispersion of CWGs gets an important issue to investigate, as the dispersion will set a limit for the minimal pulse length τ_{min} [s] of a signal that can be transmitted with negligible pulse broadening.

---

[5] 1 neper = 8.686 dB

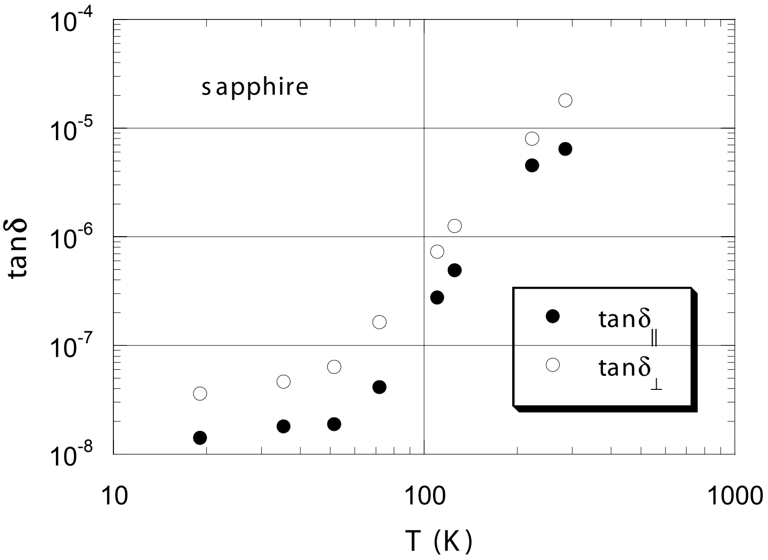

Figure 2.32: Dielectric loss tangent $\tan\delta_e$ of sapphire at 21.3 GHz parallel and perpendicular to the c-axis [45].

To get the dispersion relation $\omega(\beta)$ of a CWG, quasi-static approximations cannot be used, as they are based in principle on the assumption of negligible dispersion.
According to equation **??**, the dispersion relation is originated in a frequency dependent ε_{eff}. In literature, an expression for the dispersion seems to exist only for a conventional CWG [46], see Figure 2.20. This expression will be given here. It is further assumed that the metalization thickness is zero and the conductor is lossless. The expression was deduced by fitting the dispersion data obtained using the spectral domain method. The expression is valid upto the THz-regime. For conductor backed CWGs one has to use spectral domain methods explicitly as done e.g. in references [47,48]. The expression is:

$$\sqrt{\varepsilon_{\text{eff}}(f)} = \sqrt{\varepsilon_{\text{eff,TEM}}} + \frac{\sqrt{\varepsilon_r} - \sqrt{\varepsilon_{\text{eff,TEM}}}}{1 + aF^{-b}} \tag{2.165}$$

$$\begin{aligned} \text{where} \qquad & \qquad (2.166) \\ q &= \ln(S/H) \\ u &\approx 0.54 - 0.64q + 0.015q^2 \\ v &\approx 0.43 - 0.86q + 0.540q^2 \\ \ln(a) &\approx u\ln(S/W) + v \\ b &\approx 1.8 \end{aligned}$$

ε_r is the relative dielectric constant of the substrate and $\varepsilon_{\text{eff,TEM}}$ is the effective dielectric constant used for the quasi-static limit where a quasi-static TEM wave propagation is assumed on the CWG. The constants are numerical values from fitting the experimental data.

$F = f/f_{TE}$ is the normalized frequency, where

$$f_{TE} = c/(4H\sqrt{\varepsilon_r - 1}) \tag{2.167}$$

is the cutoff frequency for the lowest-order slotline TE mode of the CWG, that is a wave that is able to propagate *only* in between *one* gap of the CWG. This frequency can be seen as the upper limit of the usable frequency band. By reducing H, this frequency may be increased. The formula is accurate to within 5% for the parameter range:

$$\begin{aligned} 0.1 < S/W < 5 \\ 0.1 < S/H < 5 \\ 1.5 < \varepsilon_r < 50 \\ 0 < f/f_{TE} < 10 \end{aligned} \tag{2.168}$$

The dimensions of the structures fabricated within this thesis are in this range.
The bandwidth definition in reference [49] relates the full width half maximum (FWHM) τ of a pulse with Gaussian shape to the frequency $f_{0.1}$ at which the spectral amplitude is 10% of the peak value:

$$f_{0.1} = \frac{2\sqrt{\ln 2 \cdot \ln 10}}{\pi\tau} \approx 0.8 \cdot 1/\tau. \tag{2.169}$$

Therefore, the bandwidth is indirect proportional to the pulse duration.
Taking f_{TE} as the maximum bandwidth, gives a minimum pulse duration for a CWG with dimensions given in 2.28 as $\tau_{min} = 0.8 \cdot 1/f_{TE} \approx 0.8 \cdot 1/50\,\text{GHz} = 16\,\text{ps}$. This is short enough for experiments in circuit QED. Typical energy relaxation times (T_1) of superconducting Qubits are presently in the microsecond regime [50]. Most probably, it is the surrounding circuitry that limits the bandwidth.
A very illuminating experimental and theoretical investigation of the attenuation and the dispersion is given in reference [48]. There, a high-T_c superconducting CWG with dimensions comparable to the one fabricated in this thesis is compared to a CWG of same dimensions with gold metalization. The theory presented there only involves the complex conductivity (2.56) and the London penetration (2.54) depth as parameters of the superconducting material and can thus also be used for conventional superconductors. Moreover, non-zero metalization thickness is assumed there. Theory and experiment are in good agreement and confirm the huge decrease of attenuation and dispersion due to the superconducting properties of the material. The results should be even better for a conventional superpconductor like Nb, where the London penetration depth is smaller which yielding an even stronger reduction of the surface resistance (**??**).

2.7 Design procedure

With the tools developed so far, it is now easy to design a hybrid ring without the use of time consuming numerical simulations. The design procedure is as follows:

1. The characteristic impedances of the CWG ring and the CWG arms should have a ratio given by 2.140 which results from transmission line theory. Normally, one chooses the impedance of the arms to be 50 Ω to fit the impedance of the surrounding circuitry.
2. The dimensions of the CWG sections have to be designed according to the expressions in section 2.4.2 with respect to the substrate height and ε_r. The transversal CWG structure dimensions should be chosen small enough to prevent dispersion (see 2.167). The metalization thickness should be at least equal to the London penetration depth (see Figure 2.27(a)). This makes the characteristic impedance insensitive to thickness variations and facilitates fabrication.
3. (**??**) allows to calculate β_0 for the frequency f_0 where the isolation $|S_{13}|$ of the hybrid ring should be maximum. From β_0, the ring radius is calculated: $R = 3/(2\beta_0)$.
4. Losses can be introduced in the design formulas concerning to the low loss approximation from section 2.2.6.2 by the substitution: $\beta \rightarrow \beta - i\alpha$.
5. If α and ε_r are not known (this is often the case, especially at low temperatures), these have to be be used as fit parameters to the measurement data.

The parameters of the hybrid rings fabricated during this work can be found in Table 5.1.

Chapter 3

Numerical Simulations

3.1 Introduction

In this work, the hybrid ring was also analysed using commercially available software. The programs that have been used for this approach are:

- Microwave Office 2002© [51] (MWO), and
- CST Microwave Studio© [52] (MWS)

Both programs are integrated design and analysis tools for RF, microwave, and millimeter-wave design. In this section, the results of the simulations will be presented and - if possible - compared to the results of transmission line theory (TLT). More profound information on each of the programs may be found in the corresponding user manuals.

3.2 CST Microwave Studio

MWS is a general-purpose electromagnetic simulator based on the Finite Integration Technique (FIT), first proposed by Weiland in 1976/1977 [53]. This numerical method provides a universal spatial discretization scheme, applicable to various electromagnetic problems, ranging from static field calculations to high frequency applications in time or frequency domain. FIT discretizes the integral form of Maxwells equations, rather than the differential one.

In order to solve these equations numerically a finite spatial calculation domain is defined, enclosing the considered application problem. By creating a suitable mesh system, this domain is split into a large number of small cuboids, so-called grid cells. This mesh can be visualized in MWS as shown for example in Figure 3.1(a). The spatial discretization of Maxwells equations is finally performed on this grid.

This essential point of FIT discretization is reflected in the fact that important properties of the continuous gradient, curl and divergence operators are still maintained in grid space. It can than be shown that the FIT formulation is maintaining energy and charge conservation [54].

Finally, missing material equations (2.10,2.11,2.45) introduce an inevitable numerical inaccuracy due to the spatial discretization. By defining the necessary relations between voltages and fluxes in the material equations, the integral values of the voltages and fluxes have to be approximated over the grid edges and cell areas, respectively. Consequently, the resulting coefficients depend on the averaged material parameters as well as on the spatial resolution of the grid.

Three different types of solving algorithms are available for high frequency electromagnetic field problems: transient, frequency domain and eigenmode solver.

For the simulation of the hybrid ring, only the transient solver was used as the transient solver is recommended for most driven problems (i.e. with nonzero sources), especially for devices with open boundaries or large dimensions. With the transient solver, the simulation of a structure's behavior in a wide frequency range is possible in a single computation run.

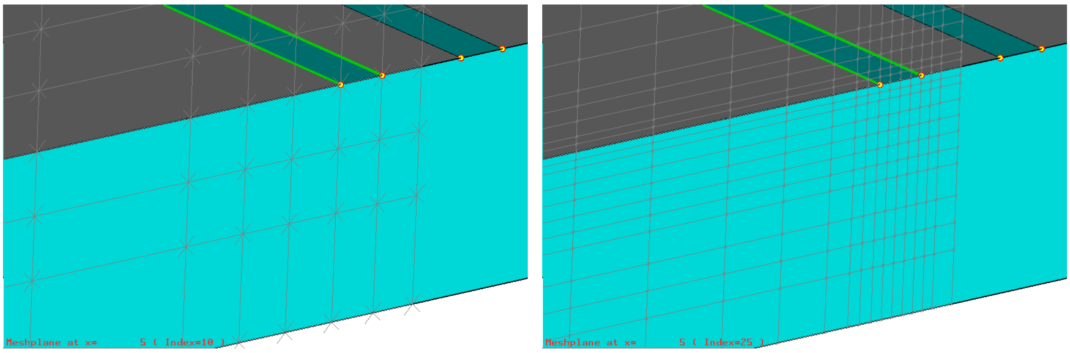

(a) (b)

Figure 3.1: (a) A very coarse grid and (b) are very fine grid, discretizing a simulation volume which contains a CWG on a substrate.

It solves the problem in time domain. The transient solver is based on the solution of the (space) discretized set of Maxwell equations, in which the time derivatives are substituted by central differences.

Every method which tries to describe a real world problem using a numerical model implies the danger of introducing errors, either because the model does not describe the actual device accurately enough, or because the numerical simulation is subject to errors. In the following, the most important error sources will be shortly described [52]. Many of them may be negligible in practice, but one should always be aware of them in order to make sure one can rely on the results:

1. **Simulation Model is not in Agreement with Reality**
   - *Geometric dimensions* are wrong or geometric details have been neglected.
   - *Material parameters* are wrong, either because they are unknown and had to be chosen arbitrarily, or because a value was chosen which is valid for another frequency band but not for the band of interest.
   - The *source of excitation* was not chosen correctly, e.g. a perfectly matched microstrip port instead of a coax fed microstrip. Furthermore, for open ports such as microstrips or coplanar lines, the port size should be chosen to be sufficiently large in order to correctly capture the field pattern of the propagating modes which are calculated in a quasi-static approximation in the corresponding 2-dimensional port plane. The same considerations are valid for *output ports*.
   - Sometimes the *environment* is not considered correctly. Objects that are placed near the measured structure may influence the result and in this case should be included in the simulation model.
2. **Inaccuracies due to the Simulation**

- *Discretization error*: To ensure accurate results the electromagnetic fields have to be sampled with sufficient in spatial resolution. Generally, the accuracy of the field solution increases with decreasing mesh size and it can be proven that convergence is ensured by the FIT. MWS supports convergence studies by automatic adaption of the mesh density parameters (so-called adaptive mesh refinement) and by visualization of the convergence progress, as will be shown below.
- *Truncation error*: If the calculation is stopped before the time-domain signals have decayed to zero, a so-called truncation error is introduced.
- The *geometry error* is the deviation between the initially defined CAD structure and the simulation model. If an object becomes small compared to the size of the mesh cells, the geometry error will be large.
- Some inaccuracy may be introduced through *boundary conditions*. In the case of radiating structures, the open space is simulated by so-called open boundaries. Here, the perfectly matched layer (PML) technique is used
- Even if the field values are calculated correctly, *interpolation errors* may still occur, e.g. when deriving secondary field quantities or when calculating the field values at locations other than the grid edges.
- *Numerical errors* finally may be caused by the finite representation of numbers, but can typically be neglected for the explicit algorithm in time-domain.

If one ensures that one has taken sufficiently into account these possible errors, one can be confident in the simulation results.

To get an idea of the simulation procedure with an electromagnetic simulator, it is recommended to start with a simple structure. This will be briefly presented here to show the limitations of the transient solver in simulating a structure like the hybrid ring.

The simulations were performed on a PC with a 2 GHz CPU and 4 GB RAM. As an enclosure of the simulation volume, perfectly electrical conducting (PEC) walls were chosen.

In Figure 3.1(a), a coarse grid of a 5 mm long section of a CWG transmission line is shown. It has the dimensions: center strip width $W = 200\,\mu$m, gap width $G = 105\,\mu$m and substrate height $H = 500\,\mu$m. The dielectric constant of the dielectric is set to 10. When simulating such a structure with the adaptive mesh refinement activated the simulator refines the mesh until a certain convergence criterion is reached. The convergence criterion is set by defining the maximum deviation of the absolute value of the complex difference of the S-parameters between two subsequent passes. The S-parameters resulting from such a simulation are shown in Figures 3.2(a) and 3.2(b).

As one can see, the S-parameters have converged after the second iteration step. The same is true for the line impedance, which is as the numerical equivalent to the characteristic impedance of a transmission line. It can be calculated by

$$Z = \frac{P}{(\sum_n I_{in})^2}, \tag{3.1}$$

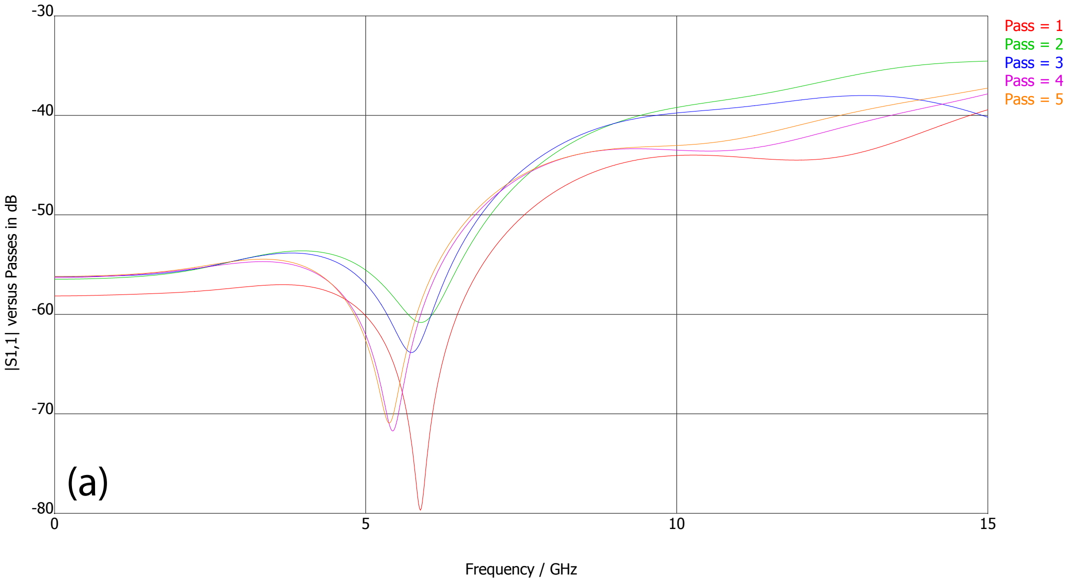

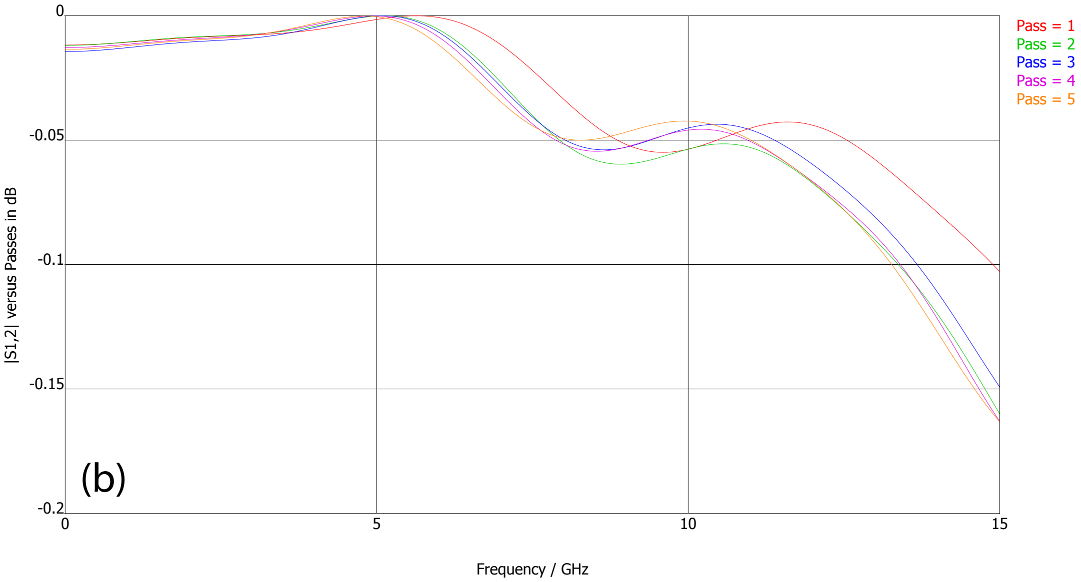

Figure 3.2: (a) S_{11}- and (b) S_{12}-parameters of a 5 mm long CWG section for different mesh refinements (Pass 1: coarse grid → Pass 5: fine grid).

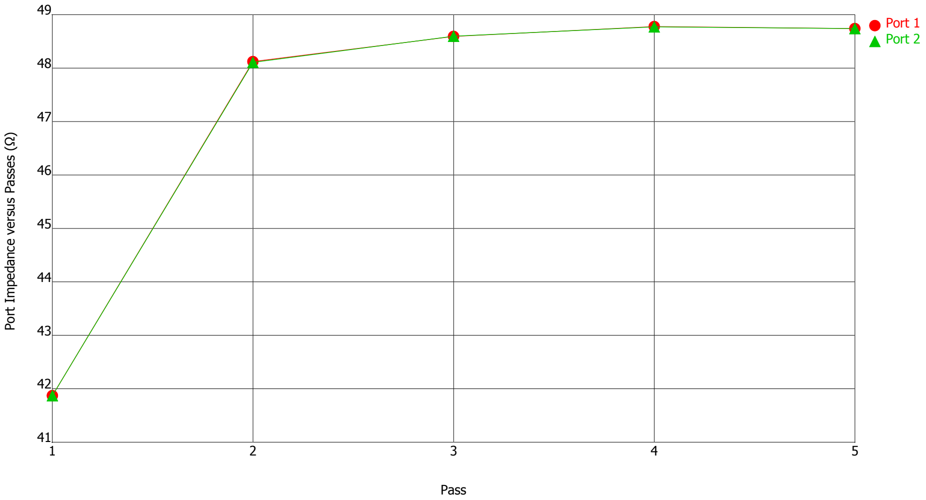

Figure 3.3: The convergence of the characteristic impedance of a 5 mm long CWG section calculated in the cross section of the ports.

where P is the power given as the integral of the poynting vector over the port area and the currents are calculated by integrating the magnetic field in a small distance around all present conductor surfaces. The calculated impedance differs slightly from values given by the quasi-static expression. This may result from the definition of the line impedance that differs from the commonly used expression $Z = U/I$.

The number of meshcells in pass one is around 1760, whereas in the finest grind there are approximately $30^3 = 20{,}000$ gridcells. The minimum size of the gridcell here is 0.016 mm. The solver time in pass 1 is 5 seconds whereas in pass 6, the solver time is 50 seconds. The simulator used approximately 9200 timesteps with a timestep of $5.11 \cdot 10^{-5}$ns.

For a prolongated CWG transmission line of 30 mm length (note that the dimensions of the hybrid ring on the substrates are 20.4 × 15 mm), the S-parameters are shown in Figures 3.4(a) and 3.4(b). Here, the convergence is much slower. Moreover, the S-parameters show wiggles at low frequencies. The transmission is very good, although the unsteady devolution of the curve is completely unexpected as dispersion-free and loss-less materials have been used to create the structure. Figure 3.5 shows the magnetic field vectors along the CWG supporting a quasi-TEM mode with a frequency of 7.5 GHz.

The port impedances also converge more slowly than in Figure 3.6. The solver time in the fifth pass is already 500 seconds, the number of meshcells is 25000. The simulator used approximately 37531 timesteps with a timestep of $1.26 \cdot 10^{-4}$ns. This means that the solver chooses a coarser grid, even though the same convergence criterion was applied. The minimum meshcell is now 0.05 mm. All in all, a linear spatial enlargement by a factor of 6 leads to an increase in solvertime by a factor of ten.

If one transfers these preliminary considerations to the simulation of the hybrid ring, one can imagine that a simple mesh refinement can easily lead to very high calculation times. By a simple estimation, one can see, that very elaborate *adaptive* mesh refinement strategies

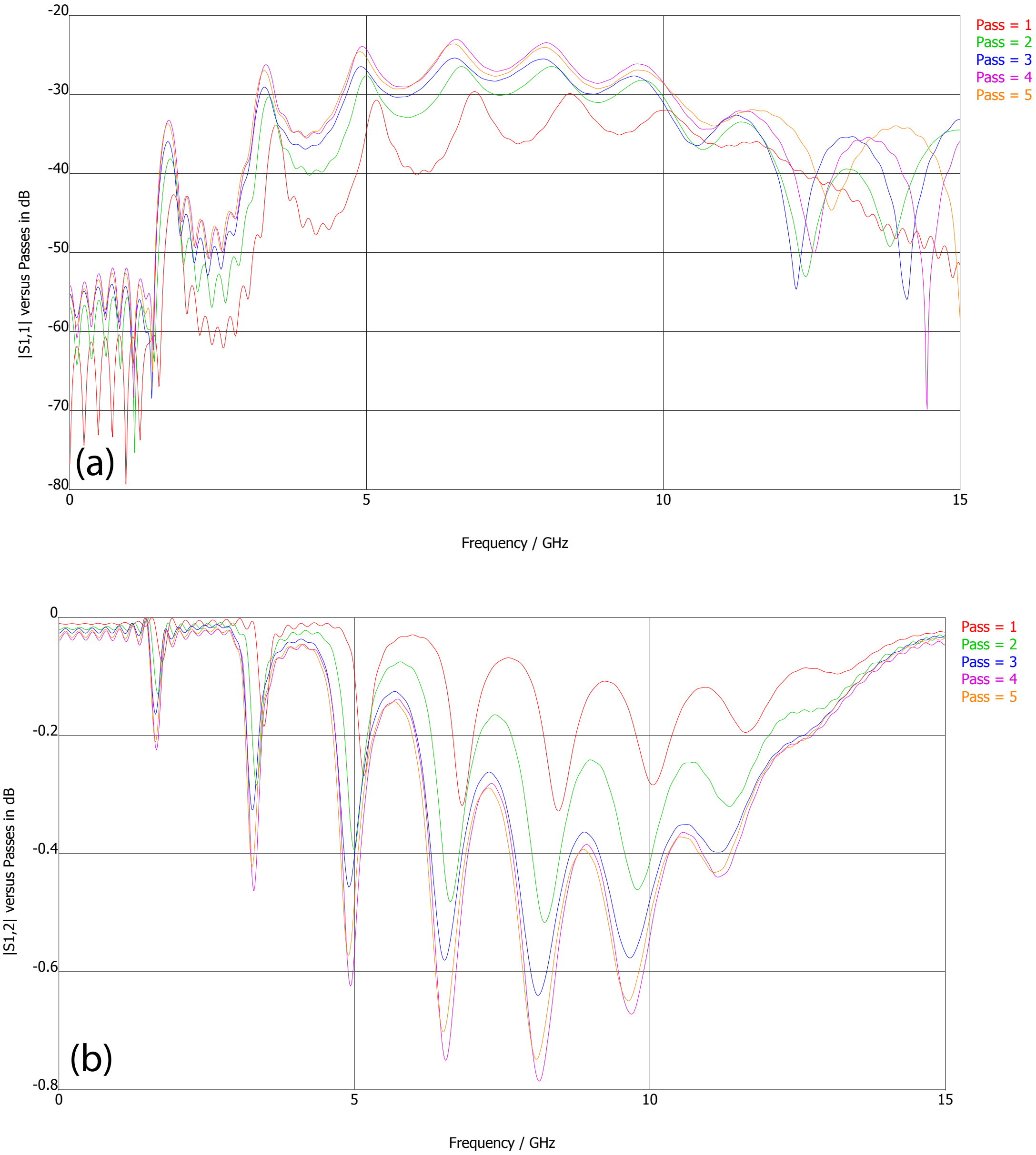

Figure 3.4: (a) S_{11}- and (b) S_{12}-parameters of a 30 mm long CWG section for different mesh refinements (Pass 1: coarse grid → Pass 5: fine grid).

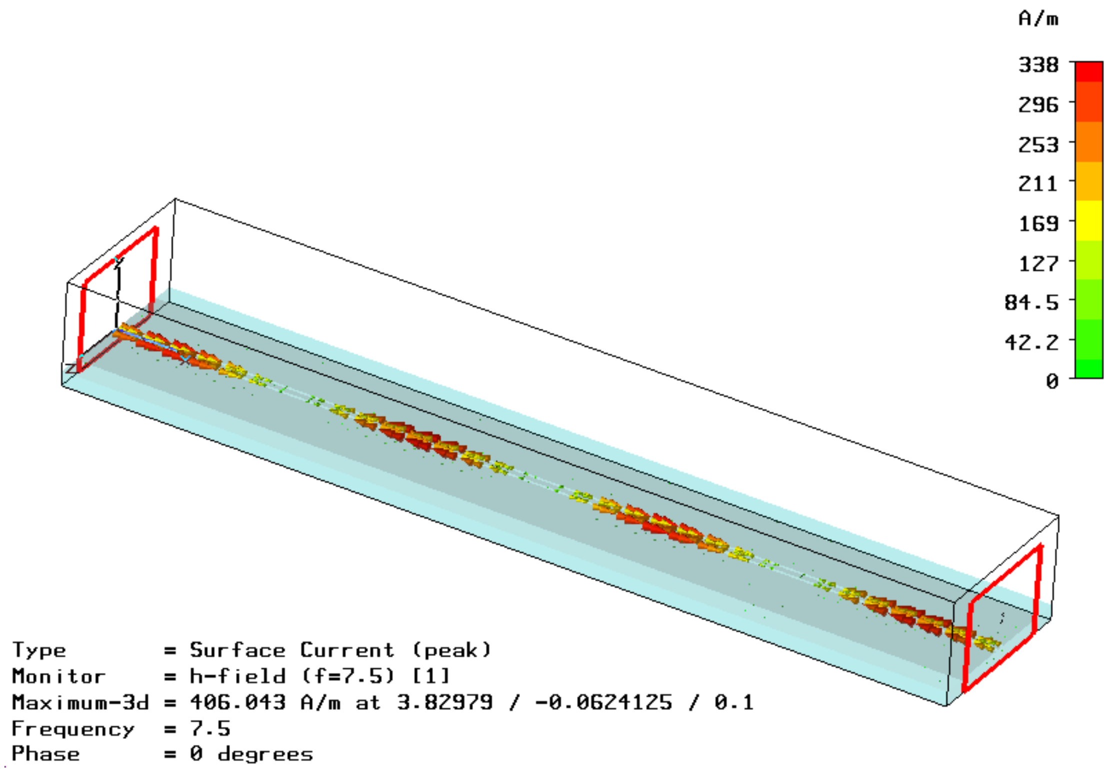

```
Type         = Surface Current (peak)
Monitor      = h-field (f=7.5) [1]
Maximum-3d   = 406.043 A/m at 3.82979 / -0.0624125 / 0.1
Frequency    = 7.5
Phase        = 0 degrees
```

Figure 3.5: A 30 mm long section of a CWG transmission line supporting a quasi-TEM mode with a frequency of 7.5 GHz. The arrows are the magnetic field vectors along the line.

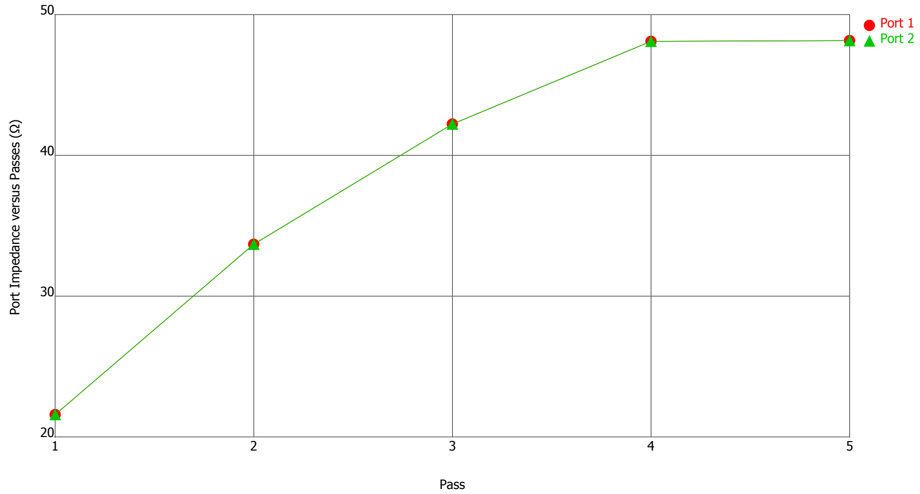

Figure 3.6: The convergence of the characteristic impedance of a 30 mm long CWG section calculated in the cross section of the ports.

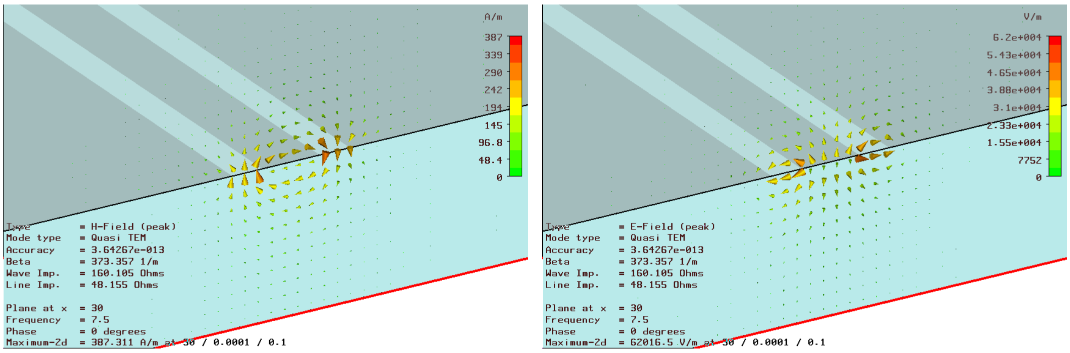

```
Type          = H-Field (peak)
Mode type     = Quasi TEM
Accuracy      = 3.64267e-013
Beta          = 373.357 1/m
Wave Imp.     = 160.105 Ohms
Line Imp.     = 48.155 Ohms

Plane at x    = 30
Frequency     = 7.5
Phase         = 0 degrees
Maximum-2d    = 387.311 A/m at 30 / 0.0001 / 0.1
```

```
Type          = E-Field (peak)
Mode type     = Quasi TEM
Accuracy      = 3.64267e-013
Beta          = 373.357 1/m
Wave Imp.     = 160.105 Ohms
Line Imp.     = 48.155 Ohms

Plane at x    = 30
Frequency     = 7.5
Phase         = 0 degrees
Maximum-2d    = 62016.5 V/m at 30 / 0.0001 / 0.1
```

(a) (b)

Figure 3.7: (a) The E-field vectors and (b) the B-field vetors of a CWG transmission line.

are necessary to simulate a *complete* CWG hybrid ring and its surrounding volume:

A CWG hybrid ring posseses two different length scales. The ring radius (which is determined by the wavelength on the CWG at the working point which is approximately 2 cm for a center frequency of 7 GHz) and the transversal dimensions of the CWG transmission line sections (which were chosen to be around 100 μm). The ratio (=200) of this two length scales is large which forces the simulation to use a fine grid. Only by advanced adaptive meshing techniques, it is possible to reduce the number of gridcells from $(200)^3 = 8 \cdot 10^6$ to approximately 45.000.

Additionally, one has to take into account the maximum time step for such a simulation. It should not exceed $\Delta t = \Delta s / c = 5 \cdot 10^{-13}$ s, where $\Delta s \approx 100\,\mu$m is the minimal grid size and c (approximately $2 \cdot 10^8$ m/s) the signal velocity in the simulation volume. The signal then passes the structure within $T = 2\,\mathrm{cm/c}= 0.1$ ns, resulting in 200 timesteps. In every timestep, 45000 discretized sets of Maxwell equations have to be solved, resulting in total number of $9 \cdot 10^6$. This is too much. In fact, it was not even possible to do one single adaptive mesh refinement step to check the convergence of the simulated solution.

Apart from this very rude estimation, it is very difficult to analyze in detail the reasons, why it was not possible to simulate the CWG hybrid structure reasonably. This is due to the fact that one has no insight into the code of the program. The manual is not sufficient. Figure 3.8 shows a CAD model of the hybrid ring number H3 (see section 5.1 for dimensions, all other parameters are the same as in the examples above), as it was implemented for the simulation in MWS. Figure 3.9(a) is a promising simulation for different values of the dielectric constant ε_r. However, already a slight change of 4 μm of the initial width $W = 90\,\mu$m of the center strip conductor leads to a completely unexpected S-parameter result shown in Figure 3.9(b).

All this illuminates the reason, why this software is not recommended for the simulation of the *complete* hybrid ring at the same time with the transient solver. Nevertheless, this would be theoretically more precise, as it should also account for any kind of direct crosstalk between the different hybrid ports due to e.g. box resonances.

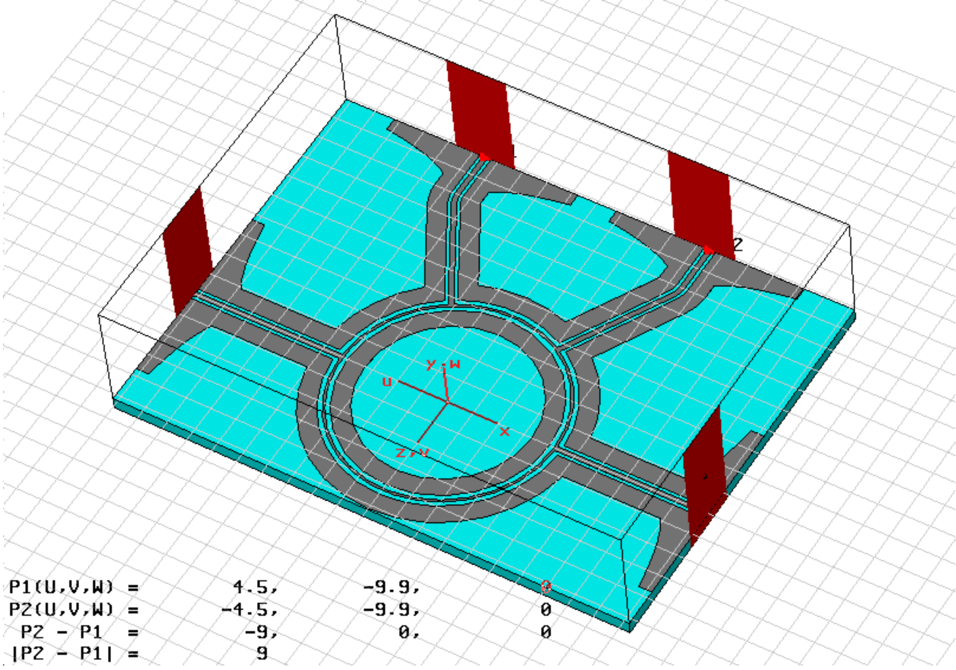

Figure 3.8: CAD model of the hybrid ring number H3 as it was implemented for the simulation in MWS.

Therefore, only two further possible problems will be stated here: 1. The round shape of the hybrid ring constitutes a principle problem for MWS as it has a rectangular grid. 2. The thin metalization layer constitutes a severe problem as a gridcell is filled completely with PEC by the MWS algorithm as soon as 2 PEC sheets intersect the gridcell.

As it seems not to be possible to achieve accurate results in a reasonable time, it is in fact advisable to use this simulation software rather for small sections of the hybrid ring, especially where one expects discontinuities in the wave propagation as constituted for example by the T-junctions or the V-connectors.

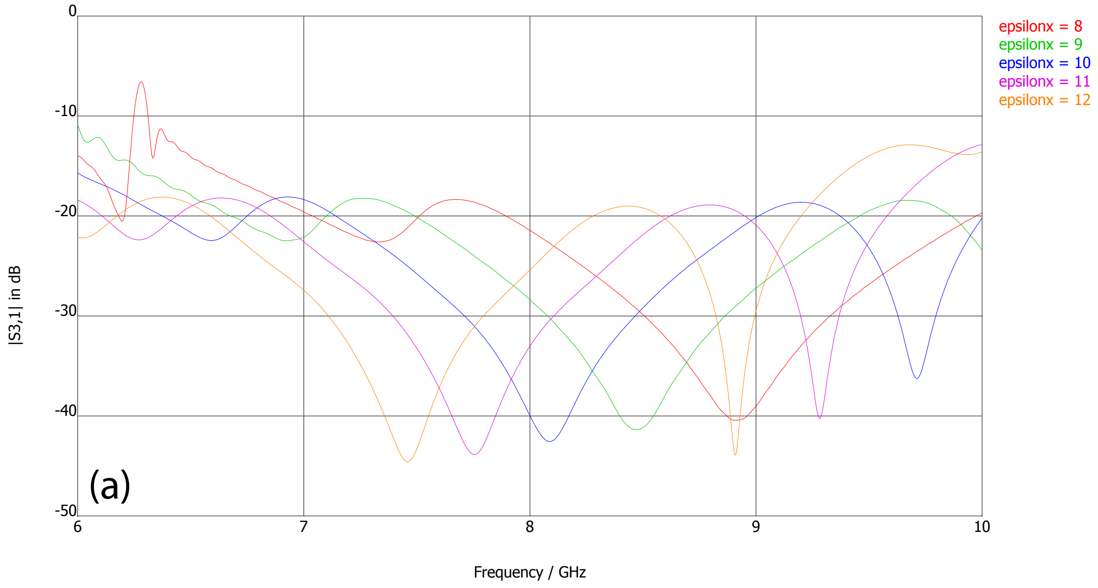

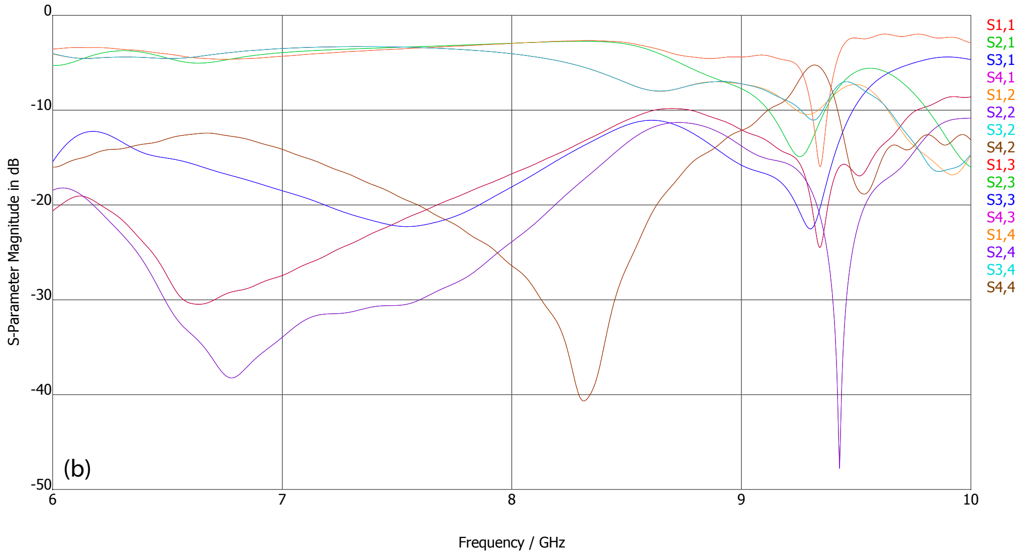

Figure 3.9: (a) S_{13}-parameter for different values of the dielectric constant of the CAD model shown in Figure 3.8. (b) S-parameters of a CAD model with a slightly changed width W of the center strip conductor in comparison to the model in Figure (a). (a) W = 90 μm 4 (b) W = 86 μm.

3.3 Microwave Office 2002

MWO allows to design circuits composed of linear and nonlinear pre-defined structures, and generate layout representations of these designs. These circuits may then be analysed, using linear, nonlinear, harmonic balance, and nonlinear Volterra-series simulation algorithms. Details about these simulation engines in particular and the use of MWO in general may be taken from the user manual of MWO. Moreover, MWO features real-time tuning and optimizing capabilities.

MWO is also equipped with a quasi-3-D electromagnetic simulation engine (called *EM Sight*). It is called a quasi-3-D electromagnetic simulator because it allows simulations only on parallel, planar, piece-wise constant stratified media which can be interconnected by electrically conducting vias. For this reason, it is well suited for the design of microwave integrated circuits (MIC) as well as monolithic microwave integrated circuit (MMIC) applications, where the different layers interact with each other *only* by vias and not - for example - field cross talk elsewhere along the lines. *EM Sight*'s method of solution for the electromagnetic problem is based on the spectral-domain method [34–37]. Nevertheless, *EMSight* was not used for the simulation of the hybrid ring as a whole, as the programming interface of *EMSight* is very inconvenient for the design of complex CWG structures like the hybrid ring. Moreover, a simulation of the whole hybrid ring with *EMSight* would be computationally too expensive.

Instead, the hybrid ring was simulated, using the *Schematic Circuit Design* module of MWO in conjunction with the *Linear Simulation Engine*.

The *Schematic Circuit Design* module allows for a very easy and intuitive linear circuit design: The process to create a linear design begins with placing linear elements in a schematic, then adding ports and sources to define the network. The elements can be data files, pre-defined structures, structures analyzed with *EMSight*, or even mathematical models of electromagnetic structures. The resulting complete schematic of the hybrid ring is shown in Figure 3.10.

The circuit elements that were used for the circuit design of the hybrid ring are shown in Figure 3.11:

- The circuit element *CPW1LINE* models a section of conductor backed CWG with metal cover. This component does not impose restrictions on the conductor thickness (thickness may be zero and non-zero). It is simulated as a quasi-static model that involves a numerical algorithm presented in reference [55].

- The circuit element *CPWTEEX* models a CWG symmetric T-junction including the effects of airbridges which connect the ground planes on each side of a discontinuity. The purpose of these features is to suppress the excitation of a slot line mode between the three ground planes (see also section 5.4.2 and reference [19]). It is assumed that ports 1 and 2 are symmetric. This model is automatically generated by *EMSight*.

- The circuit element *CPWBENDX* finally is a circuit component that models a CWG 90°-bend including the effects of airbridges to suppress the excitation of a slot line

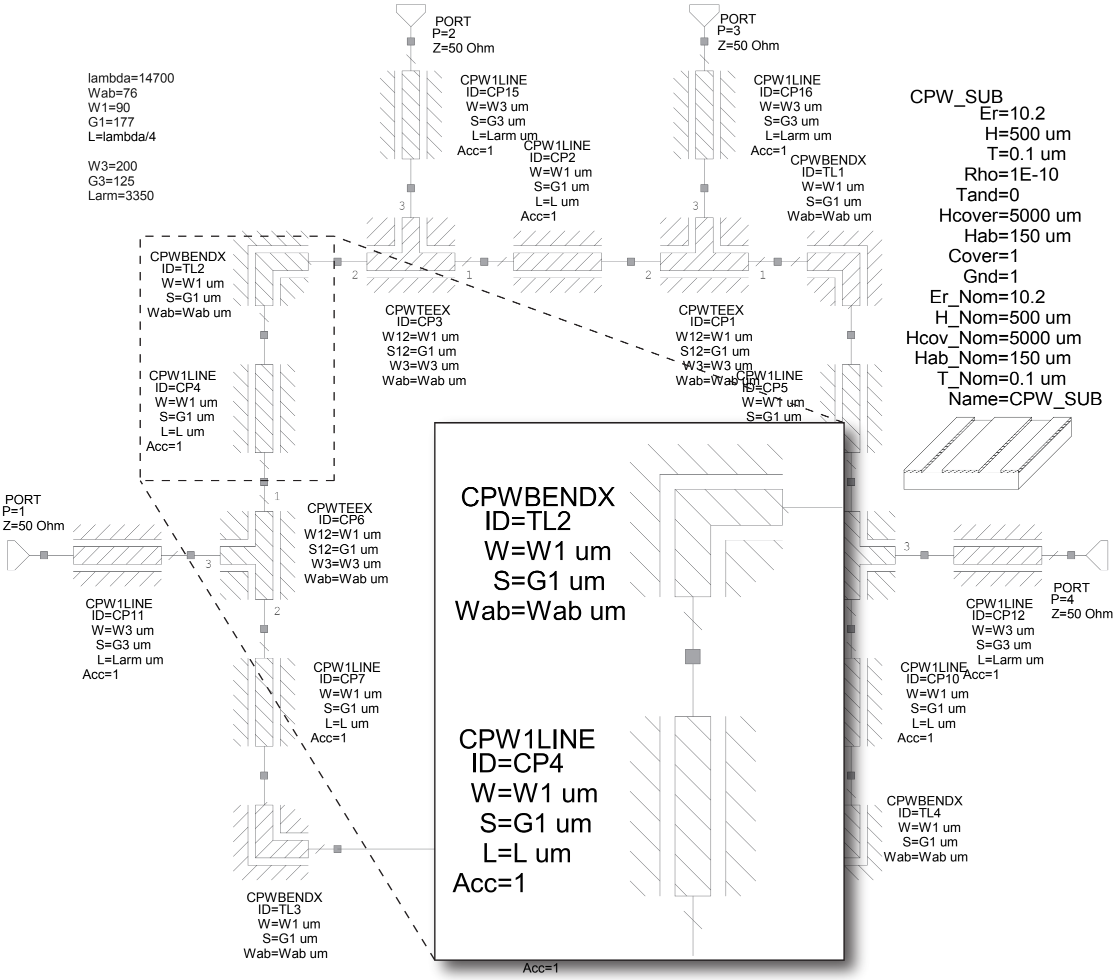

Figure 3.10: The complete schematic of the hybrid ring as simulated by MWO. The inset shows an enlarged detail of the schematic.

mode between the two ground planes. This model is also automatically generated by *EMSight*.

Moreover, the elements are assumed to have no conductor and dielectric losses and they are assumed to be dispersion-less. Superconductivity can not be simulated with this software. After having designed the hybrid ring, the schematic was simulated using the *Linear Simulation Engine*, which uses the nodal admittance matrix (2.120) method. This method computes the response of the linear N port network from its admittance matrix equivalent. MWO is a very fast simulation program if one only changes parts of the model in the circuit that do not affect the substrate. As soon as a substrate parameter (e.g. dielectric constant or substrate height) is changed, the program needs to start a time consuming calculation. The reason for this is that each *EM Sight*-based model in MWO operates on a table of data generated for this model on a particular substrate. This table stores the results of

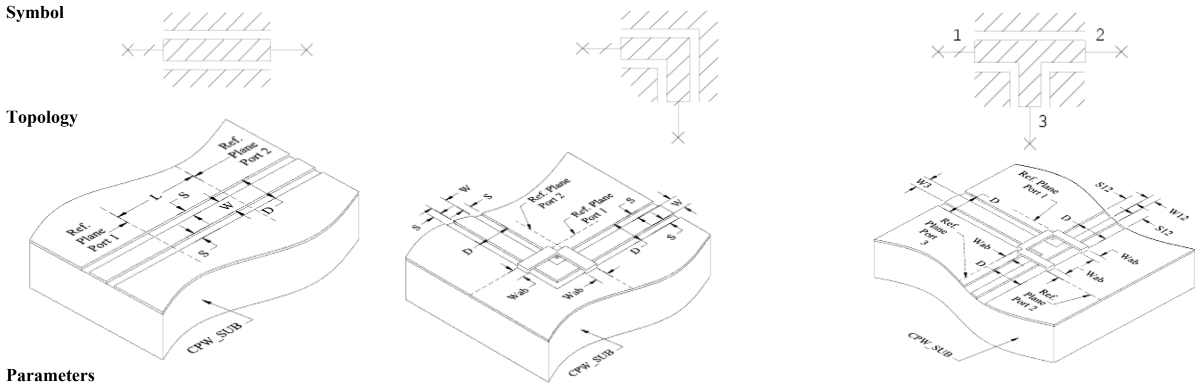

Name	Description	Unit Type	Default
ID	Name	Text	CP#$^{(1)}$
W	Conductor width	Length	W$^{(2)}$
S	Left/right gap width	Length	W$^{(2)}$
L	Conductor length	Length	L$^{(3)}$

(a)

Name	Description	Unit Type	Default
ID	Element ID	Text	CP#1
W	Conductor Width	Length	W^{2}
S	Gap Width	Length	W^{b}
Wab	AirBridge Conductor Width @ Port 1&&2	Length	W^{b}

(b)

Name	Description	Unit Type	Default
ID	Element ID	Text	CP#$^{(1)}$
W12	Conductor Width @ Port 1&&2	Length	W$^{(2)}$
S12	Gap Width @ Port 1&&2	Length	W$^{(2)}$
W3	Conductor Width @ Port 3	Length	W$^{(2)}$
Wab	AirBridge Conductor Widths @ All Ports	Length	

(c)

Figure 3.11: Pre-defined circuit elements available in MWO used for the circuit design of the hybrid. (a) Conductor backed CWG section (quasi-static): CPW1LINE. (b) 90°-bend (*EMSight*-based): CPWBENDX. (c) Symmetric T-junction (*EMSight*-based): CPWTEEX.

the *EMSight*-based simulations. During a concrete simulation, MWO interpolates the data in this table in order to estimate the electrical performance for the current set of input parameters. For common substrates, these tables are already generated by Applied Wave Research, Inc., thus saving the time required to fill the interpolation tables. To be able to use such a table, the following substrate parameters were chosen:

> Dielectric constant $\varepsilon_r = 10.2$, dielectric loss tangent $\delta_e = 0$, Height $H = 500\,\mu$m. There are also other substrate parameters, but they are not of interest for this investigation.

The described filling procedure is perhaps the most inconvenient aspect of the programme.On the other hand, it is important, as after having filled the table, geometrical parameters of the structures in the schematic may be changed while S-parameters are simulated in real time. This makes designing and fine tuning of microwave circuits extremely comfortable and efficient.

Some selected results of the simulation of the hybrid ring in schematic 3.10 are shown in Figure 3.12. The geometrical parameters correspond to hybrid ring structure number H3 which was fabricated and measured within this work (see section 5.1, Tabular 5.1).

In these plots, the simulation results are compared to TLT. As TLT is loss-less, losses have to be ”introduced” in the theory by inserting a factor α_f. For the plots, α_f was set to $\alpha = 26 \cdot 10^6$/m. This factor results from a fit of TLT to the measurement data of hybrid ring H3. The procedure is explained in detail in section 5.4.1. For the moment, it is sufficient to know that inserting this factor and setting it to the mentioned value makes the plotted transmission line S-parameters correspond to the measurement data. Like this, the simulation results in turn may be compared to the measurement results, too.

Figure 3.12 demonstrates that MWO and TLT are in a good agreement concerning the devolution of the selected S-parameter curves. However, the frequency where S_{13} has its minimum (denoted as center frequency f_0) differs in the two approaches by $\approx$ 0.83 GHz. MWO predicts f_0 = 6.00 GHz, whereas TLT gives f_0 = 7.83 GHz. The absolute prediction of f_0 is very important as the bandwidth for isolation (S_{13}-parameter) of < -40 dB is very narrow. MWO and TLT estimate the following benchmarks:

center frequency	bandwidth	transmission	isolation
0 - 8 GHz	300 MHz	> -3.5 dB	< -40 dB

Nevertheless, f_0 can be determined by only one single experiment as shown in Chapter as it is in principle only dependent on the dielectric constant ε_r of the substrate. Once this ”iteration step” is done and ε_r is known, the absolute values for f_0 delivered by MWO and TLT may be corrected by an appropriate off-set.

The absolute values of the isolation is also not equal in both methods. The absolute difference is around 10 dB, the relative difference approximately 15%. This is a lot, but fortunately, this is not too important because the bandwidth around -40 dB is not much affected by changes of the absolute isolation below -50 dB as the peak is very sharp.

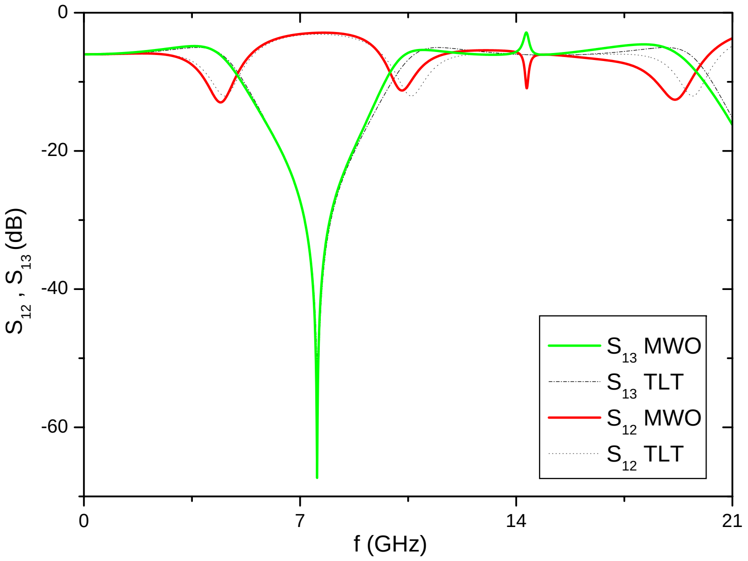

Figure 3.12: Comparison of S_{13} and S_{12} as simulated by MWO and calculated by transmission line theory (TLT).

To illustrate the importance of impedance matched microwave connectors for the performance of the hybrid ring, Figure 3.13 shows S-parameters calculated by MWO, where port 2 of the circuit schematic was set to an impedance of 55 Ohm which deviates from the optimal case of 50 Ω that can easily occur in real structures. These impedance discontinuities may occur due to additional parasitic inductances due to e.g. bonding wires and/or parasitic capacitances due to e.g. imperfect galvanic contacts (see 5.4.2). Impedance mismatches may also occur due to geometric discontinuities as mentioned in section 2.2.7.
To conclude this chapter, one can state that in contrast to transmission line theory, MWO also takes into account CWG discontinuities. Nevertheless, MWO and TLT are in very good agreement. In fact, the differences in the results of both approaches are that small, that the performed experiments cannot decide, which one models reality better – as one will see in Chapter 5. Improving the measurement data to be able to make this decision will be future work. For this reason, it seems to be sufficient for the moment to analyse the measurement data only with one of the two models. For data analysis, it seems more convenient to take TLT in conjunction with the closed-form expressions for superconducting CWGs. Although not able to simulate CWG discontinuities (TLT is even rather insensitive to changes in the characteristic impedances of its CWG sections Z_c and Z_1), TLT is preferable as it provides explicit formulas for the S-parameters which can be numerically fitted to the measurement data. In other words, a working theoretical model has the advantage of full control over all parameters entering the theory. This makes it possible to investigate

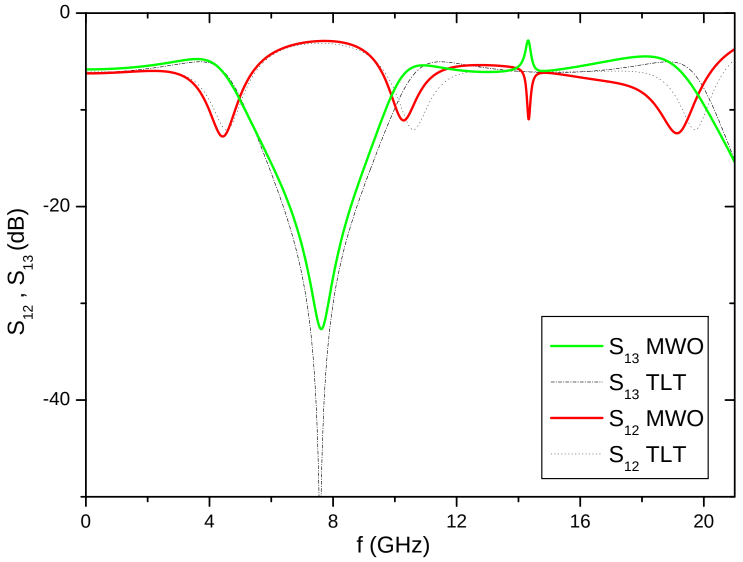

Figure 3.13: S_{13}- and S_{12}-parameters as simulated by MWO for the circuit schematic shown in Figure 3.10. An impedance mismatch of 5 Ω at port 2 causes the deviation from the corresponding S-parameters calculated by transmission line theory (TLT).

the effects that are related to these parameters.

MWO also does not account for direct crosstalk between the hybrid ring ports, when used in its *Schematic Circuit Design* mode only. EMSight could do this, but has a very inconvenient user interface, despite the fact that *EMSight* would be probably faced with the same problems as MWS. Nevertheless, MWO is in general very recommendable for the analysis of CWG structures as the hybrid ring, as it allows to extend the circuit schematic in a very easy way by additional microwave components. MWS however is not recommendable at all for such complex structures as the hybrid ring for the reasons already mentioned above. In reference [19], one can find a detailed list of additional commercially available accurate models for CWG discontinuities, such as open circuits and short circuits, lumped elements, such as inductors and capacitors, and three and four-port junctions, such as, T- and cross junctions. In addition, one can find a summary of commercially available electromagnetic simulation software for 2-D and 3-D structures.

Chapter 4

Fabrication

4.1 Sample Fabrication Processes

Within this work, superconducting niobium CWG structures have been produced on sapphire substrates. The CWG structures have been fabricated using standard clean room processes and sputtering of niobium . In this chapter, two fabrication processes developed within this work will be presented.
The fabrication processes are shown schematically in Figures 4.1 for P1 and 4.2 for P2. The most important fabrication parameters as well as some comments on the process steps for P1 and P2 are summarized in Table 4.1. A very detailed and practical description of several clean room processes is given in [56].

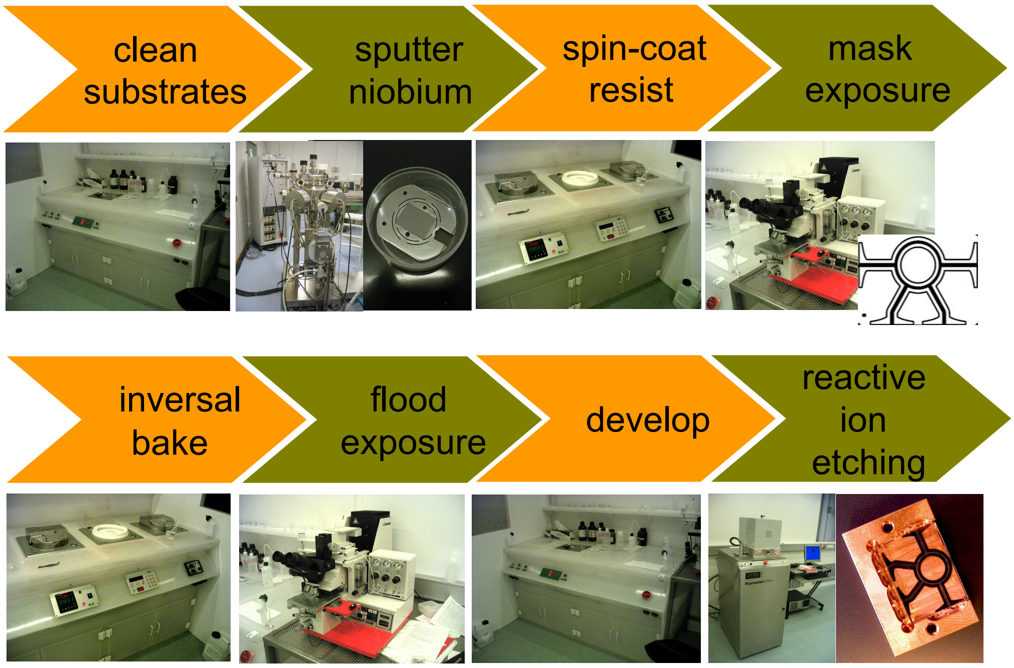

Figure 4.1: Overview over the niobium CWG fabrication process using ion etching (process P1).

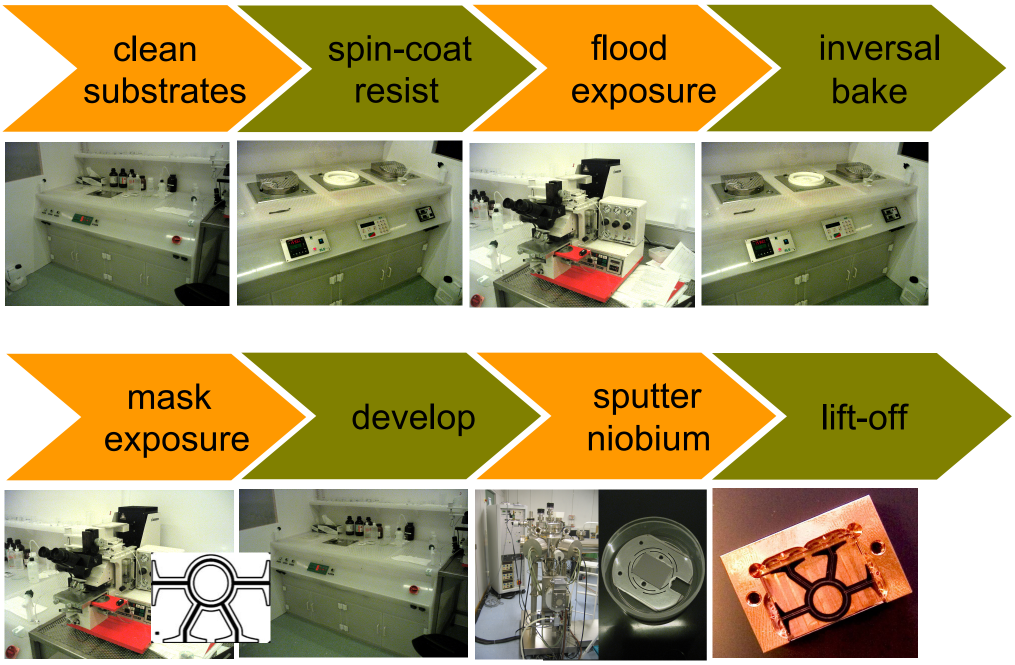

Figure 4.2: Overview over the niobium CWG fabrication process using final lift-off (process P2).

Parameters of the Fabrication Processes

process step	process parameters
cleaning the quartz mask	• cleaning with: 1. acetone, 2. acetone (p.a.), 3. isopropanol (p.a.) • dry with nitrogen N_2 • cleaning with so-called piranha etch (mixture of sulfuric acid (H_2SO_4) with hydrogen peroxide (H_2O_2) 3:1) for insistent organic residues [1] • do not touch the chromium surface at all

---

[1] Be careful when preparing a piranha etch, as it starts an extremely exothermic self starting reaction. The mixture becomes hot when the hydrogen peroxide is added to the sulfuric acid. Never add the acid to the hydrogen peroxide as this can cause an explosion!

process step	**process parameters**
cleaning the samples	• see cleaning the mask, in addition each cleaning step (except of piranha etch) should be supported with ultrasonic (2 min, power 4) • additionally, substrates may be mechanically precleaned by a teflon tweezer which was wrapped by a precision wipe
spin-coating the resist	• resist: AZ© 5214E Image Reversal Photoresist (MicroChemicals [57]) • spin speed: 4000 rpm @ 40 s (acceleration: 4 s)
hot plates	• soft bake: 111° C @ 70 s • inversal bake: 120° C @ 120 s • 4000 rpm @ 40 s
developing	• developer: AZ© developer : H_2O (1:1) • P1: 1:15 - 1:40 min (typ. 1:25 min), P2: 5:20 - 6:30 min
exposure	• Mask aligner (MJB3, Karl Süss GmbH) • flood exposure process P1: 15 s, P2: 0.5 s • mask exposure process P1: 8.5 s, P2: 7.9-8.5 s (typ. 8.2 s)
sputtering niobium	• process pressure: $4.7 - 4.9 \cdot 10^{-3}$ mbar • power: 50 W • duration: 600 s (presputtering 60 s) • Ar flow rate: 5 sccm/min • sputter rate: $\approx$ 10 nm/min

process step	**process parameters**
RIE (Plasmalab 80 Plus ICP65, Oxford Instruments Inc.)	Step 1: etching • duration: 210 s • Ar flow rate: 10.0 sccm/min • SF_6 flow rate: 20.0 sccm/min • 0_2, N_2 flow rate: 0 sccm/min • RF forward power: 15 W @ 13.56 MHz • ICP forward power: 300 W @ 13.56 MHz • Chamber pressure: 15 mTorr • He backing flow rate: 10.0 sccm/min • Temperature 20° C
	Step 2: ashing • duration: 30 s • 0_2 flow rate: 50.0 sccm/min • Ar, SF_6, N_2 flow rate:0 sccm/min • RF forward power: 100 W @ 13.56 MHz • ICP forward power: 0 W @ 13.56 MHz • Chamber pressure: 30 mTorr • He backing flow rate: 10.0 sccm/min • Temperature 20° C

Table 4.1: Details of Process P1 and P2.

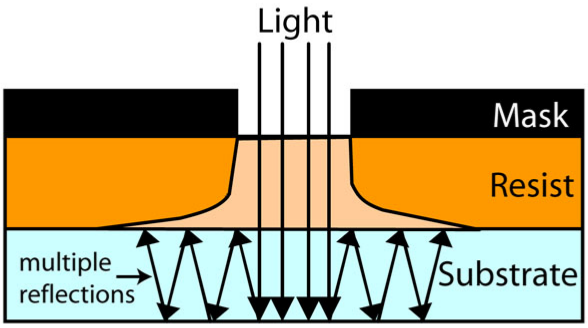

Figure 4.3: During light exposure in the mask aligner, light is reflected from the backside of the transparent sample and the chuck and then multiply reflected within the transparent substrate.

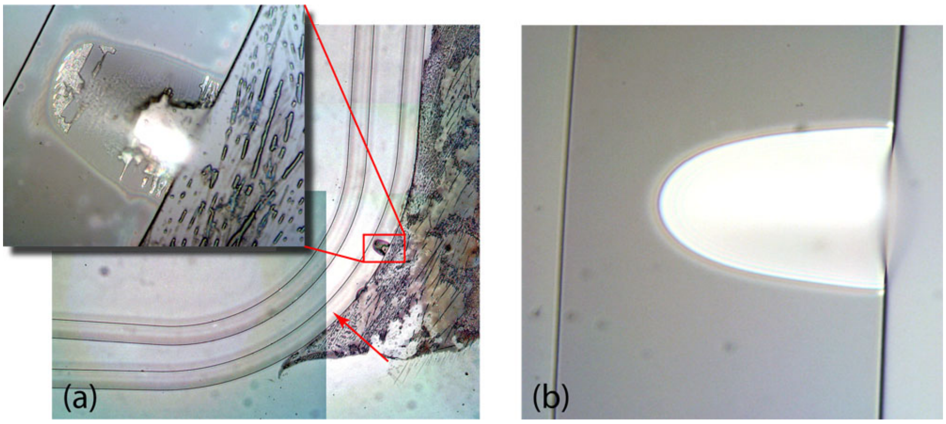

Figure 4.4: Microscope pictures of badly structured resist due to multiple reflections. (a) The red arrow indicates the region of the curved CWG where the center strip width has become narrower. Due to the multiple reflections, the resist was overexposed and thus, during the development process, too much of the resist was dissolved. The inset shows an enlargement of the area in the red box. One can see that parts of the center strip were completely dissolved. (b) Detailed view of a lifted center strip conductor.

The first process (denoted by P1) using reactive ion etching (RIE [2]) turned out to be more stable and reproducible for arbitrary structures than the second process (denoted by P2) using a lift-off process.

The reason for this is most probably the high transparency of the sapphire substrates. During light exposure in the mask aligner, light is reflected from the backside of the transparent sample and the chuck and is then multiply reflected within the substrate (see Figure 4.3). Therefore, the light can also illuminate part of the resist which was initially covered by the mask. This leads to a loss of resolution in patterning the resist by widening the structures.

---

[2] In a RIE process, the substrate is placed inside a reactor in which several gases are introduced. A plasma is struck in the gas mixture using an RF power source, breaking the gas molecules into ions. The ions are accelerated towards, and react at the surface of the material being etched, forming another gaseous material. This is known as the chemical part of reactive ion etching. The processes used within this thesis uses a SF_6. Flourine radicals chemically etch the Nb.

There is also a physical part which is similar in nature to the sputter deposition process. If the ions have high enough energy, they can knock atoms out of the material to be etched without a chemical reaction.

It is a complex task to develop dry etch processes that balance chemical and physical etching, since there are many parameters to adjust. By changing the balance it is possible to influence the anisotropy of the etching, since the chemical part is isotropic and the physical part highly anisotropic the combination can form sidewalls that have shapes from rounded to vertical.

”Sputter etching” is essentially RIE without reactive ions. The systems used are very similar in principle to sputtering deposition systems. The big difference is that the substrate is now subjected to the ion bombardment instead of the material target used in sputter deposition.

This as well as additional information about RIE processes can be found in the internet: http://www.memsnet.org/mems/processes/etch.html,2006.

More severe however was the fact that the resist was lifted from the substrate and displaced during the development process as shown in Figure 4.4. This problem of multipe reflections could be improved by placing a black piece of paper under the substrate. Moreover, a new chuck has been fabricated with blackened surface (see Appendies B.1 to B.3).
The transparency is also crucial when trying to optimize P2 for minimally pronounced edge beads (*dt. Randüberhöhung*), as the mask exposure times may not be too long. A time-consuming optimization of the mask exposure and developing times could considerably improve process P2 with respect to edge beads.
Moreover, the Nb layer in P1 can be much thicker (even thicker than the resist) than in P2. Lift-off becomes difficult even for Nb layers with a thickness smaller than the resist thickness. The reason for this limitation of the lift-off process in combination with sputtering is the isotropy of the sputtering process: the sputtered metal is deposited everywhere (also on the resist side walls); resist which is covered by metal cannot be removed by the lift-off process .

> Therefore, it is recommended to use process P1 if the metal layer can be removed by RIE.

Within this work the RIE process P1 has been used for niobium structures on sapphire substrates only. P2 can be used for every kind of metal layer considering the above mentioned drawbacks.
Some additional practical remarks on the fabrication processes:

- The cleaning process of the substrates at the wet benches should be followed by a 120° C hot plate bake to remove any excess solvents and moisture that remained on the substrate surface.

- The etching time in process P1 is relatively long because of the fact that the niobium surface with a thickness of $\approx$ 100 nm has to be removed *completely* from the substrate to avoid short circuits in the CWGs. But this is not a crucial process step as one can start with a short etching time and than repeat the etching until all the niobium has been removed. By doing this, the mentioned total etching time was reached.

- After etching, the ashing step is performed to remove the resist from the structure. The O_2 in this step reacts selectively to underlying non-organic layers. The duration of this step should be at least 30 *s*. Otherwise, the remaining resist has to be removed by repeatedly cleaning the samples as explained in Table 4.1. To support this procedure, the cleaning procedure may also be performed in boiling acetone and isopropanol. The ashing step presented here has surely still some improvement opportunities.

- According to the data sheet of the AZ© 5214E Image Reversal Photoresist [57], a spinning speed of 4000 rpm should result in a resist thickness of 1.4 μm.

- The dimensions of the fabricated structures are way above the resolution limit of standard photolithography which is around 1 μm.

- The sapphire substrates were delivered by Mateck GmbH[3]. They have the following specifications:
  - orientation: (0001) ± 0.5°
  - size: 15 mm × 20.4 ± 0.1 mm
  - thickness: 0.5 mm ± 0.05 mm
  - epi-polished on both sides
- The quartz glass mask with chromium surface was ordered at ML&C GmbH[4].

Examples of fabricated structures together with their corresponding mask data are shown in Figure 4.5. The structure shown in Figure 4.5(b) was fabricated using process P2. The remaining edge beads of the resist mentioned above prevented the Nb from covering also the edges and corners of the substrate. Fortunately, this is not affecting the microwave properties lying far enough away from the CWG center strip conductor. Hybrid H3 shown in Figure 4.5(d) has been fabricated using process P1. Here, the vast tapered ground planes end just at the edges of the substrate. The Nb remainder in the lower left corner of the substrate is due to an imperfectly spin-coated resist.

4.2 Sample Preparation

To be able to measure the coplanar structures, they were inserted in specially machined sample holders (see Appendices B.8 to B.12) and connected to the measurement circuitry via ANRITSU V Connector components [5]. A detailed overview over the connectors and their assembly is given in Figure 4.6.
After mounting the samples, they have to be galvanically connected to the connectors. Within this thesis, two types of galvanic contacts have been investigated:

1. Bonding with Aluminium wire from the stress relief (see Figure 4.6(a)) to the center strip of the CWG and from the bonding planes inside the sample holder copper box to the ground planes of the CWG structures as shown in Figures 4.7(a) to 4.7(c). S-parameter measurements showed that bonding wires are no a good solution for contacting the center strip at all. It turns out that there is a parasitic capacitance between the center strip and the stress relief. This effect can be reduced by the application of silver glue. Nevertheless, the bonding wires constitute an extra series inductance which seems not to be negligible compared to the inductance of the CWG. This leads to a discontinuity in the characteristic impedance of the line and finally to unwanted reflections.

2. Silver glue between the stress relief and the center strip, as well as between the inner walls of the sample holder box and the ground planes of the CWG structures . It was

---

[3] Mateck GmbH, Hugo Schlich, http://www.mateck.com/ (2006)

[4] ML&C GmbH, http://www.mlc-jena.de/ (2006)

[5] Anritsu GmbH, http://www.anritsu.de/ (2005)

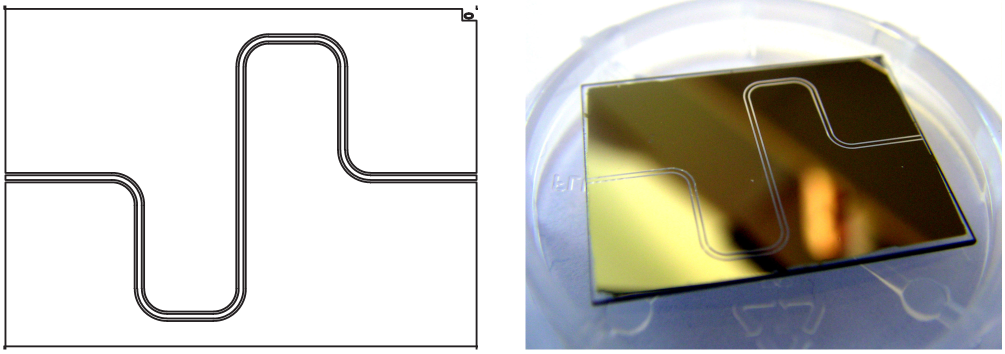

(a) Mask data for structure M1: meander-like CWG transmission line.

(b) Photograph of a fabricated M1 structure.

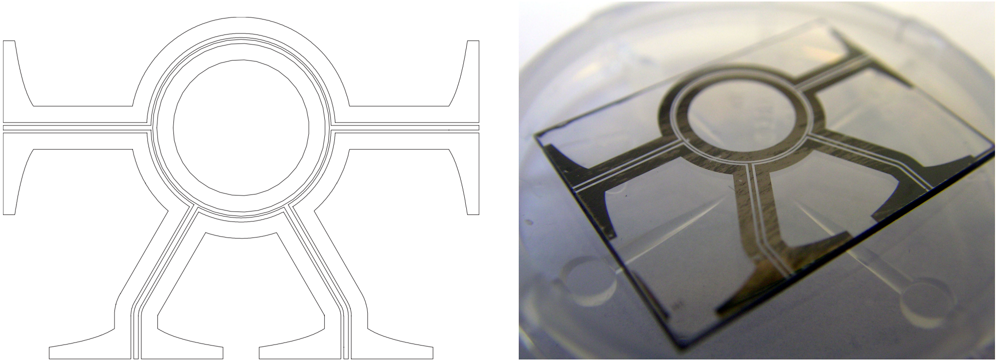

(c) Mask data for a hybrid ring structure used to produce structure H3 (H2 and H4 similar).

(d) Photograph of a fabricated hybrid ring H3 structure.

Figure 4.5: Mask data and photographs of fabricated and measured Nb structures on sapphire.

> found by S-parameter measurements, that for this kind of galvanic contact, it is even better not to use the stress reliefs as shown in Figures 4.7(e) and 4.7(f).

The silver glue can be applied by a sharpened toothpick and a calm experimenter (eventually equipped with Augustiner[6]). The bonding wires can be attached using a bonding machine. For this purpose, the bonding machine should be equipped by a microscope that can be adjusted quite flexible. Otherwise it is hard to look at all positions where bonds have to be placed. Therefore, a special microscope adapter was produced for the bonding machine at the WMI. To guarantee a good connection between the CWG ground planes and the (grounded) sample holder, the hybrid rings were designed with vast tapered ground planes (see Figure 4.5(b)).

Figure 4.7(c) shows an example for the limitations in achievable machining accuracy. The center conductor of the ANRITSU connector is not centered in the borehole. This will surely cause an impedance discontinuity and thus reflections. As stated in Appendix B, this problem could be improved by fabricating the sample holder in brass, with the drawback of much lower heat conductivity which becomes a problem at very low temperatures in the mK-regime.

---

[6] http://www.augustiner-braeu.de/

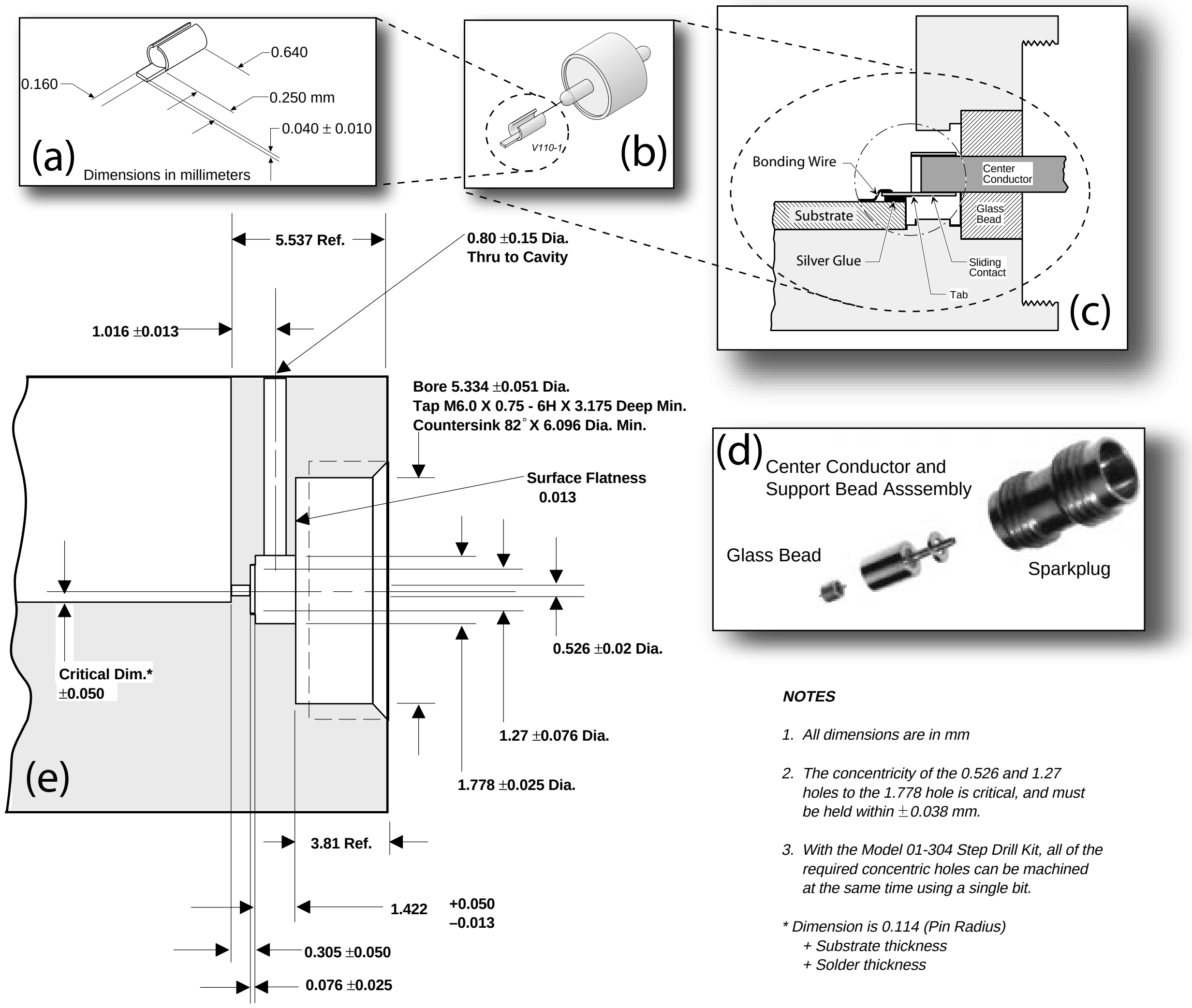

NOTES

1. *All dimensions are in mm*
2. *The concentricity of the 0.526 and 1.27 holes to the 1.778 hole is critical, and must be held within ± 0.038 mm.*
3. *With the Model 01-304 Step Drill Kit, all of the required concentric holes can be machined at the same time using a single bit.*

** Dimension is 0.114 (Pin Radius)*
+ Substrate thickness
+ Solder thickness

Figure 4.6: Overview over the ANRITSU V Connector components and their assembly used to contact the CWG structures in the sample holders (see B.8 to B.11) to the measurement circuit. (a) Sliding contact for microstrip and CWG, Model V110-1 (also called ”stress relief”). (b) Assembly of stress relief and glass support bead, Model V100. (c) Crosscut of the sample holder with installed glass bead and stress relief. Also marked are the positions for possible bonding wires and silver glue. (d) Assembly of glass bead and microstrip/CWG to V female sparkplug connector, Model V102F (also available are V male sparkplug connectors, Model V102M). The shown center conductor and support bead assembly are part of the Model V102F and make the transition from the glass bead to V male/female in-line cable connectors, Model V101M/F (not shown here), respectively. (e) Dimensions of the boreholes in the sample holder for the installation of the glass bead and sparkplug connector.

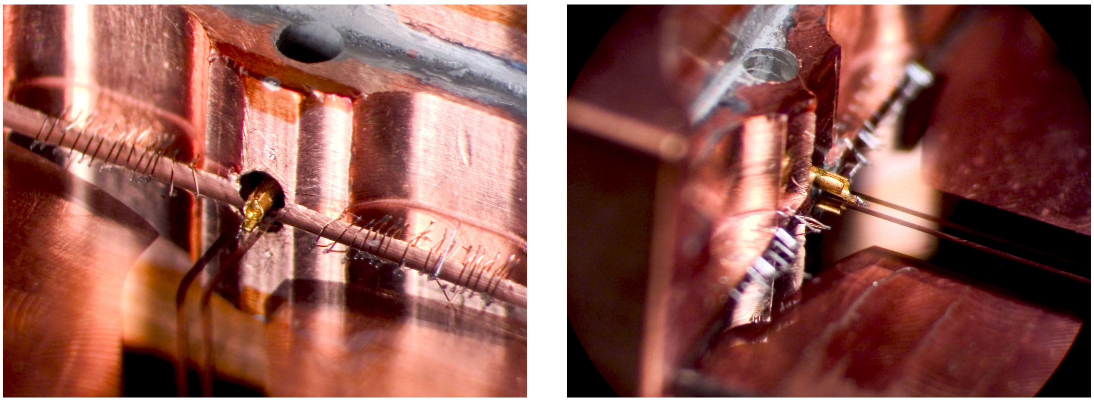

(a) Front view of the bonding wires and the ANRITSU connector.

(b) Side view of the bonding wires and the ANRITSU connector.

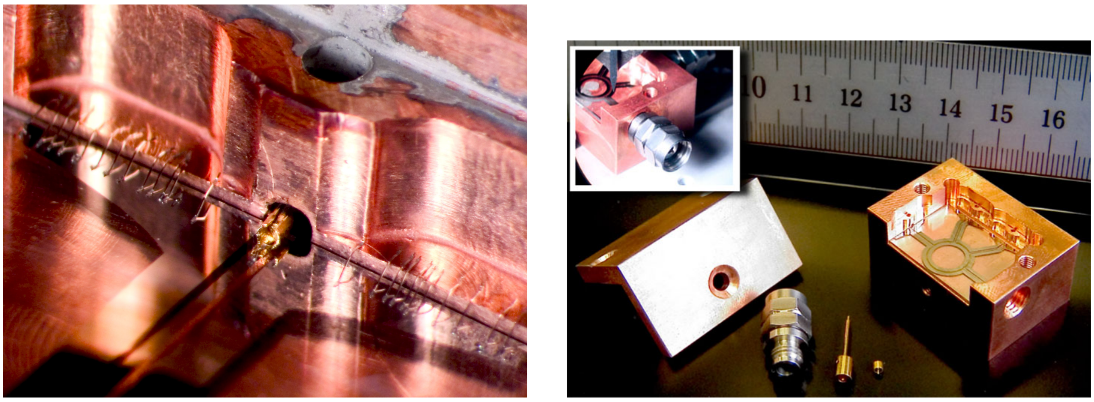

(c) The center conductor of the ANRITSU connector is not centered in the borehole. This will surely cause an impedance discontinuity and thus reflections.

(d) Top metal cover of the sample holder, sparkplug connector and its center conductor, glass bead and sample holder box with hybrid structure (from left to right). The inset shows the installed sparkplug cennector.

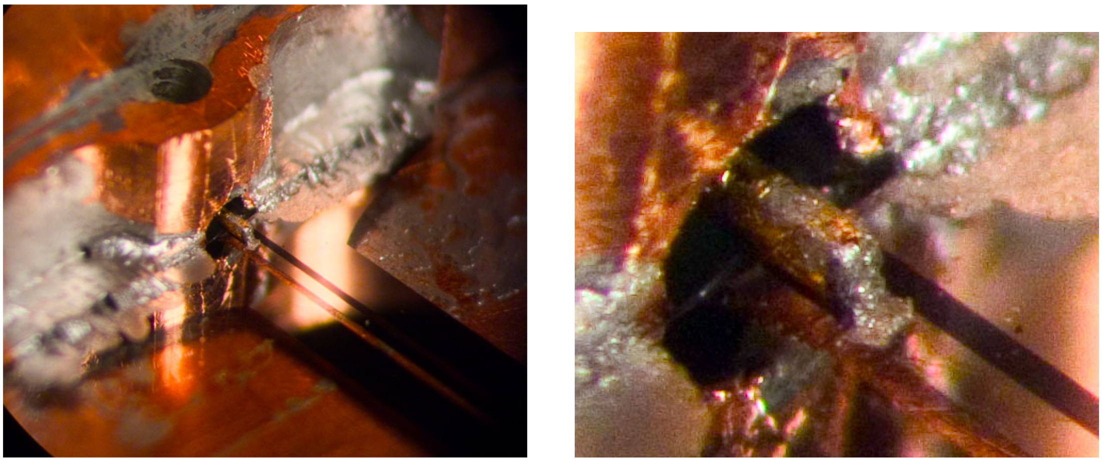

(e) View of a connection done with silver glue.

(f) Detailed view of 4.7(e).

Figure 4.7: Two types of galvanic contact: bonding wires (4.7(a)-4.7(c)) and silver glue (4.7(e) and 4.7(f)). 4.7(d) shows the ANRITSU V Connector components and the sample holder.

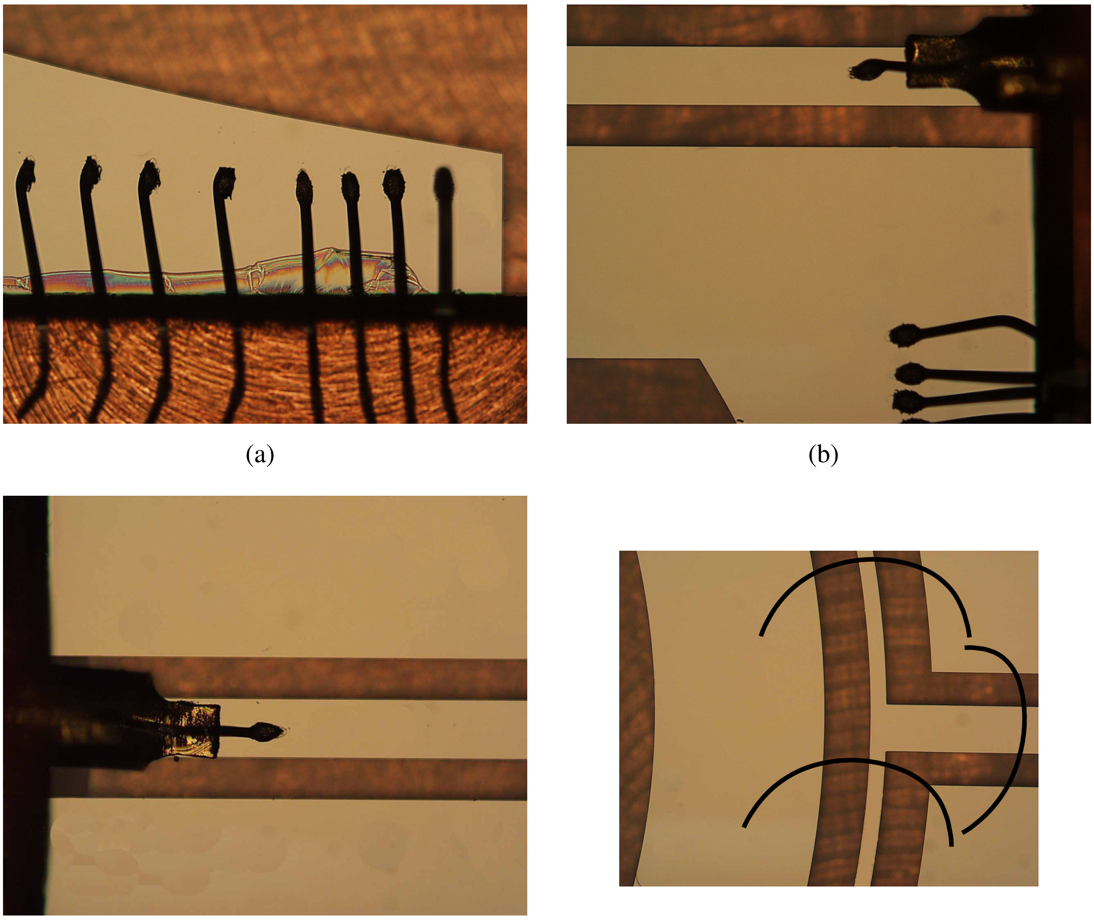

(a) (b)

(c) (d)

Figure 4.8: Microscope photographs of a tapered ground plane with bonding wires (a) and a bonded stress relief mounted on the center conductor of a V-connector (b, c). Figure (c) shows the connection of the hybrid arms with the hybrid ring (so called T-juntion). The so called airbridges one can see in this picture are only drawn. They are realized using bonding wires that connect opposite ground planes as explained in reference [19]. Further explanations on airbridges are presented in section 5.4.2.

Chapter 5

Measurements

5.1 Introduction

In this work, the S-parameters of four CWG structures have been measured with a HP8722D network vector analyzer (NVA). A meander-like CWG transmission line (denoted by M1, see Figure 4.5(a)) and three hybrid rings (denoted by H2, H3 and H4, see Figure 4.5). The relevant dimensions of the structures are summarized in Table 5.1. The calculated characteristic impedances Z_1 and Z_c of the corresponding transmission line sections (M1 only has one characteristic impedance Z_c, the characteristic impedance of the hybrid ring arms is Z_c, the one of the ring is Z_1, see section 2.3) and their ratio are also given there. The characteristic impedances have been calculated using the formulas given in section 2.4.2.

First some words will be spent on the measurement setup and the measurement technique used for measuring the S-Parameters of the structures. Then, the results of the measurements will be given for the meander structure M1 and for the hybrid structures H2 - H4.

5.2 Measurement Setup and Calibration Technique

The measurement setup is shown schematically in Figure 5.1. With this setup, S-parameters of a device under test (DUT) can be measured versus temperature. The DUT is located in a dewar which can be filled with liquid helium, allowing measurements between room temperature and 4.2 K. To be able to do this in an accurate way, the HP8722D NVA calibration data have to be taken at the temperature values of interest. For the calibration, the data

	M1	H2	H3	H4
L (mm)	39.93	–	–	–
R (mm)	–	3.825	3.825	3.825
H (μm)	500	500	500	500
W (μm)	200	200	200	200
G (μm)	105	125	125	125
Z_c (Ω)	50.3	52.5	52.5	52.5
W_{Ring} (μm)	–	75	90	105
G_{Ring} (μm)	–	177	177	177
Z_1 (Ω)	–	77.6	73.6	70.3
Z_1/Z_c	–	$\sqrt{2.18}$	$\sqrt{1.97}$	$\sqrt{1.79}$

Table 5.1: Dimensions of the measured structures: meander-like CWG transmission line M1, and hybrid rings H1, H2, H3. For the calculation of the characteristic impedances (with formulas presented in 2.4.2 and values for niobium taken from 2.1), it was assumed: $\varepsilon_r = 10$, $T = 4.2$ K , $t = 100$ nm.

read-out and control of the NVA via IEEE interface, a PC equipped with LabView[1] is used. All measurements were performed with an input power of -10 dBm (default for the NVA). For input powers much lower than this value, the S-parameter measurements became very noisy. The S-parameters did not change by increasing the input power.

During a frequency sweep, the NVA takes measurements at 1601 different frequency values maximally. The measurements for this thesis have been taken in the frequency range from 3 to 11 GHz and from 0 to 21 GHz respectively, resulting in a frequency resolution of 5 MHz and 13 MHz, respectively. The temperature of the sample was recorded using a NEOCERA LTC-21 temperature controller and a silicon diode attached to the outer surface of the sample holder. A short explanation of the functionality of a NVA can be found in reference [4]. For a more detailed introduction see references [17] and [18].

To be able to measure S-parameters with a NVA, it is necessary to perform a measurement calibration [58, 59]. This is a process in which a network analyzer measures precisely known devices and stores the vector differences between the measured and the values. The error data is used to remove systematic errors from subsequent measurements of unknown devices. HP8722D NVA has six types of calibrations available for 2-port measurements: response, response & isolation, S_{11} 1-port, S_{22} 1-port, full 2-port and TRL 2-PORT. Each of these calibration types solves for a different set of 12 systematic measurement errors (6 forward and 6 reverse error terms). These are all systematic errors, namely (see Figure 5.2):

- Coupler directivity (1) and crosstalk (2) errors leading to signal leakage.
- Source (3) and load (4) impedance mismatches resulting in to reflections.
- Frequency response errors caused by reflection (5) and transmission (6) tracking within the test receivers.

Not corrected by any kind of calibration are of course random errors and drift errors.

Response calibration is the simplest to perform as no reference device at all is needed, but corrects for only two of the 12 possible systematic error terms, namely, two frequency response errors caused by reflection *or* transmission tracking in reflection or transmission measurements, respectively. A response calibration only requires one standard each for transmission (a thru) and reflection (a short or open).

Response calibration is a normalized measurement in which a reference trace is stored in the network analyzers memory, and later on the measurement data is devided by the stored trace for normalization. The lack of correction for source and load impedance mismatch is especially troublesome for low-loss transmission measurements (such as an ordinary transmission line, like structure M1 of this thesis), and for reflection measurements. Using response calibration for transmission measurements on low-loss devices can result in considerable measurement uncertainty in the form of ripples in the measurement spectra . However, the accuracy of a calibration is always relative. Whether a calibration is accurate enough or not depends on the requirements one imposes on the measurements and the DUT.

---

[1] National Instruments, http://www.ni.com/ (2006)

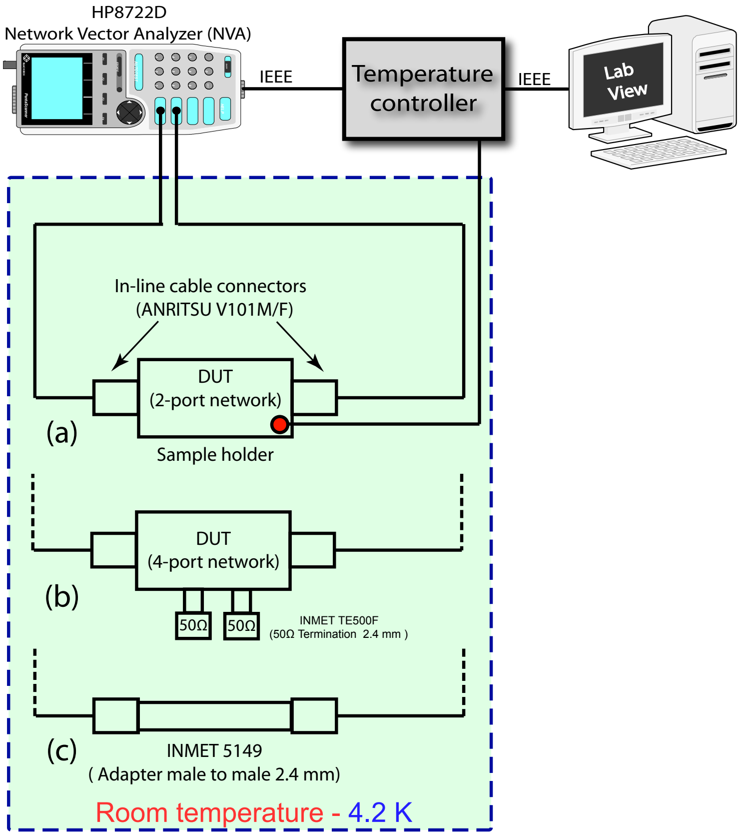

Figure 5.1: Measurement scheme. The S-parameter measurements were performed using a HP8722D network vector analyzer (NVA). The NVA was controlled and read out by LabView via IEEE interface. Moreover, the temperature of the sample was recorded using a NEOCERA LTC-21 temperature controller and a silicon diode attached to the outer surface of the sample holder. (a) Scheme for the measurement of a 2-port device. (b) Scheme for the measurement of a 4-port device. As the NVA has only 2 ports, the other ports of the 4-port device have to be terminated via 50 Ω terminations. (c) The NVA was calibrated by replacing the device under test (DUT) by an INMET 5149 adapter male to male.

The response calibration scheme performed in this work shown in Figure 5.1(c) was done with a 2.4 mm INMET 5149 adapter (male to male) inserted in the measurement circuit which was later on replaced by the DUT. As the calibration was not corrected by the attenuation and electrical length of this adapter, a systematic error in the response calibration is present. This procedure was necessary because the DUT together with a 2.4 mm INMET 5149 adapter (female to male) did not fit into the dewar. Data of such a temperature dependent calibration for the S_{34}-parameter is shown in Figure 5.3. As one can see, the measure-

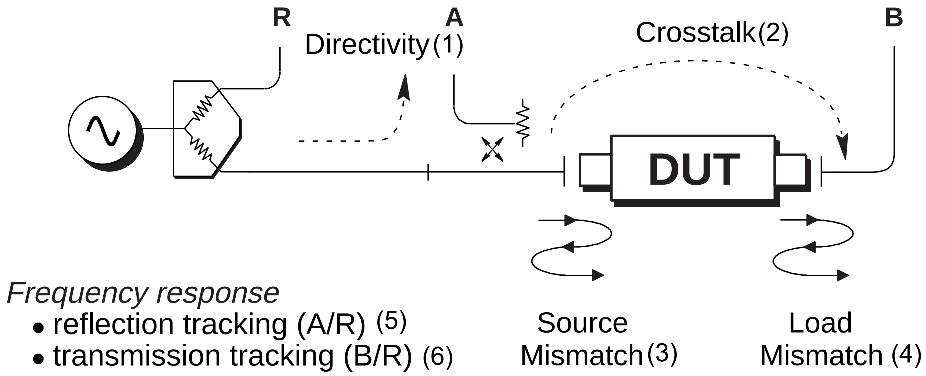

Figure 5.2: Model of a two-port NVA illustrating the six forward error terms. Together with the six reverse errors *not shown* here), this yields 12 error terms.

ment circuitry shows a significant temperature dependence ($S_{34}(234\,\mathrm{K}) - S_{34}(4\,\mathrm{K}) \approx -3.3$ dB).

The *error due to the attenuation* caused within the adapter can be assumed negligible in comparison to firstly the systematic errors which are not corrected by the response calibration and secondly the attenuation of the transmitted signals within the test structures.

The electrical length of the adapter however is in the order of the wavelength (≈ 2 cm @ 6 GHz) causing a severe systematic *error on phase measurements* of the transmitted signal. But as phase measurements were not performed within this work, this error did not play a role.

To get a feeling for the accuracy that can be achieved with a response calibration, the S_{12}-parameter of an INMET 40 EH-10 10 dB-attenuator has been measured. The results are shown in Figure 5.5(a)(b) at room temperature.

According to the technical data sheet [2], this attenuator has a maximum tolerance of attenuation of ±0.5 dB. Thus, in the worst case, the attenuation of the attenuator is -10.5 dB or -9.5 dB. The measured attenuation according to Figure 5.5(b) varies between -10.0 dB and -10.5 dB.

> This gives a **worst case approximation of the achievable measurement accuracy of** ±1.0 **dB** for the present measurement scheme with response-calibration.

The measurements of the 10 dB-attenuator at 77 K are not important for the estimation of the accuracy as the attenuator is not specified at this temperature. The results are given for the interested reader and show that the attenuator can be regarded as perfect down to 77 K within the achievable measurement accuracy.

To conclude the discussion about calibration techniques, it should be pointed out that the response calibration as performed here has a big disadvantage, as it can never allow to ”see” the pure coplanar structures themselves. Instead, one always measures the S-parameters of

---

[2] AEROFLEX INMET Corp., http://www.aeroflex-inmet.com/ (2006)

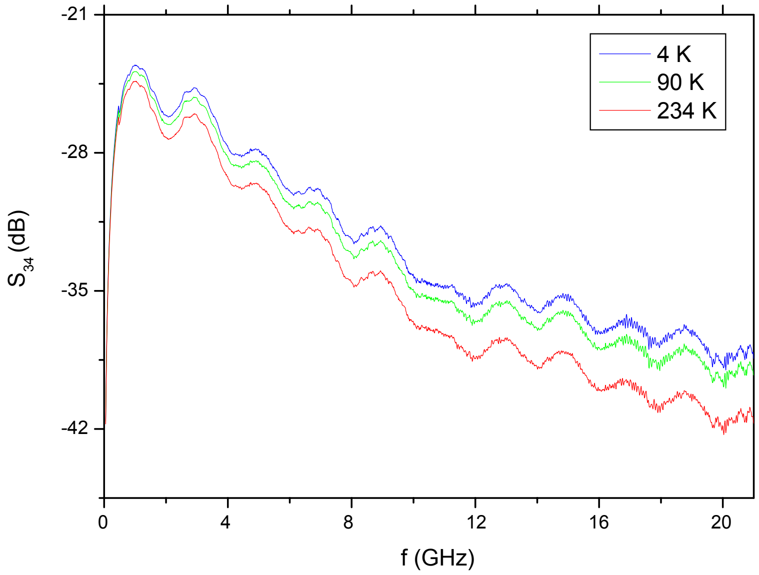

Figure 5.3: The response calibration for the measurement setup. The calibration data is strongly temperature dependent.

the whole DUT, meaning the coplanar structures plus the ANRITSU V Connector components including eventually present bonding wires and silver glue as shown in Figure 4.6. Although negligible for the CWG properties as shown in 2.4.2, the sample holder itself can contribute to the S-parameter measurements, especially by supporting unwanted resonances within the copper box.

To be able to measure a coplanar structure, a TRL (**T**hru-**R**eflect-**L**ine) calibration (or one of its numerous variations like LRL (**L**ine-**R**eflect-**L**ine)) is best suited and relatively easy to perform [58]. The big advantage of a TRL calibration originates from the fact that one can fabricate the calibration standards together with the coplanar test structures oneself and thus make them compatible to the sample holder and coplanar connectors which are already existent in the measurement setup. The requirements on TRL calibration standards are comprehensively summarized in reference [58].

Performing a TRL calibration will be subject to future work at the WMI.

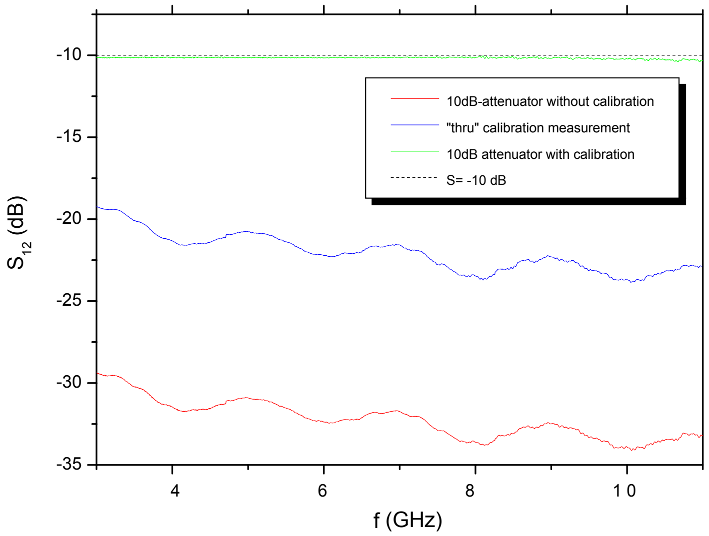

(a)

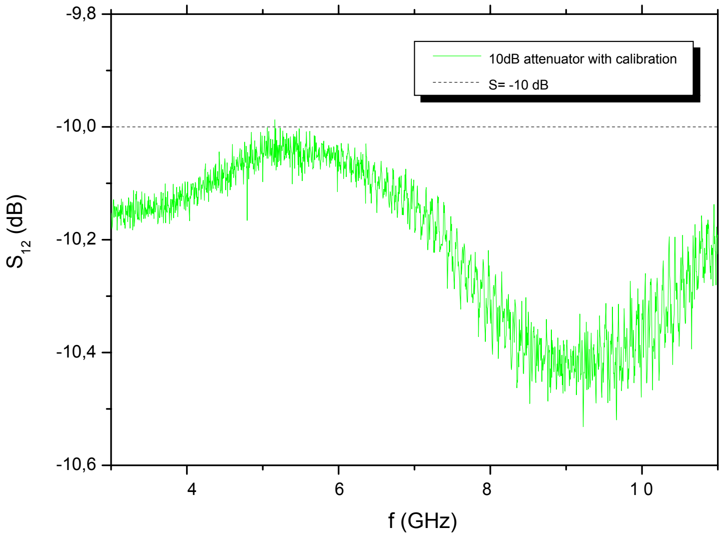

(b)

Figure 5.4: The S_{12}-parameters of an 2.4 mm INMET 40 EH-10 high frequency 10 dB-attenuator at room temperature. (a) uncalibrated measurement, calibrated measurement and ”thru” calibration measurement. One gets the calibrated data by subtracting the ”thru” calibration data from the uncalibrated measurement data (if data is given in dB). (b) enlargement of calibrated data as seen in (a).

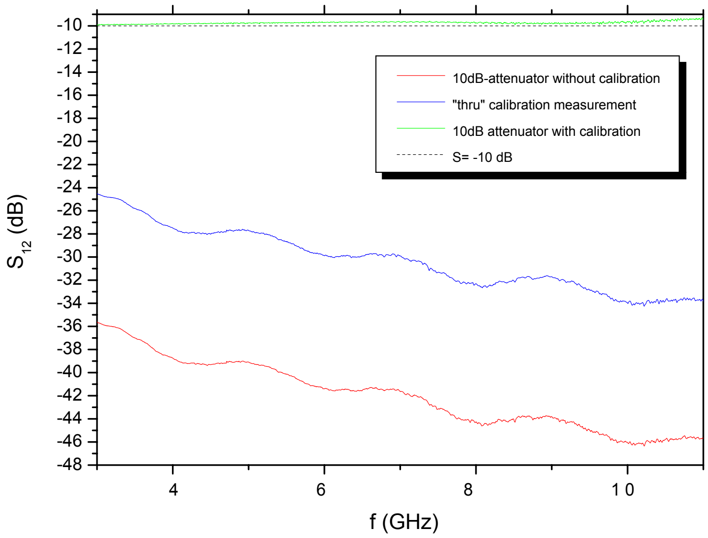

(a)

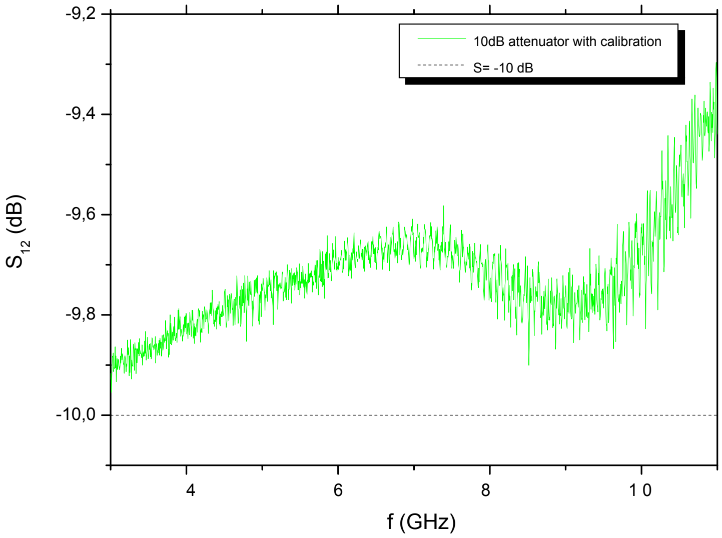

(b)

Figure 5.5: The S_{12}-parameters of an 2.4 mm INMET 40 EH-10 high frequency 10 dB-attenuator at 77 K. (a) uncalibrated measurement, calibrated measurement and "thru" calibration measurement. One gets the calibrated data by subtracting the "thru" calibration data from the uncalibrated measurement data (if data is given in dB). (b) enlargement of calibrated data as seen in (a).

5.3 Measurement of Structure M1

Structure M1 is a CWG transmission line. As it is a very simple structure, it was used to investigate the best way to connect the coplanar structures to the ANRITSU V-connectors. Two strategies have been examined as already mentioned in section 4.2. The corresponding measurements are shown in Figures 5.6 and 5.7(a). Measurements with bonded structures are indicated by (b), whereas measurement with silver glue connections are indicated by (sg).

5.3.1 Frequency Domain Measurement

The measurement in Figure 5.6(a) was performed at 4, 9 and 10 K. The measurement data at 9 and 4 K do not differ much. However, a slight decrease of the resonance dip at around 4 K is observable as expected from theory as the attenuation increases for $T \rightarrow T_c$. With the transition from the superconducting to the non-superconducting state between 9 and 10 K the attenuation strongly increases from around -1 dB to ¡ -10 dB for frequencies between approximately 0 and 8 GHz. In the normal conducting case, the resonance dip becomes very flat. It is barely visible. At 4 K, a Lorentz fit to the resonance dip (in linear scale) has been performed. The results are shown in Table 5.2. From theses results, it is possible to calculate an attenuation constant α according to equation (2.163). For the center frequency x_c of the resonance dip, $\beta \approx 190$/m can be calculated numerically with the formulas presented in section 2.4.2. α then follows as $\approx$ 4.3/m = 37.3 dB/m.

This big value for the attenuation constant has to be regarded as the overall attenuation of the DUT. The attenuation of the superconducting CWG itself should be negligible small in comparison to the overall attenuation according to CWG theory. Taking the length of the sample holder ($\approx$ 2 cm) one ends up with an attenuation of -0.75 dB for the DUT. This corresponds to the offset of the Lorentz fit (y_0 [dB] = $20 \cdot \log(0.9) = -0.9$dB). This seems to be consistent. However, the results of these estimations should be taken with care, as they originate from the assumption that the DUT is a resonator. This assumption is not completely correct, as the DUT should rather be a good transmission line. For this reason, error bars are not given explicitly. Moreover, one has to take into account that all the values given here are at the resolution limit of the measurement setup as estimated conservatively in the previous section.

The origin for the resonance dip is parasitic capacitances and inductances at the V-Connectors. These are due to the imperfect galvanic contact between the coplanar structure and the stress reliefs of the V-Connectors, and due to the bonding wires, respectively.

To confirm this assumption, the bonding wires and stress reliefs were removed and substituted by silver glue. The results of the measurements with silver glue are shown in Figures 5.6(b) and 5.7(a). Here, the resonance dip vanishes. Moreover, one can see that the transmission is significantly better in the case of silver glue connections for frequencies above 14 GHz.

Area A	Center x_c	Width w	Offset y_0	Quality factor $Q = x_c/w$
-1.8·10^8 Hz	4.0·10^9 Hz	1.8·10^8 Hz	0.9	22

Table 5.2: Results of the Lorentz fit for the resonance dip in Figure 5.6(a). The fitting function: $y = y_0 + (2A/\pi) \cdot w/(4(x - x_c)^2 + w^2)$.

5.3.2 Time Domain Measurement

It is possible to perform a Fourier transformation of the S-parameters from frequency domain into time domain. This is called a time domain measurement. The NVA is able to do this transformation via a FFT algorithm. In Figure 5.7(b), one can see the results of the time domain measurement of the (uncalibrated) S_{11}-parameter for the *bonded* structure. The blue curve shows the data for $T = 10$ K, whereas the green curve shows the measurement for the superconducting case. Δ is the difference of S_{11} at 10 and 4 K (additionally, adjacent averaging over 10 measurement points (equivalent to $\approx$ 0.44 ns) was performed on Δ). The olive curves are linear fits to curve Δ. Peaks in a time domain measurement represent reflections in the measurement circuitry due to impedance mismatches. If one knows the velocity of the signal in the microwave circuit, one can determine the relative position of these mismatches in the line by a time domain measurement. This is the reason why time domain measurements are often used to find imperfections in telecommunication lines.

Assuming the DUT as a sort of damped resonator, this measurement can be interpreted as follows: The measured difference Δ of the curves above and below T_c can be modeled as the difference of two exponentially decaying curves (y_1 for $T < T_c$ and y_2 for $T > T_c$), that a are given by:

$$y_1[dB] = 20\log e^{-(\alpha_1+\alpha_c)ct} \approx -8.7(\alpha_1 + \alpha_c)l \tag{5.1}$$

$$y_2[dB] = 20\log e^{-(\alpha_1+\alpha_n)ct} \approx -8.7(\alpha_1 + \alpha_n)l \tag{5.2}$$

where α_1 accounts for a decay of the wave along the way $l = ct'$ (see Figure 5.7(b)) due to effects that are present in the superconducting and non-superconducting case (e.g. capacitances that couple the DUT to the environment, like the parasitic capacitances between the coplanar structure and the stress reliefs). c is the signal velocity on the line (dispersion is neglected) and t' the measurement time. α_n is the attenuation due to the normal conducting Nb, whereas α_c is the attenuation due to the superconducting Nb. To model Δ correctly, also an offset y_0 (see Figure 5.7(b)) has to be introduced. y_0 gives the height of the initial signal above the noise floor (NF, in the measurement ≈ -100 dB) of the measurement setup.

Signals below NF cannot be detected by the system any more:

$$y_1\,[dB] = \left\{ \begin{array}{c} -8.7(\alpha_1 + \alpha_c)ct'\,[dB] \quad \text{for} \quad 0 < t' < t_1 \\ -y_0\,[dB] \quad \text{for} \quad t_1 < t' \end{array} \right\} \tag{5.3}$$

$$y_2\,[dB] = \left\{ \begin{array}{c} -8.7(\alpha_1 + \alpha_n)ct'\,[dB] \quad \text{for} \quad 0 < t' < t_2 \\ -y_0\,[dB] \quad \text{for} \quad t_2 < t' \end{array} \right\} \tag{5.4}$$

where t_1 and t_2 are the times when the respective signal falls below the noise floor. As the attenuation is much bigger in the normal conducting case $t_1 > t_2$.
Δ is then

$$\Delta\,[dB] = \left\{ \begin{array}{c} 8.7(\alpha_n - \alpha_c)ct'\,[dB] \quad \text{for} \quad 0 < t' < t_2 \\ y_0 - 8.7(\alpha_1 + \alpha_c)ct\,[dB] \quad \text{for} \quad t_2 < t' < t_1 \\ 0\,[dB] \quad \text{for} \quad t_1 < t' \end{array} \right\} \tag{5.5}$$

$$\tag{5.6}$$

As $\alpha_n \gg \alpha_c$, Δ increases until $t = t_2$. Then Δ decreases with an attenuation of $\alpha_1 + \alpha_c$, where $\alpha_1 \gg \alpha_c$. Separate linear fits of the rising and falling part of Δ give the slopes $m_1/$ [dB/s] and m_2 [dB/s]. Together with the estimated y_0, t_1, t_2 and c, an over-determined set of 4 linear equations with the three unknowns α_1, α_n and α_c is obtained.
Practically, the accuracy of the linear fit to Δ is bad. Therefore, none of the needed parameters may be determined accurately. In addition, α_c is so much smaller than α_1 and α_n, that it would not play any role in the set of linear equations. All this means, that α_1 and α_n can be estimated only very roughly. The errors are obviously so big, that an error consideration will not be done here. Moreover, this procedure can not at all be used for the determination of α_c. To do this accurately, one can measure a resonator with very small coupling capacitances as already mentioned in section 2.5.1. In the above given model, such a resonator could be described with $\alpha_1 \to 0$, allowing for a determination of α_c in the time $t_2 < t < t_1$.
Assuming $c = 1.3 \cdot 10^8$ m/s, one gets from the slopes of the linear fits (see olive curves in Figure 5.7(b)): $m_1/c \approx \alpha_n \approx 0.52$ dB/cm and $-m_2/c \approx \alpha_1 \approx 0.09$ dB/m. Unfortunately, α_n is much too low to explain the low S_{12}-parameters of M1 in the normal conducting case. α_1 at least is small enough to not contradict the S_{12}-measurement of M1 in the superconducting case.

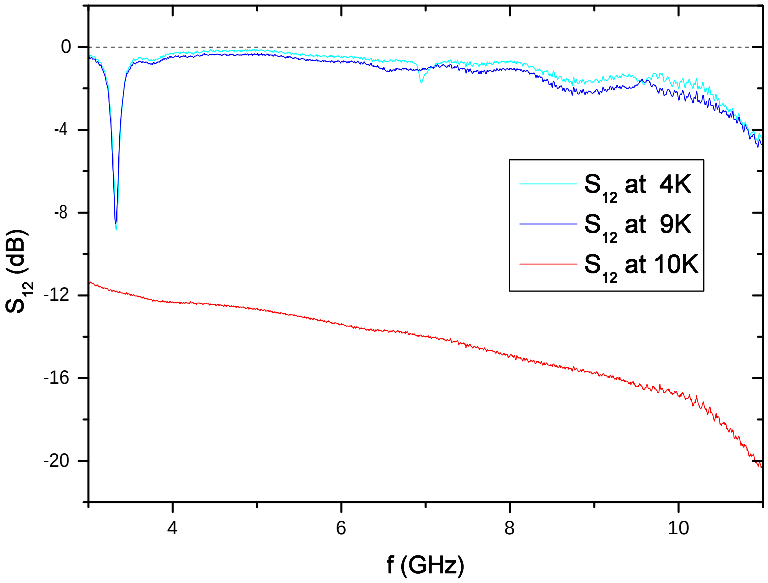

(a) Bonding wires were used here to contact the structure as seen in Figures 4.7(a) to 4.7(c). The data at 9 and 4 K do not differ much, whereas the transition to the non-superconducting state between 9 and 10 K strongly increases the attenuation extremely from around -1 dB to ¡ -10 dB for frequencies above 2 GHz.

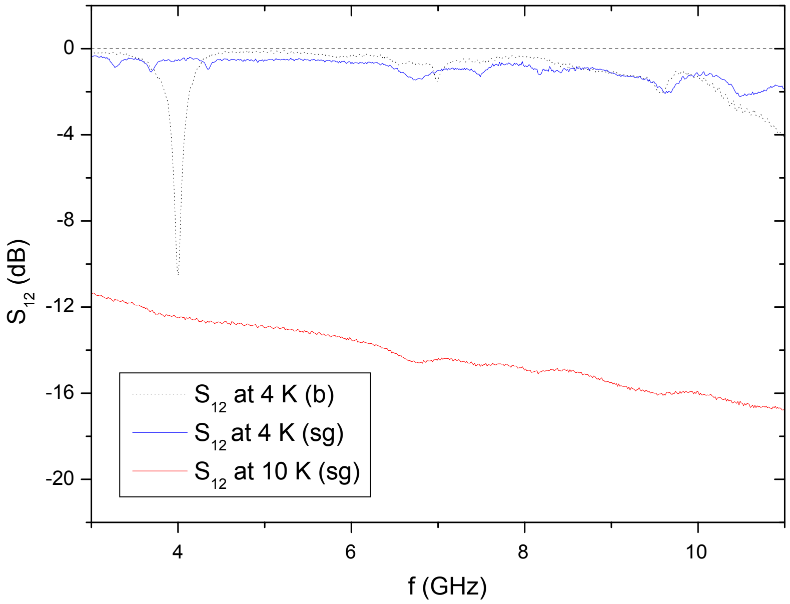

(b) Red and blue solid curves: Silver glue (sg) was used to contact the structure as seen in Figures 4.7(e) and 4.7(f). Above T_c, there is not much difference to Figure 5.6(a) (red curves). Below T_c however, the resonance dip (dotted line, from 5.6(a)) disappears completely.

Figure 5.6: S_{12} parameters of the meander structure M1 connected to the outer world by bonding wires (b) and silver glue (sg) (see Figure 4.7).

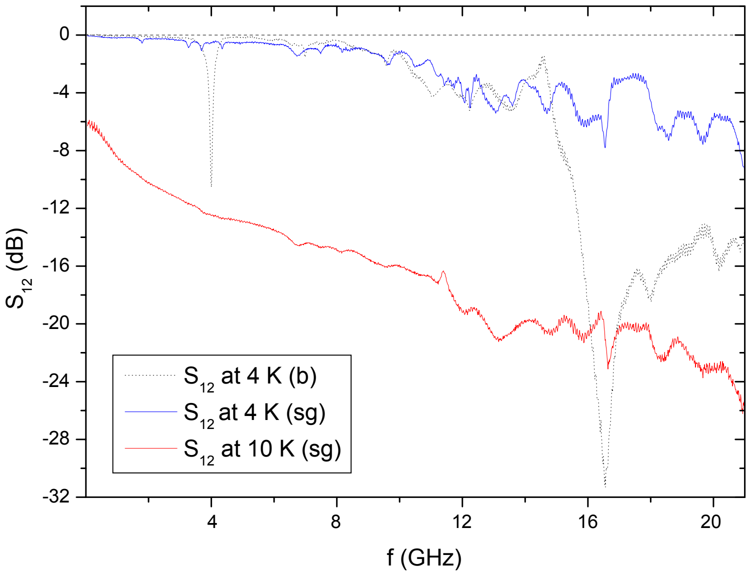

(a) Same as Figure 5.6(b), the frequency was swept from 50 MHz to 21 GHz. The dotted curve is from 5.6(a). In addition to the resonance dip at around 4 GHz, the transmission of the bonded structure is getting significantly worse for frequencies above 14 GHz.

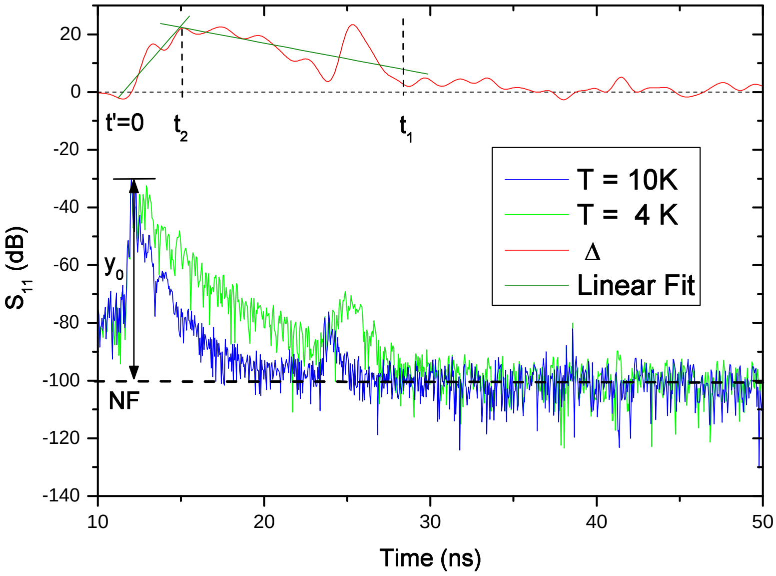

(b) S_{11} time domain measurement. Δ is the difference of S_{11} at 10 and 4 K (additionally, adjacent averaging over 10 measurement points ($\simeq$ 0.44 ns) was performed on Δ). The green curve is a linear fit to Δ.

Figure 5.7: (a) shows the S_{12} parameters of the meander structure M1 when connected to the outer world by bonding wires (b) and silver glue (sg) (see Figure 4.7). (b) shows a S_{11} time domain measurement of the bonded M1 structure.

5.4 Measurement of Hybrid Ring Structures H2, H3 and H4

In this section, the measurement results for the hybrid rings are presented. All measurements are compared with the transmission line theory developed in section 2.3. This comparison is performed by fitting the theoretical S_{13}-function to the measured curves. The S_{13}-parameter is chosen as it allows most accurate fitting because of the characteristic peak with highest isolation. All other theoretical S-parameter curves were then calculated with the fit parameters derived by fitting the S_{13} data. In all plots, the fitted S_{13}-function is plotted as dotted line for better illustration of the center frequency of the hybid ring, the latter being marked by a vertical dashed line.

5.4.1 Results from the Fitting Procedure

As the transmission line theory from section 2.3 assumed no losses, losses have to be "introduced" now in the theoretical S-parameter functions. The most simple way to do this, is using the low loss transmission line theory introduced in section 2.2.6.2. According to this theory, the losses can be modeled by the following substitution for the frequency f:

$$f \rightarrow f - i\alpha_f. \tag{5.7}$$

According to the relation $\beta = f\frac{2\pi}{c}\sqrt{\varepsilon_{eff}}$, α_f is related to the attenuation constant appearing in the low loss transmission line theory:

$$\alpha = \alpha_f \frac{2\pi}{c}\sqrt{\varepsilon_{\text{eff}}}. \tag{5.8}$$

α_f will serve as one fit parameter, making it possible to calculate α for known ε_{eff}.
The other fit parameter will be the frequency of maximum isolation (denoted as center frequency f_0 in the following). The center frequency f_0 is related to $\sqrt{\varepsilon_{\text{eff}}}$ by

$$f_0 \frac{2\pi}{c}\sqrt{\varepsilon_{eff}} = \frac{3}{2R}, \tag{5.9}$$

where R is the radius of the ring which is well known from the fabrication process. If f_0 is known from the fit to the experimental data, ε_{eff} can be calculated. This finally allows to determine ε_r (an isotropic substrate assumed) via equation (2.4.2).
For the hybrid rings, the fits were done using the MATLAB[3] function `nlinfit` which performs nonlinear least-square data fitting based on the Gauss-Newton method. The best fits were achieved, taking into account only data below 14 GHz, since above 14 GHz, the attenuation is muc stronger, as already observed for M1 (the reason for this is most likely an imperfect galvanic connection between the structure and the V-connectors). Nevertheless, the fitting errors given by `nlinfit` for the center frequency f_0 and α seem to be very big.

---

[3] The MathWorks, Inc., Version 6, http://www.matlab.com/ (2006)

The reason for this is that the function calculates the overall error by averaging over the deviation of the fitted curve from the data over the *whole* frequency range. This results in a large error ($\approx$ 1 GHz for f_0 and $\approx 10 \cdot 10^6$ /m), although the fitted function seems to be a perfect envelope of the measurement data, especially around the most important region, the center frequency f_0.
Unlike the data of S_{13} of H2 and H4, H3 has a measured S_{13}-parameter that is not superposed by a resonance dip at the center frequency (see Figures 5.8(a), 5.12(a), 5.15(a), 5.12(a) and 5.12(a)). As one can see in Figure 5.8(a), the fit for S_{13} is very good for H3. Due to the sharp isolation peak, the determination of the center frequency is possible to a very high accuracy. Although no error can be given from the `nlinfit` function, it is reasonable to assume an error for the fit of S_{13} of H3 that is based on in the resolution of the frequency sweep of the NVA. The frequency sweep was performed linearly between 50 MHz and 21 GHz with a step size of 13 MHz. Thus a conservative error estimate of ±20 MHz for f_0 seems reasonable.
Varying the fitting curve manually gives a reasonable error estimate of α of approximately $\pm 3 \cdot 10^6$/m. The accuracy of the S_{13}-measurement on H3 is the reason why the results from the fit of H3 are taken to calculate ε_r and α.
The error of the fit of S_{13} of H2 is larger than for H3. Manual variation of the fitting curve gives an error estimate of ±400 MHz for f_0. For α_f however, it is not possible to give a reasonable error estimate. The S_{13} data of H2 can be reasonably reproduced by α_f-values in the range from 1 to $50 \cdot 10^6$/m. The reason for this is the absence of the isolation maximum.
For H4, it does not make sense to perform a fit procedure as the measurement data differs too much from the theoretical curve. In the plots of the S-parameters of H4, the fitting curves of H3 are given as a guide for the eyes.
All relevant fitting parameters as well as ε_r and α which were deduced from the fit parameters of H3 are shown in Table 5.3. The errors for the derived values were calculated by Gaussian error propagation.
The value for ε_r is very realistic and should be taken for future designs of CWG structures on sapphire at temperatures around 4.2 K. α is definitely too big to be due to attenuation of the superconducting CWG transmission line itself as shown in section 2.5.1. This means that α cannot be interpreted within the framework of transmission line theory only (see section 2.3). This is clear as the transmission line theory does not account for the influence of e.g. any CWG discontinuities, connectors, sample holder, crosstalk between the CWG lines etc. There are many reasons that could add up resulting in an elevated α. Some of these reasons are discussed in the following section.

5.4.2 Discussion of the Measurement Results

In principle, transmission line theory and experiment are in good agreement. Despite numerous resonance peaks, theory always constitutes a good envelope for the measured data. This is especially the case for the measurements of hybrid ring H3. The performance of the hybrid rings seems to be reduced by a big resonance peak (denoted as center peak in the following) present in all measurements very close ($\approx$ 100 - 200 MHz) to or exactly at

Structure	f_0 (GHz)	α_f (1/m)	$\sqrt{\varepsilon_{eff}}$	ε_r	α (dB/m)
H3	7.58 ± 0.02	$(26 \pm 3)\cdot 10^6$	2.469 ± 0.007	10.9 ± 0.7	2.6 ± 1.0
H2	7.6 ± 0.4	$26 \cdot 10^6$	–	–	–

Table 5.3: Results of the fits of H2 and H3 for 4 K, as well as the deduced values for $\sqrt{\varepsilon_{eff}}$, ε_r and α. The geometrical data of H3 are taken from Table 5.1.

the center frequency (see Figures 5.8(a) to 5.14). A peak in S_{13} is always accompanied by peaks in the other S-parameters at the same position, see e.g. 5.8(a) and 5.9(a) for H3, or 5.12(a) and 5.13(a). In some sense this agrees with the unitarity of the S matrix. The center peak makes precise analysis and interpretation of the measurement data and the ring performance very difficult and speculative.

For example, H3 is the hybrid ring where the ratio of Z_1/Z_c meets the requirements of transmission line theory best. However, the question whether this is the reason for its better performance in comparison to H2 and H4 can not be judged from the data. Transmission line theory predicts only a negligible influence of this ratio on the hybrid ring performance, whereas numerical simulations were quite sensitive to this ratio.

Moreover, the origin of the center peak itself is not clear yet. As the envelope of the S-parameters agree pretty well with theory, it is not very probable that the peak is a feature of the hybrid rings. It is more realistic, that the environment is responsible for it. Some hints are given in the following:

Resonances within the box are *very* probable candidates for such an environmental influence. Assuming a wave velocity of $c = 2 \cdot 10^8$ m/s and the typical center frequency of 7.6 GHz, one gets a wavelength of 2.6 cm, which corresponds well to the dimensions inside the sample holder of $20.4 \times 15 \times 5$ mm. This assumption is supported by the measurement shown in Figure 5.11. These resonances could then couple e.g. ports 1 and 3 and thus reduce the isolation. In the case of sample holder resonances, even the investigation of the line-to-line coupling by G. Ghione [27] presented in 2.4.2 would lose its validity.

Another reason could be an imperfect contact between the coplanar structure and the V-connectors. This is demonstrated by the measurement shown in Figure 5.15. To avoid silver glue connections, which are pretty hard to establish, the structure was pressed againt the connectors using a small screw in the back part of the sample holder. Instead, it was tried to press the structure against the connectors using a small screw in the bottom part of the sample holder. The absence of sufficient galvanic contact between connectors and hybrid ring is responsible for a drastic decrease of the performance. This is strongly supported by the strongly enhanced attenuation at low frequencies. In principle, better measurements could be performed with a probing station [4] as is presently being set up at the WMI for measurements at cryogenic temperatures down to and even below 4.2 K. Nevertheless, experience with the structures installed *inside* a compact sample holder is indispensable, as in later experiments in circuit CQED, one will be confronted with limited access and

---

[4] see e.g. BSW TestSystems & Consulting AG, http://www.testfixture.de/ (2006)

space in a millikelvin cryostat. A good message however is the fact that the S-parameter measurements were reproducible to a great extent when silver glue was used to establish the connections to the V-connectors. Unfortunately a comparative measurement of H4 with silver glue was not performed because of a lack of time.

It was also tried to improve the performance of the hybrid rings making use of so called airbridges at the T-junctions of the hybrid arms as proposed in reference [19] (see also section 3.3). An illustration of airbridges as they were used in this work is shown in Figure 4.8(d). The airbridges have been made with bonding wires with a diameter of approximately 3 - 4 times the gap distance G of the CWG structures. Such airbridges are typically positioned a CWG T-junctions to suppress parasitic coupled slot line modes as they can result in excess insertion and return loss. Moreover, within the hybrid, they contribute to an unwanted crosstalk of ports that ought to be isolated.

The measurement data performed with installed airbridges on hybrid rings H3 and H2 are shown in Figures 5.10 and 5.14, respectively. In the case of H3, this leads to a dramatic decrease of the performance. This could be explained by the phase shift that can be provoked by an airbridge in the context of waveguide discontinuities [19] which would in turn change the interference conditions at the ports of the ring and finally reduce the isolation and transmission properties. In the case of H2, this is less distinctive. S_{12} on the other hand even shows an improved performance, having less pronounced resonance peaks. The simulations with Microwave Studio in section 3.3 did not show a negative influence of airbridges on the performance of the hybrid ring as well. Nevertheless, these measurements show rather that airbridges made out of bonding wires are not a good choice to efficiently ameliorate the characteristics of the hybrid rings.

A comparison of the S_{13}-parameters of H2 and H3 above T_c with the ones below T_c as shown in Figures 5.8(b) and 5.12(b) shows the drastic influence of the superconductivity. Above T_c, the measured S-parameters follow the theoretical curves with an offset of more than 5 dB far away from the center frequency. The isolation maximum is much less pronounced but clearly visible. Nevertheless, the curves above T_c cannot be fitted very accurately with the fitting procedure described in 5.4.1. The procedure gives as an estimate $\alpha_f = 25 \cdot 10^8/\mathrm{m}$. The fit is especially bad for lower frequencies as there, the low loss transmission line approximation entering the fit functions is not valid any more. Very good conductivity or even superconductivity is a key ingredient for a high performance hybrid ring.

Finally, a very speculative explanation for the origin of the center peak is the flux quantization inside the superconducting ring. A presentation and discussion of the most important aspects of this problematic is given in Appendix A. Summarizing, one can say that the influence of the fluxoid quantization on the operability of the hybrid cannot be excluded up to now. It would be advisable to repeat the measurements with non-superconducting material like e.g. gold.

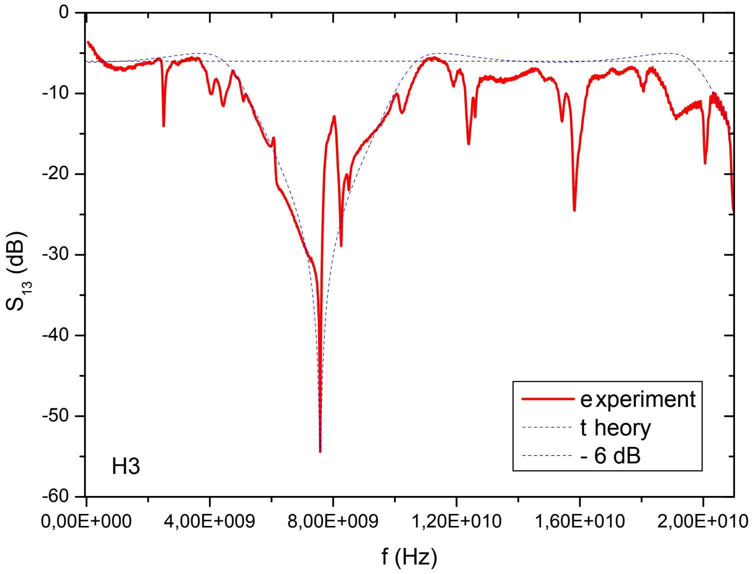

(a) S_{13} at 4 K.

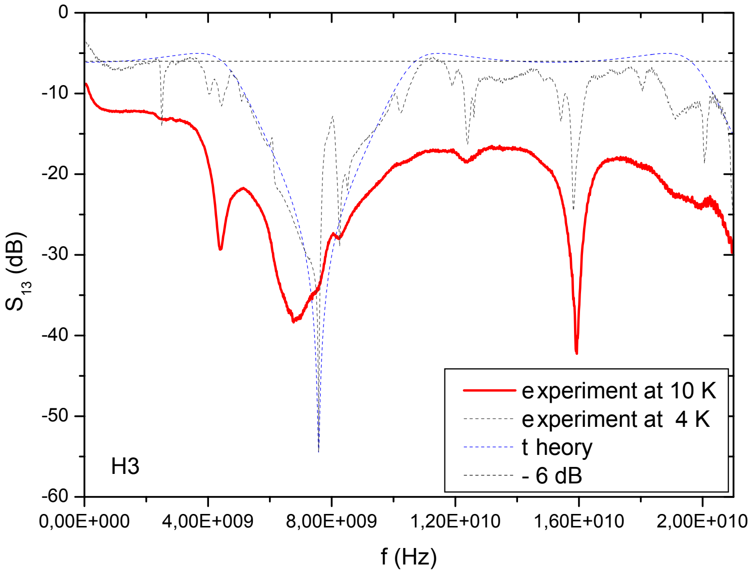

(b) S_{13} at 4 and 10 K.

Figure 5.8: S_{13}-parameters of hybrid ring H3 at above and below T_c.

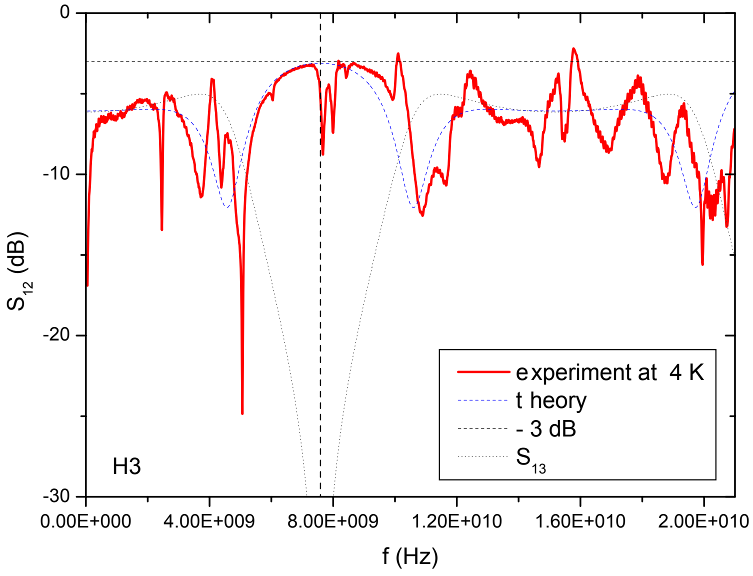

(a) S_{12} at 4 K .

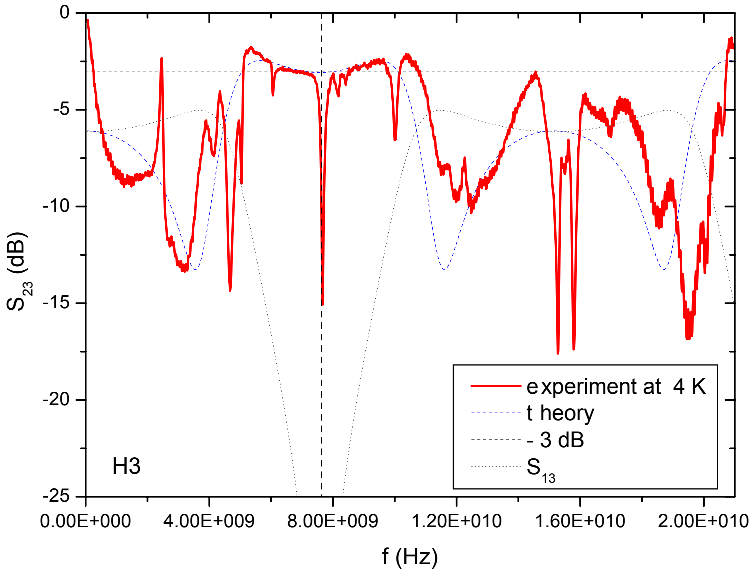

(b) S_{23} at 4 K .

Figure 5.9: S_{12} and S_{23}-parameters of hybrid ring H3.

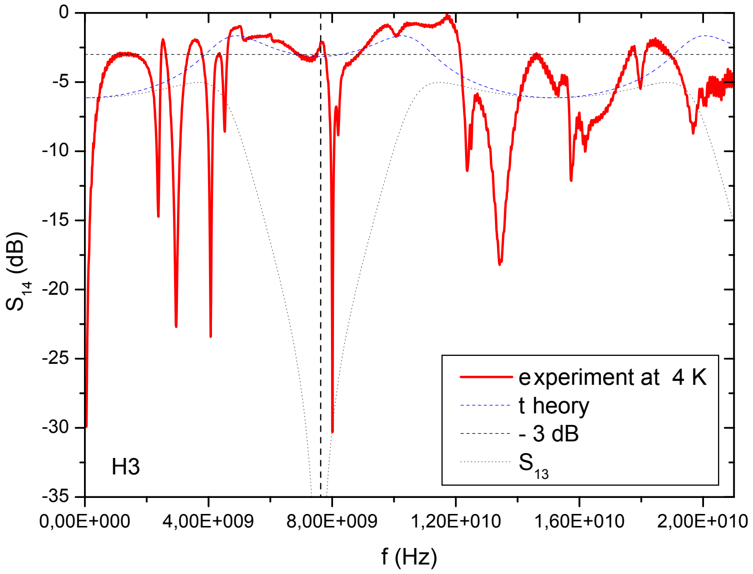

(a) S_{14} at 4 K.

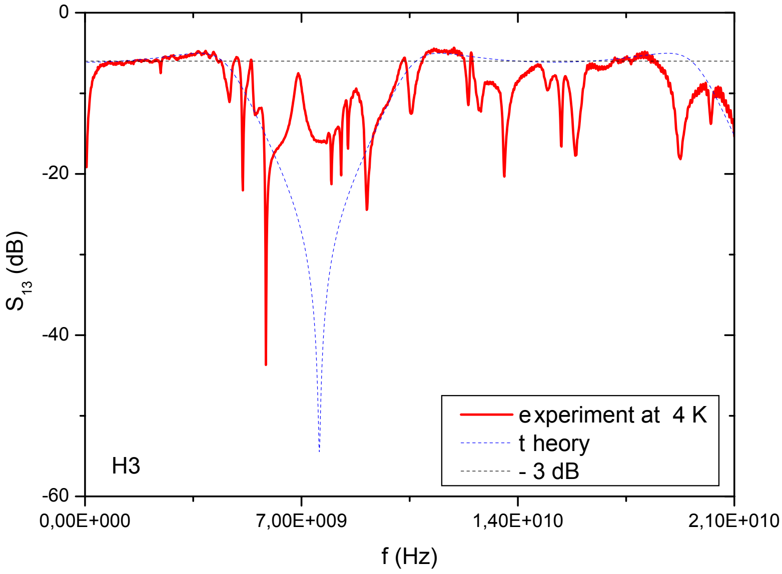

(b) S_{13} at 4 K with bonded airbridges at the T-junctions of the hybrid ring. This measurement was performed to investigate the influence of airbridges.

Figure 5.10: S_{14} and S_{13}-parameters of hybrid ring H3.

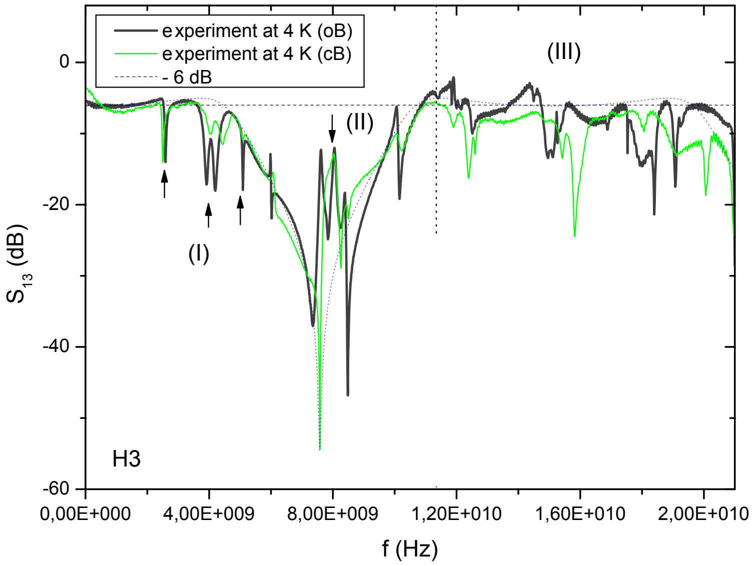

(a) S_{13} at 4 K.

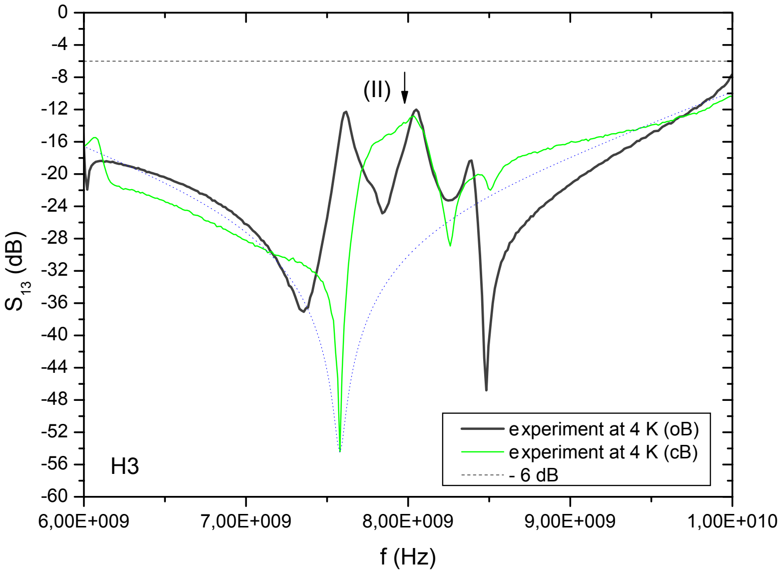

(b) S_{13} at 4 K. Enlarged view of Figure (a).

Figure 5.11: $S13$-measurement of H3 performed with open (oB) and closed (cB) sample holder. This measurement shows that environmental influences play a significant role.

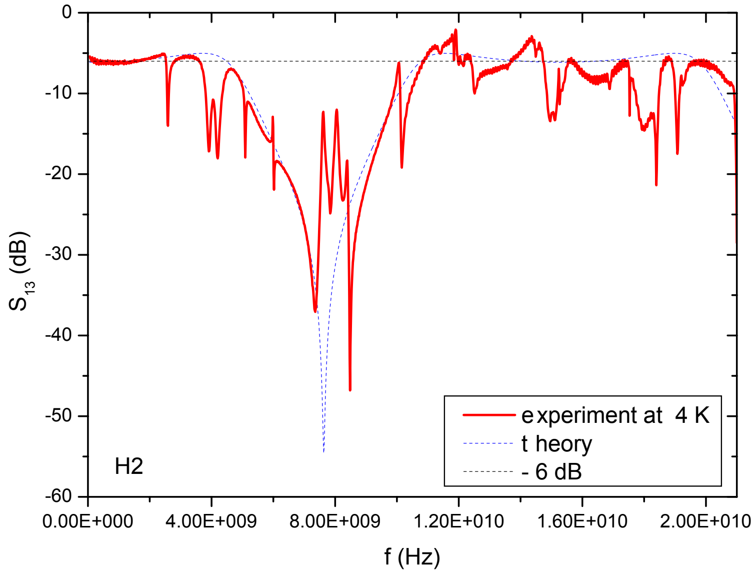

(a) S_{13} at 4 K.

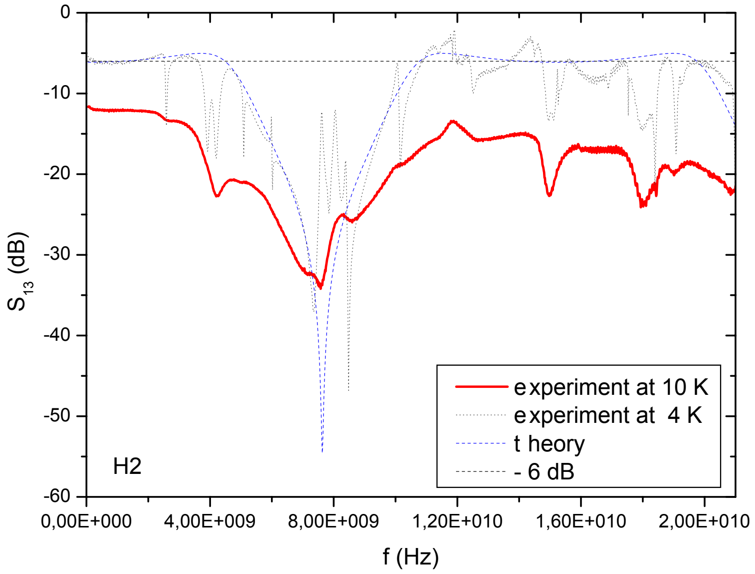

(b) S_{13} at 4 and 10 K.

Figure 5.12: S_{13}-parameters of hybrid ring H2 at above and below T_c.

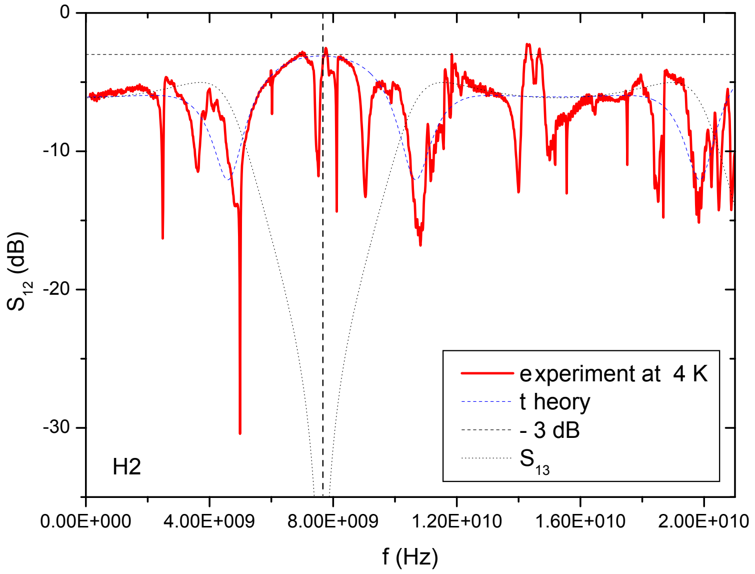

(a) S_{12} at 4 K .

Figure 5.13: S_{12}-parameter of hybrid ring H2.

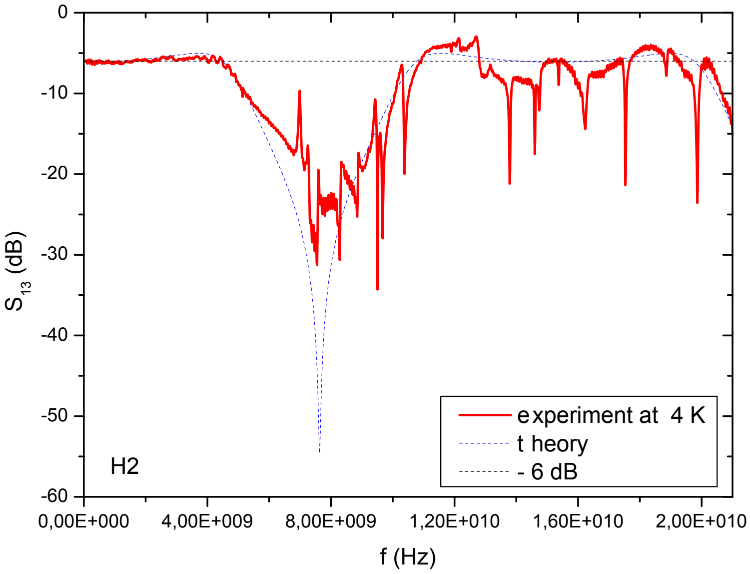

(a) S_{13} at 4 K with bonded airbridges at the T-junctions of the hybrid ring.

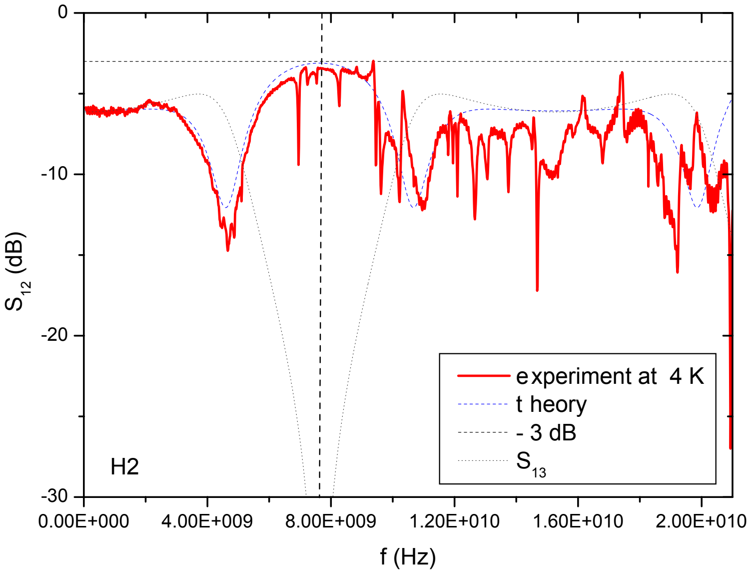

(b) S_{12} at 4 K with bonded airbridges at the T-junctions of the hybrid ring.

Figure 5.14: S-parameter measurements that were performed with hybrid ring H2 to inverstigate the influence of airbridges.

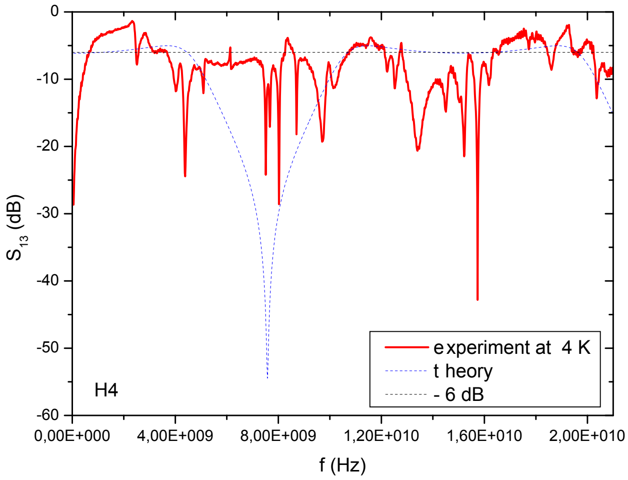

(a) S_{13} at 4 K.

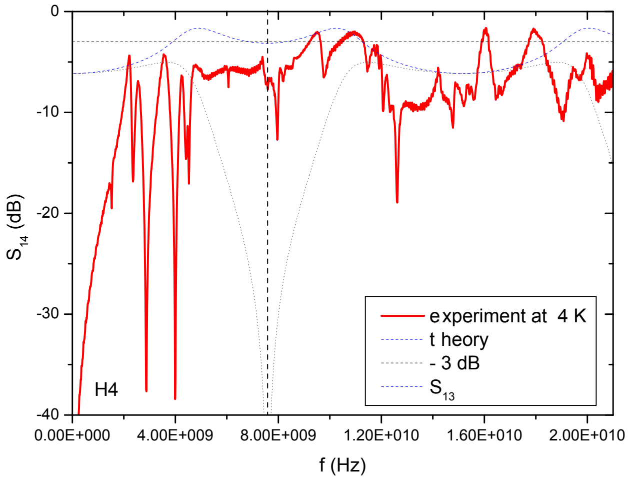

(b) S_{14} at 4 and 10 K.

Figure 5.15: S-parameters of hybrid ring H4 without silver glue. Instead, it was tried to press the structure against the connectors using a small screw in the bottom part of the sample holder. The absence of sufficient galvanic contact between connectors and hybrid ring are responsible for the drastic decrease of performance.

5.5 Outlook

To allow for a more profound analysis of the above mentioned aspects, additional measurements on new hybrid structures will be necessary. Thereby, one should favor the measurements over additional exhausting numerical and theoretical studies, as now all fabrication steps (theory, simulation, design, fabrication and measurement) have been established, making it possible to quickly produce samples on demand. In principle, it takes not more than one day, to fabricate a sample and it is advisable to produce several samples in parallel. The only bottle neck here is the limited capacity and the long time for evacuating the load-lock for the sputter chamber. As already mentioned, structures should be fabricated in gold and niobium. Moreover, one should also investigate silicon-substrates, as they will be important as soon as a Qubit will come into play. A Qubit cannot be fabricated directly on sapphire via E-beam lithography, as sapphire is electrically isolating.

New masks should include especially a set of structures with different center frequencies. This will allow to distinguish - in an effective and accurate way - between the influences coming from the hybrid ring itself and from the environment. Peaks and dips caused by the environment should be unaffected by a change of the center frequency in first order approximation. The hope is, that this could illuminate especially the origin of the most disturbing center peak. The sweep over the center frequencies can be performed most easily by changing the radius of the ring, making it possible to re-use the sample holder and the substrates. Moreover, by changing the radius of the ring, the length of the arms will be changed, allowing the investigation of the influence of this parameter on the performance of the device. A possible influence was recently pointed out by numerical simulations done by the group of Prof. Lugli at the Institute for Nanoelectronics at the TUM [60].

It is advisable to fabricate resonator structures together with the actual structures of interest, as resonators allow for an accurate determination of all relevant transmission line properties.

Chapter 6

Conclusion

This thesis was motivated by the idea to set up a *microwave quantum homodyning* detection scheme in which a superconducting hybrid ring acts as an on-chip microwave beam splitter. The hybrid ring thus constitutes a central building block in the detection scheme for weak quantum signals [61]. Experiments like the one proposed in the introduction, where a quantum object interacts with the quantized modes of a resonator fall into the class of cavity quantum electrodynamics (CQED) experiments. If such experiments are realized in superconducting circuits, they belong to the subgroup of circuit CQED experiments.

In this work, a superconducting coplanar wave guide (CWG) realization of such a hybrid ring for frequencies up to 10 GHz has been investigated to a great extent. The hybrid ring was realized in a CWG design for allowing an easy and reflection-less coplanar integration of this ring in up-to-date CQED circuitry [50].

Starting from basic electrodynamics, the transmission line theory has been introduced with which it was possible to model the hybrid ring analytically.

As transmission line theory is independent of the concrete realization of a transmission line, transmission line theory was followed by a thorough investigation of superconducting CWGs. Basic considerations of the relevant timescales showed that the dimensions of the CWGs fabricated within this work allow a treatment within the framework of quasi-static approximations up to 50 GHz. Below this frequency, the superconducting CWG may be regarded as dispersion free. This results in a minimal pulse duration of approximately 20 ps, which is sufficient for present experiments with superconducting quantum devices.

Accurate expressions for the relevant transmission line properties were given. These are the propagation constant (or wave vector) and the attenuation constant. The knowledge of the propagation constant is important to predict the working point of the hybrid ring, i.e. the center frequency around which the hybrid ring may be used as microwave beam splitter. Due to the extremely low attenuation within the superconducting CWGs, transmission line theory predicts very good transmission and isolation properties of the hybrid ring - key features for its use as a beam splitter.

The hybrid ring has been simulated with commercially available Software: Microwave Office 2002© [51] and CST Microwave Studio© [52]. Thereby, perfectly conducting materials were assumed, as superconductivity is not included in the software.

The results using the first simulation program agree very well with the predictions made by the analytical transmission line theory in a reasonable amount of time. This is not striking as the software models the hybrid ring also in transmission line theory. The big advantage of this software is, however, that it also accounts for the effects of the T-junction discontinuities in a hybrid ring. This allows a slightly more accurate modelling of the structures.

The second software simulates the complete volume of the hybrid ring. Theoretically, this is more precise, as it should also account for any kind of direct crosstalk of the different hybrid ports due to e.g. box resonances. Unfortunately, this approach is computationally too expensive to deliver accurate results in a reasonable time. This program should rather be used for problems involving only small sections of the hybrid ring, especially where discontinuities in the wave propagation are expected, e.g. at T-junctions or V-connectors.

Hybrid rings have been designed according to the design guidelines presented in this work, to correspond best to the results from analytical and numerical analysis.

Two fabrication processes for the samples have been optimized. One process uses reactive ion etching (RIE), the other one is based on a lift-off process as a final step. It turns out that the process using RIE is best suited for the fabrication of Nb samples on sapphire as this process is not affected by the transparency of the sapphire substrates. The process parameters allow a very reliable sample fabrication.

Finally, S-parameter measurements have been performed with an ordinary meander-like CWG transmission line (M1) and several hybrid rings down to a temperature of 4.2 K using a simple response-calibration technique.

For M1, also a time domain measurement has been presented. The measurement of M1 allowed to test two different strategies for the galvanic connection of the coplanar samples to the measurement circuitry: Firstly via bonding wires and secondly via silver glue. Although the connections via bonding wires are much easier to elaborate, it turns out that the silver glue connections have much better microwave properties. They should be used in future applications.

The measurement data of the hybrids show, that transmission line theory and experiment are in good agreement: With only *two independent* fitting parameters (attenuation α and frequency of maximal isolation f_0), it is possible to fit the data such that the resulting fitting curve is a very good envelope for the measured data. The fitting data allowed to determine the relative dielectric constant of sapphire at 4.2 K. The knowledge of this constant is important as from now on, f_0 can be predicted by transmission line and CWG theory and thus will not be a fitting parameter any more. However, the absolute value for the α parameter - resulting from the fitting routine - can not be understood by transmission line and CWG theory alone. Thus, it has been taken as a fit parameter that accounts for the manifold effects that can reduce the performance of the hybrid ring.

The performance of the hybrid rings seems to be reduced by a big resonance peak around f_0 whose exact origin is unclear up to know. This has to be subject of further investigations as recommended in the outlook in the previous section. All necessary fabrication steps (theory, simulation, design, fabrication and measurement) for further experiments have been established within this diploma thesis.

Despite the problems that are still present, it seems to be possible to design a hybrid ring that meets the requirements for the use as microwave beam splitter in circuit QED as proposed in the introduction. According to the fits, the following benchmarks seem reasonable:

center frequency	bandwidth	transmission	isolation
0 - 8 GHz	300 MHz	> -3.5 dB	< -40 dB

Appendix A

Fluxoid Quantization in the Hybrid Ring

A very important property of superconductivity is the fluxoid or flux quantization in multiply connected superconductors as shown experimentally in 1961 [62, 63]. The total flux threading a superconducting closed ring has to be a multiple of the flux quantum $\Phi_0 = \frac{h}{2e}$

$$\oint_C \Lambda \vec{I_s} \cdot d\vec{l} + \int_S \vec{B} \cdot d\vec{s} = n \cdot \Phi_0, \tag{A.1}$$

where C is a closed contour, S the surface defined by the contour C, $d\vec{l}$ is an infinitesimal length of line in the contour C, and $\vec{I_s}$ is the supercurrent. $\vec{B}$ is the magnetic flux and $d\vec{s}$ is normal to the surface S quantifying an infinitesimal area. n is a natural number and Φ_0 the so called flux quantum. Λ is the London coefficient [1]. This fluxoid quantization may eventually affect the operability of the hybrid ring close to the operating frequency.

Regarding the hybrid ring as an inductance L_{Ring} (see Figure A.1(a)), a lumped element representation of the ring within the two-fluid model can be given as shown in Figure A.1(b). This circuit is adequately approximated by the circuit shown in Figure A.1(c) which is comparable to Figure 2.3. The results for a typical hybrid ring fabricated within this work for T = 4.2 K are shown in Table A.1[1].

Fluxoid quantization has to be taken into account, whenever supercurrents are dominant. In the two-fluid model, this is the case when $\omega \ll 1/\tau_{chan}$ (2.62). Here, only the inductances due to the inertia of the electrons and Cooper pairs where taken into account. In the case of superconducting circuits however, a "geometrical" inductance depending on the geometry of the circuit lines arises. This additional inductance can lower the characteristic frequency above which normal conducting electrons dominate. This calculated characteristic frequency for the hybrids within this work is $1/\tau_{LR}$ = 1.4 GHz which is in close to the operating frequency of the hybrids. Therefore, an influence of the fluxoid quantization on

---

[1] $R_n = \rho \frac{l}{A} = \frac{2\pi r}{W t \tilde{\sigma_0}(T=4.2K)}$ resistance of the ring's normal conducting channel, W = 200 μm width of the ring, t = 100 nm thickness of the metal layer forming the ring, r = 3.8 mm radius of the ring, $\tilde{\sigma_0}(T = 4.2\text{K})$ specific conductivity of normal conducting channel of Nb at 4.2 K $\tilde{\sigma_0}(T = 4.2K) = \tilde{\sigma_0}(T_c = 9.2K)\left(\frac{T}{T_c}\right)^4$ with $\tilde{\sigma_0}(T_c = 9.2K) = 1.4 \cdot 10^9\ 1/(\Omega m)$ (2.1) $L_{Ring} \approx N^2 r \mu_0 \mu_r [\ln(8r/W) - 2.0]$ inductance of the ring, where $N = 1, \mu_r = 1$
(see http://emcsun.ece.umr.edu/new-induct/circular.html, Jan. 2006)

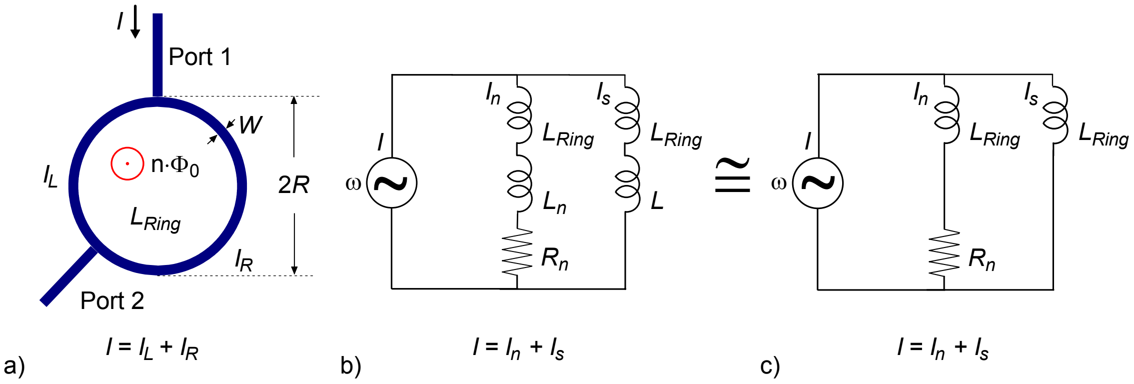

Figure A.1: (a) The hybrid ring modelled as a two-port element: a superconducting ring (radius R and width W) with asymmetrically connected ports 1 and 3. The ring has a self-inductance L_{Ring} and is threaded by the flux $\Phi = n \cdot \Phi_0$. The total current I through the lines is split into a left-circulating current I_L and a right-circulating current I_R. (b) Lumped element representation of the hybrid ring in the two-fluid model. The ring is modelled as an additional serial inductance L_{Ring} in the normal channel (transporting current I_n) and in the superchannel (transporting current I_s). As the inductances due to the inertia of the normal electrons and Cooper pairs (L_n and L_s, respectively) are negligible in the frequency regime under consideration in comparison to the large self-inductance L_{Ring}, the reduced lumped element representation shown in (c) is a good approximation.

R_n	L_{Ring}	$1/\tau_{LR}$
20 Ω	14 nH	1.4 GHz

Table A.1: Calculated values for the characteristic frequency $1/\tau_{LR} = R_n/L_{Ring}$ and the corresponding characteristic frequency ω_{LR} for a superconducting hybrid ring modelled as shown in Figure A.1(c) as a lumped element with ohmic resistance R_n and inductance L_{Ring}.

the performance of the hybrid cannot be excluded - given the lumped-element model can be applied.

This influence on the performance is due to the following mechanism: The supercurrent I_s contributing to a non-negligible extend to the total current I is unequally split into currents $I_{L,s}$ and $I_{R,s}$, such that the total flux Φ_s through the ring due to the supercurrent remains constant and equal to $n \cdot \Phi_0$. Thus, the ratio of $I_{L,s}$ and $I_{R,s}$ should be equal to the inverse ratio of the corresponding distances on the ring between ports 1 and 3, i.e.: $I_{L,s}/I_{R,s} = 2/1 \Rightarrow I_{L,s} = 2/3 \cdot I_s$ and $I_{R,s} = 1/3 \cdot I_s$. However, to get maximum isolation between port 1 and 3 at the operating frequency, $I_{L,s}/I_{R,s}$ should be 1. In this way, the performance of the hybrid would be reduced.

However, the lumped element representation is not completely valid for the hybrid ring driven at the operation frequency, since then, the structure dimensions *are* in the order of the wavelength λ, namely the circumference of the ring is $3\lambda/2$. As the wavelength is in the order of the ring dimension, it is very hard to predict the exact influence of fluxoid or flux quantization on the operability of the hybrid ring. A complete theoretical calculation or numerical simulation of the S-parameters around the working frequency of the hybrid ring taking into account the condition of fluxoid quantization is quite challenging as it should be based on the general Maxwell equations together with the fluxoid quantization, resulting in a system of inhomogeneous partial differential equations. In this case, near or far field approximations can not be applied and one would probably try to approach the problem analogous to the concept of retarded potentials for the generalized Maxwell equations (see e.g. [64]). The use of retarded potentials as a particular solution of inhomogeneous differential equations is convenient for complicated situations in which the fact of a finite speed of wave propagation c becomes important: In this situation, a potential at position $\vec{r}$ and time t has to be calculated regarding the source of the potential at any point $\vec{r}'$ at an *earlier* time $t - |\vec{r} - \vec{r}'|/c$.

Since presently an influence of the fluxoid quantization on the operability of the hybrid cannot be excluded, it would be advisable to repeat the measurements with a hybrid ring made out of a non-superconducting material like e.g. gold.

Appendix B

Technical drawings

Within this work, several devices have been constructed and machined in the WMI workshop. Their technical drawings are shown in this appendix.
The 2” chuck shown in B.1 and B.2 and the mask holder shown in Figure B.4 extends the mask aligner MJB3 (Karl Süss GmbH) in a way that big structures for substrates up to 2” can be handled.
With the spin-coater carriers B.6 and B.5, substrates with dimensions 20.4 mm x 15 mm and 20 mm x 43 mm respectively may be spin-coated in a comfortable way, reducing edge beads as the substrate surface coincides with the surface of the carriers.
The drawings in B.8 to B.11 finally show two sample holders. One for substrates with planar 2-port microwave structures, the other one for planar 4-port microwave structures. The substrates which can be inserted in these sample holders have to have dimensions of 20.4 ± 0.1 mm$\times15.0\pm0.1$ mm$\times$ 0.5 ± 0.05 mm. The tolerances given here are already at the limit of what can be produced cost-effectively (meaning without too much waste)[1]. Even stricter tolerances are necessary for the sample holders, which are already at the limit of the fabrication capability of the WMI workshop. As the achievable accuracy of the substrate dimensions is below the achievable accuracy of the sample holder, the dimensions of the sample holders have been adapted to those of the substrates. The narrow tolerances are in principle due to the strict tolerances imposed by the high demands of the ANRITSU V-Connectors [2]. Unless future measurements are not performed at mK-Temperatures, it is recommended to machine sample holders from brass as its swarf (*dt. Span*) properties allow much better surface qualities and thus narrower machining tolerances.

---

[1] Hugo Schlich, Matek GmbH, http://www.mateck.com, private communication

[2] Anritsu GmbH, http://www.anritsu.de/

B.1 2” Chuck for Mask Aligner MJB3 (Karl Süss GmbH)

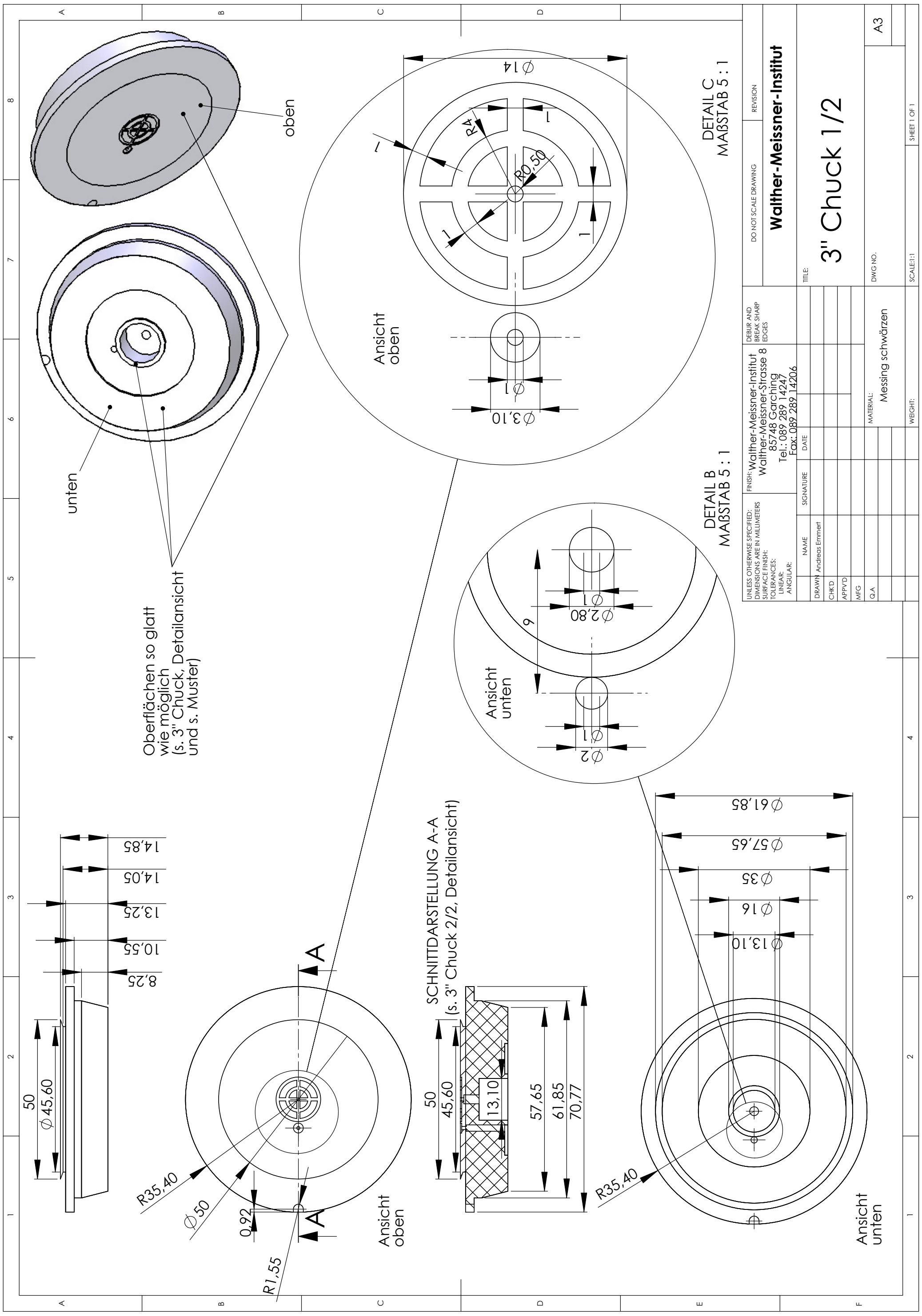

B.2 Detailed View of the 2” Chuck

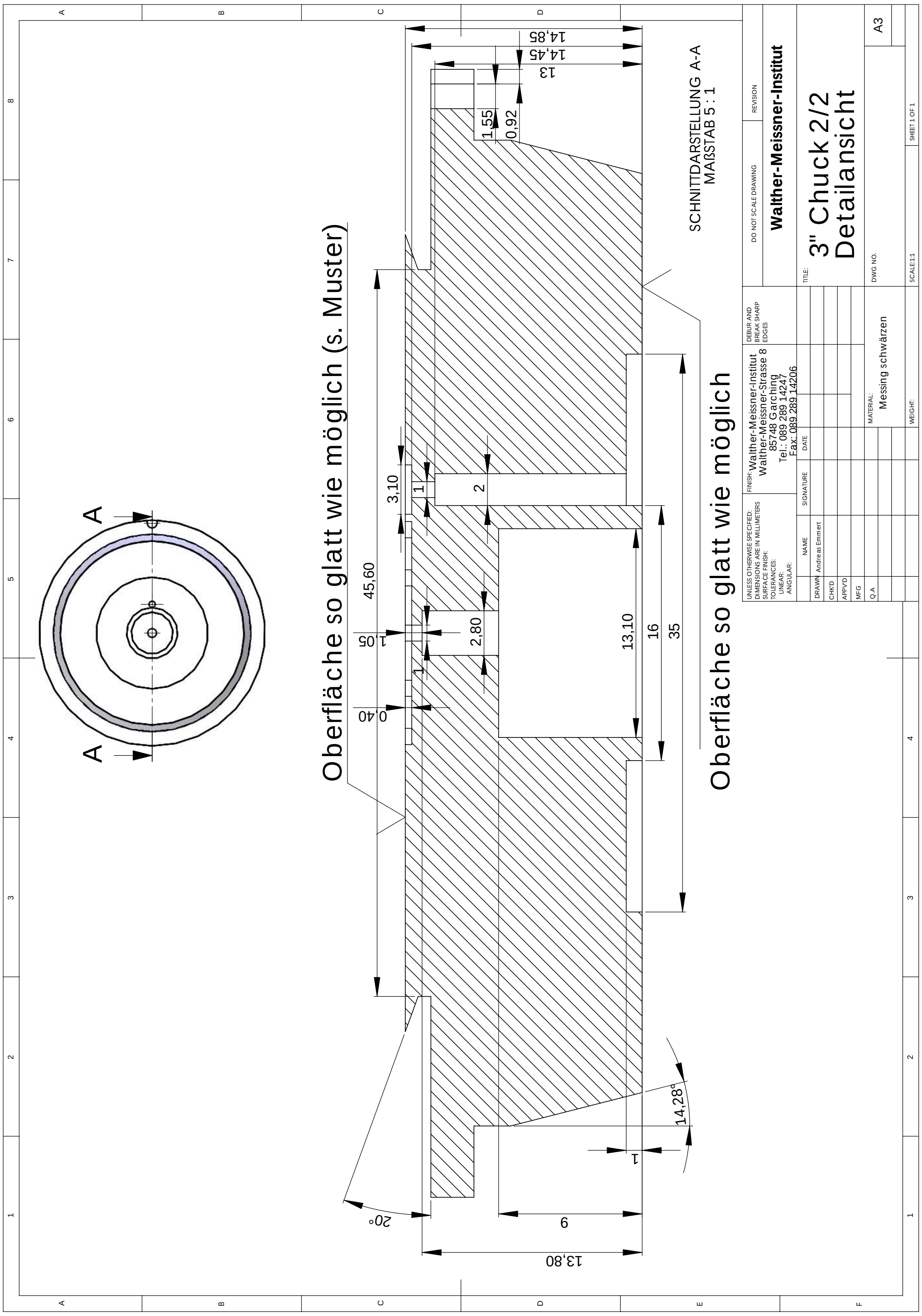

B.3 Photograph of 2” Chuck

B.4 Photograph of Mask Holder for Structures up to 20 × 43 mm^2

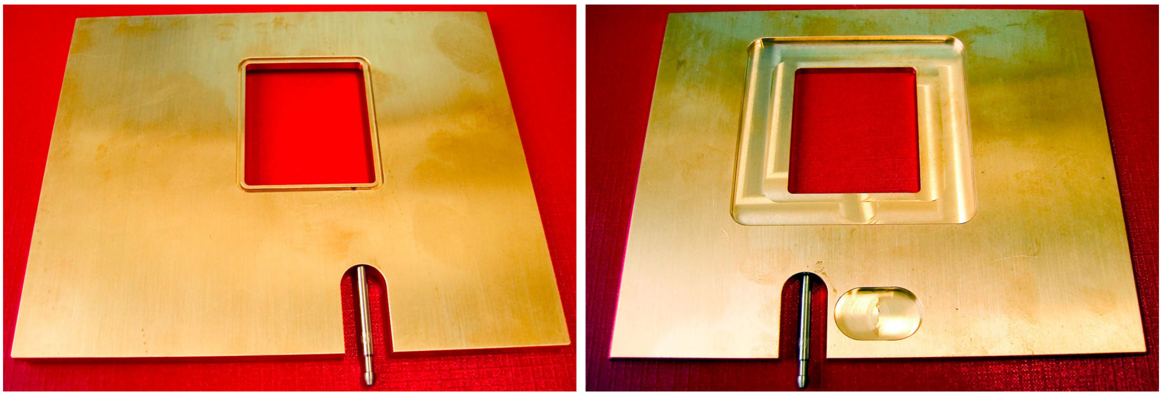

B.5 Carrier for Spin-Coater for Substrates 20 mm x 43 mm

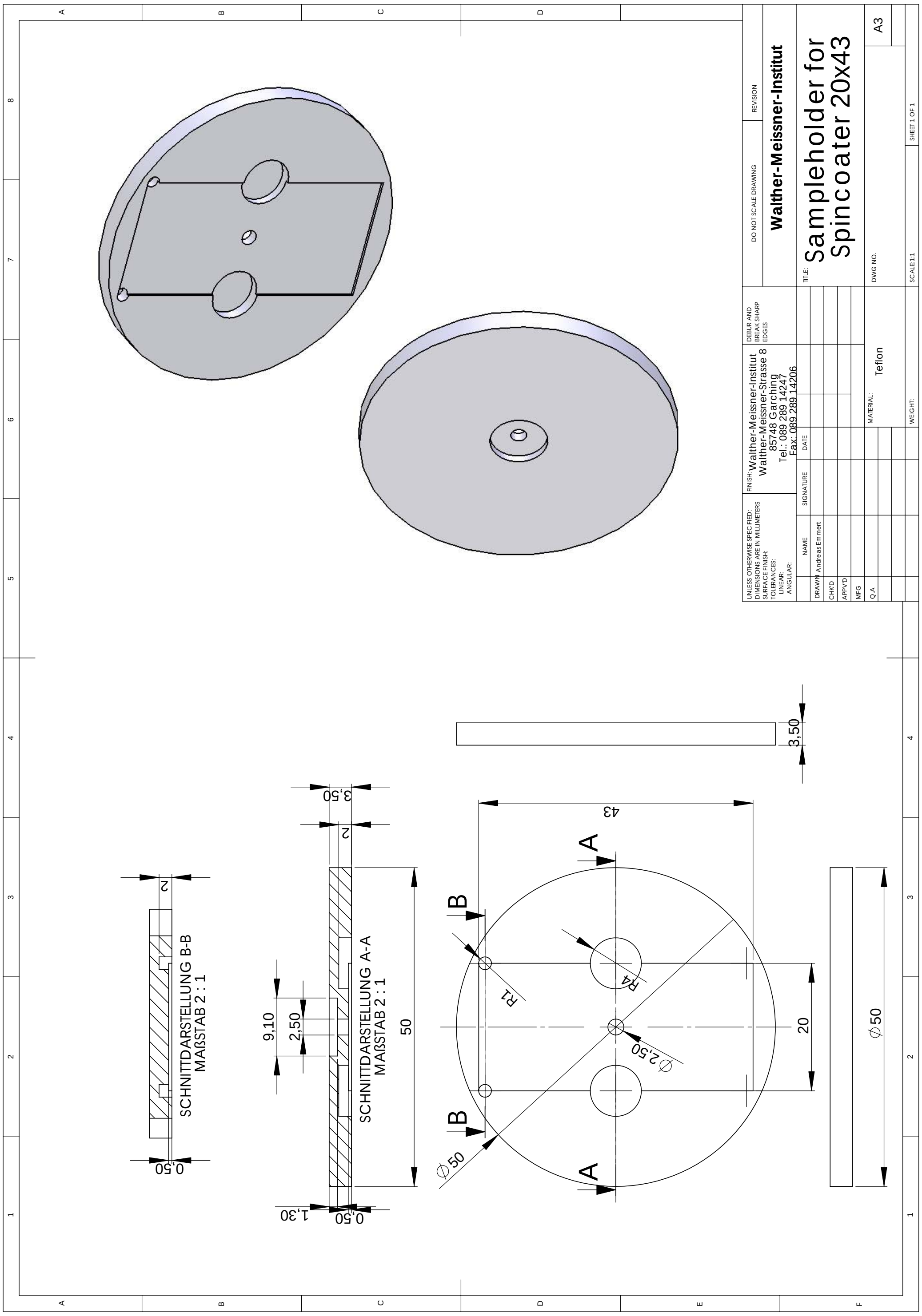

B.6 Carrier for the Spin-Coater for Substrates 20.4 mm x 15 mm

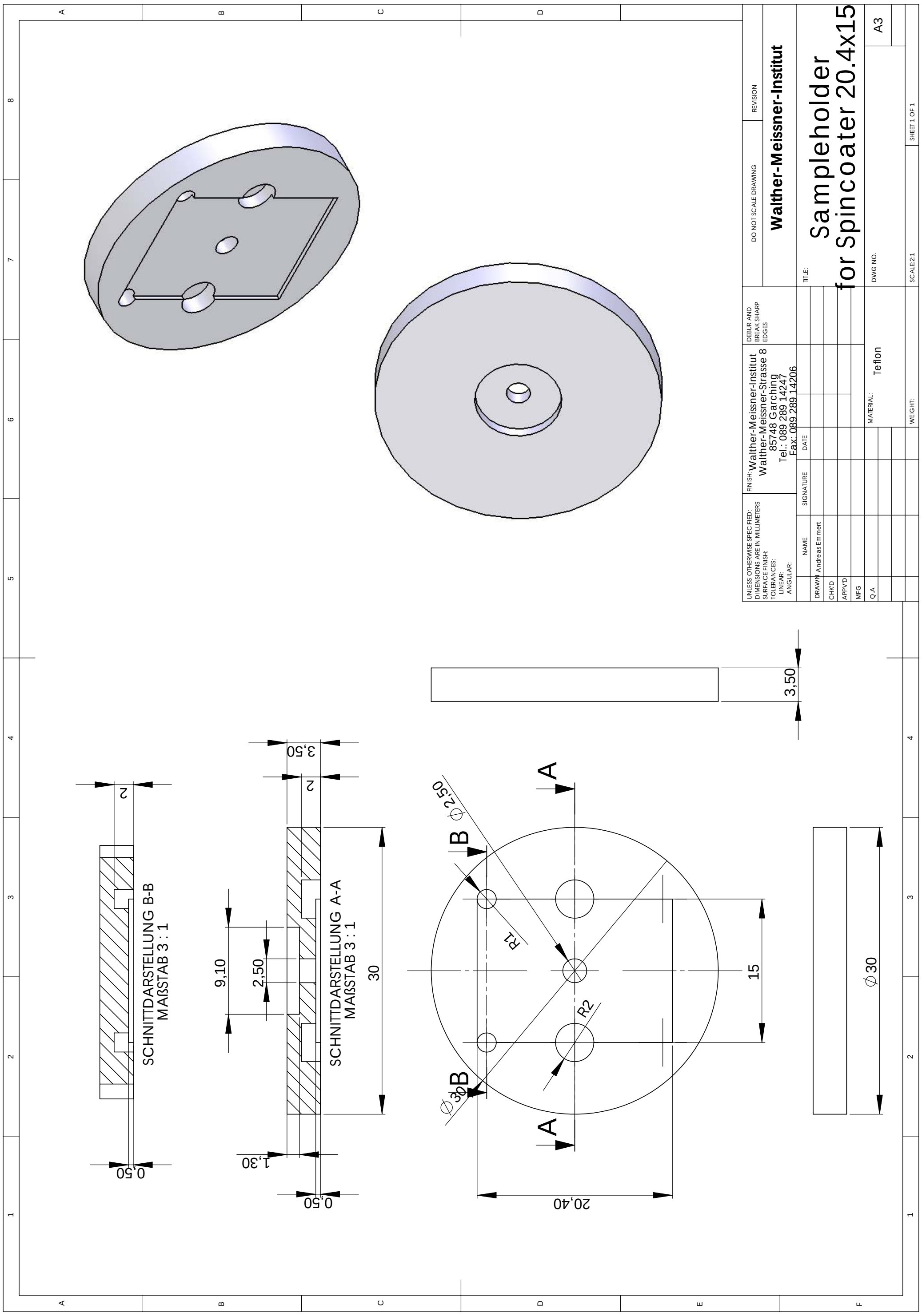

B.7 Carrier for EVAP for Substrates 20 mm x 43 mm

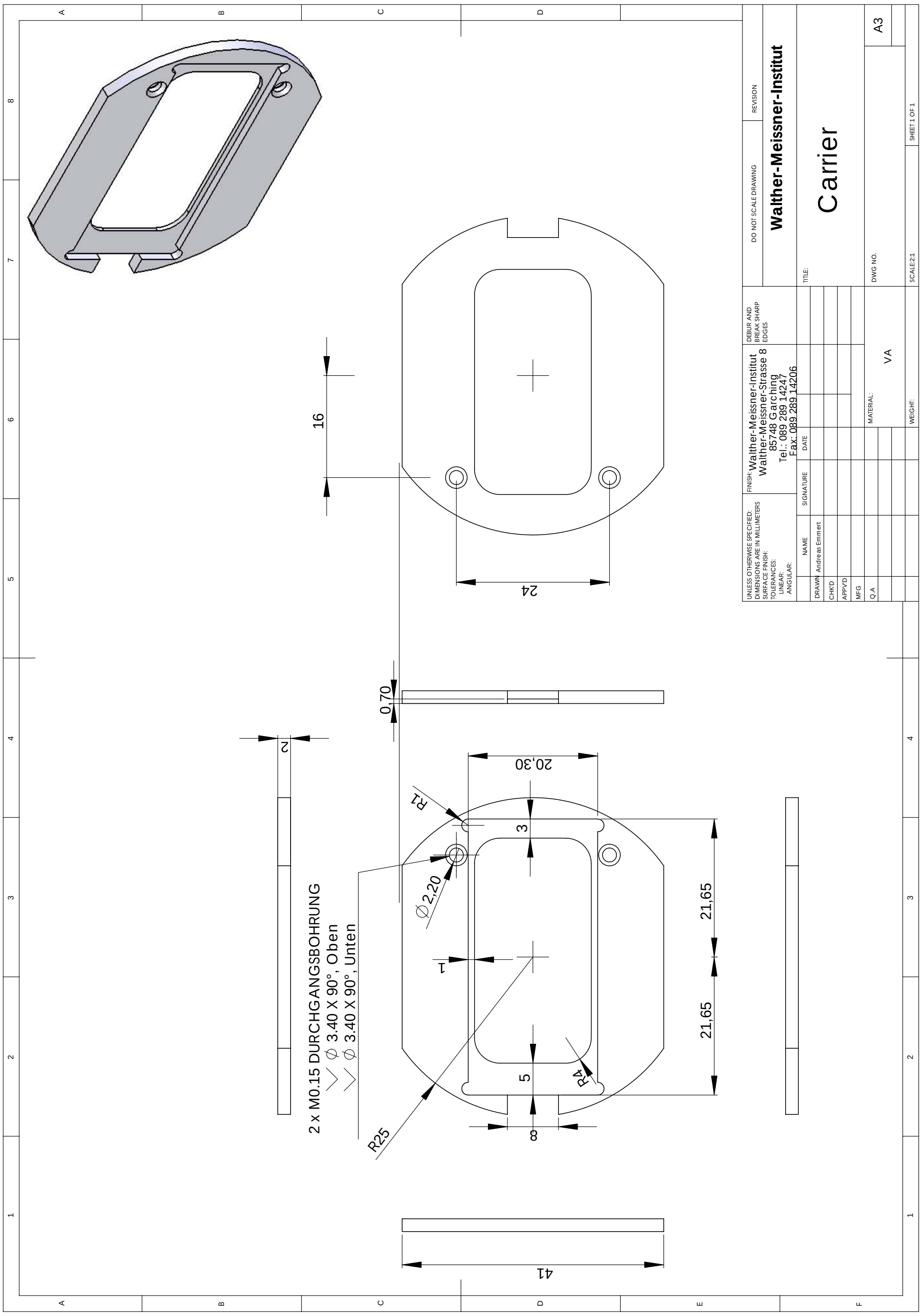

B.8 Sample Holders for 2-Port and 4-Port Devices

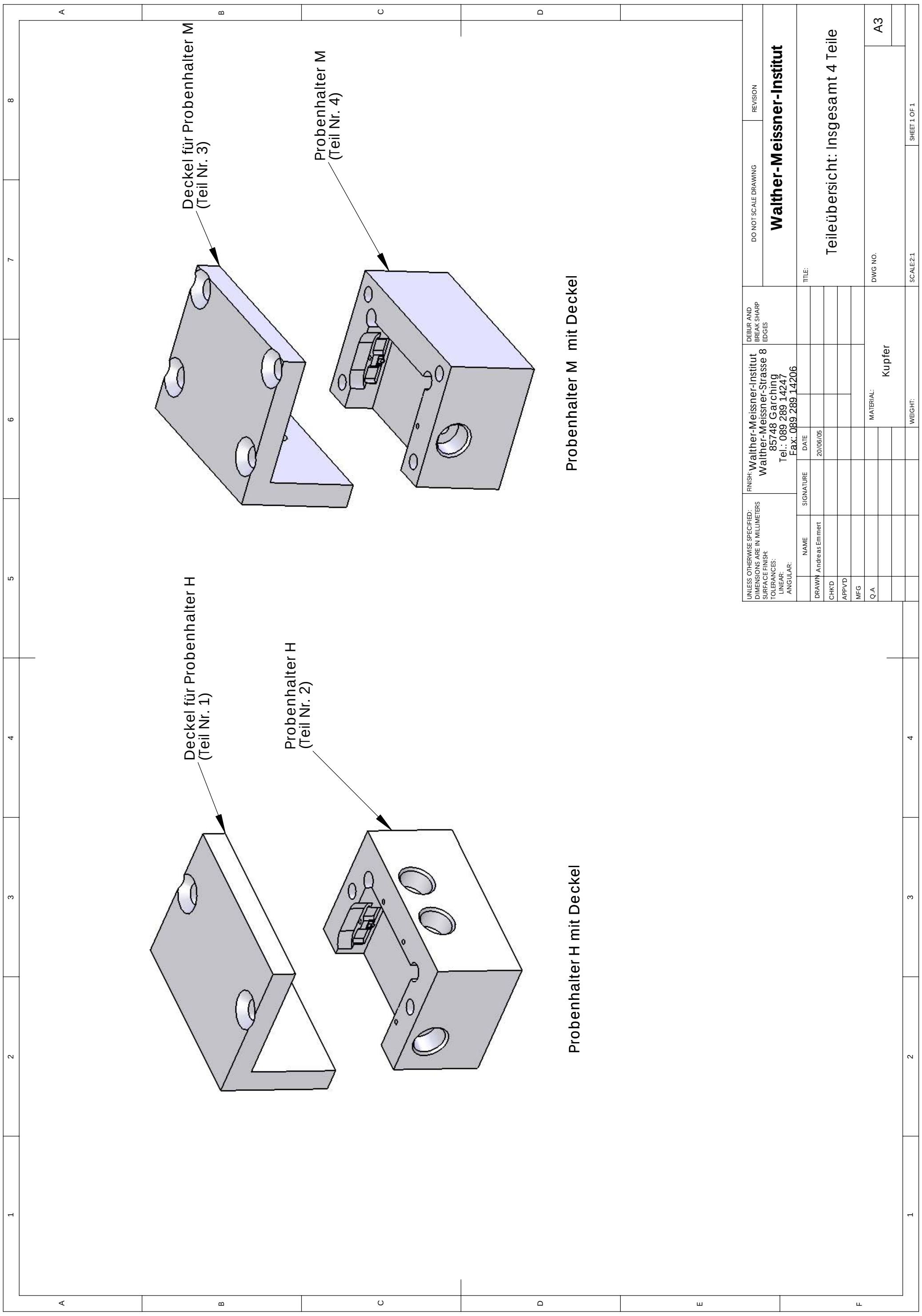

B.9 Sample Holder for 4-Port Devices (20.4 mm x 15 mm)

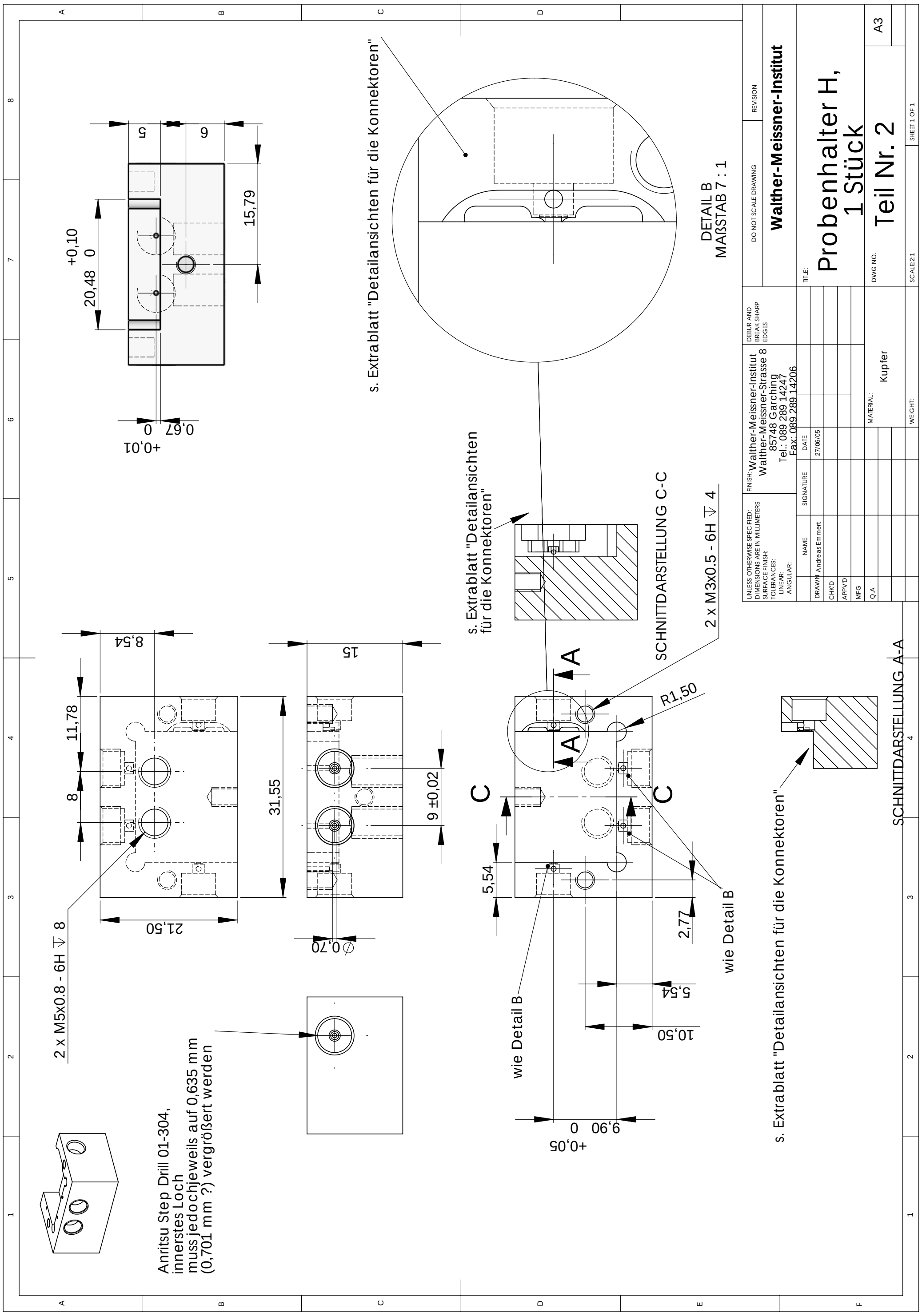

B.10 Sample Holder for 2-Port Devices (20.4 mm x 15 mm)

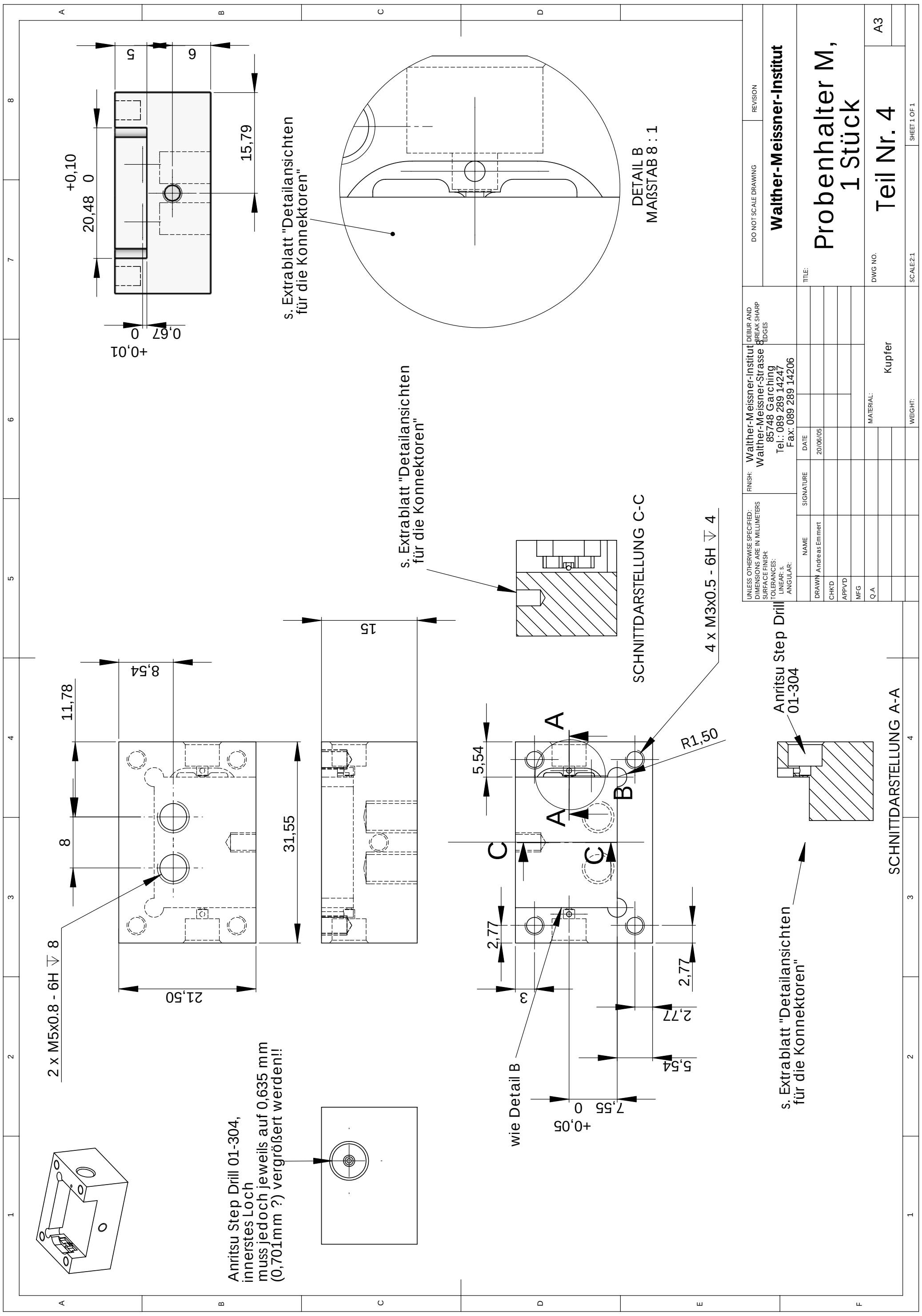

B.11 Detailed View of Connector Boreholes of Parts B.9 and B.10

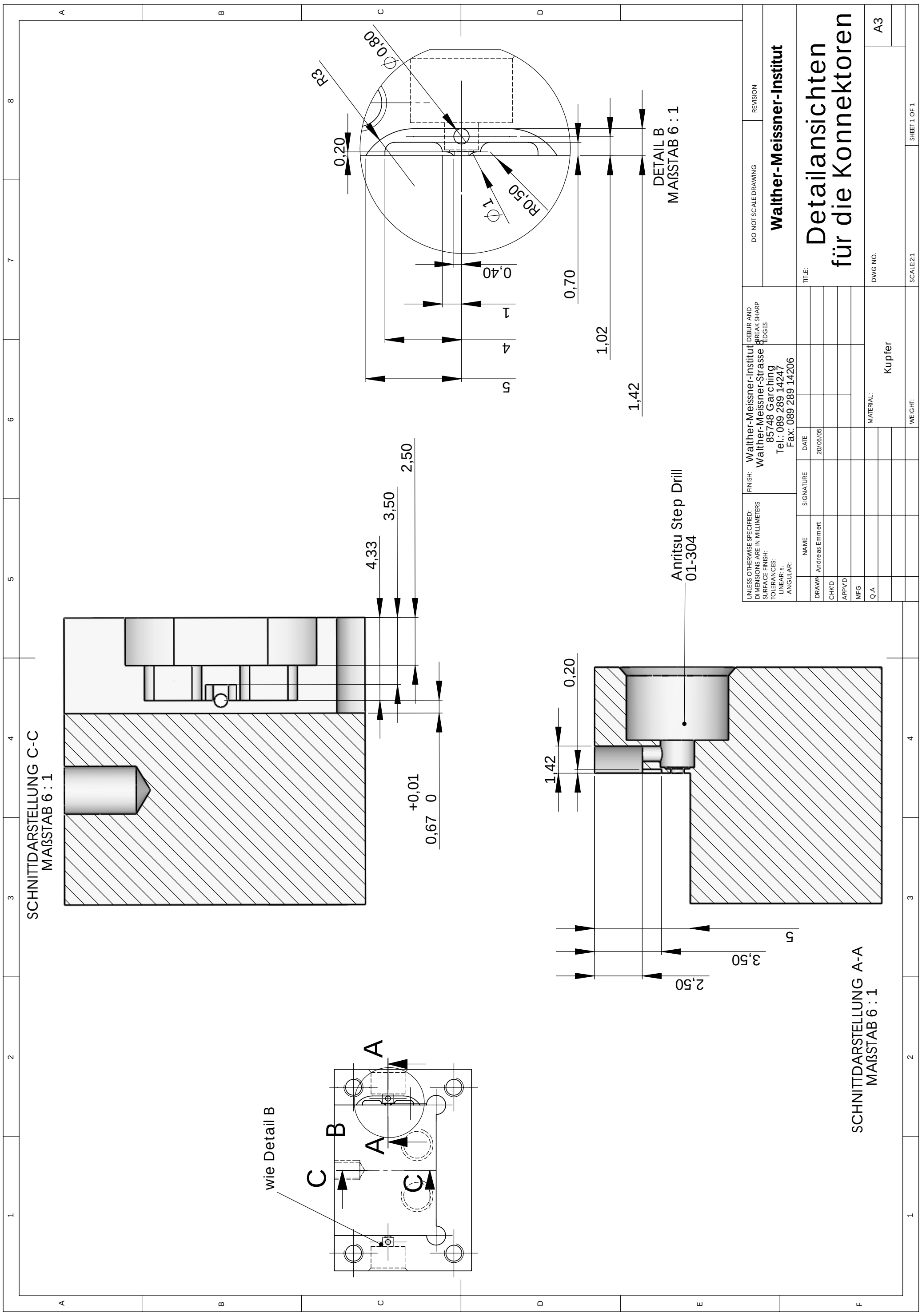

B.12 Detailed View of Top Metal Enclosure of Part B.9

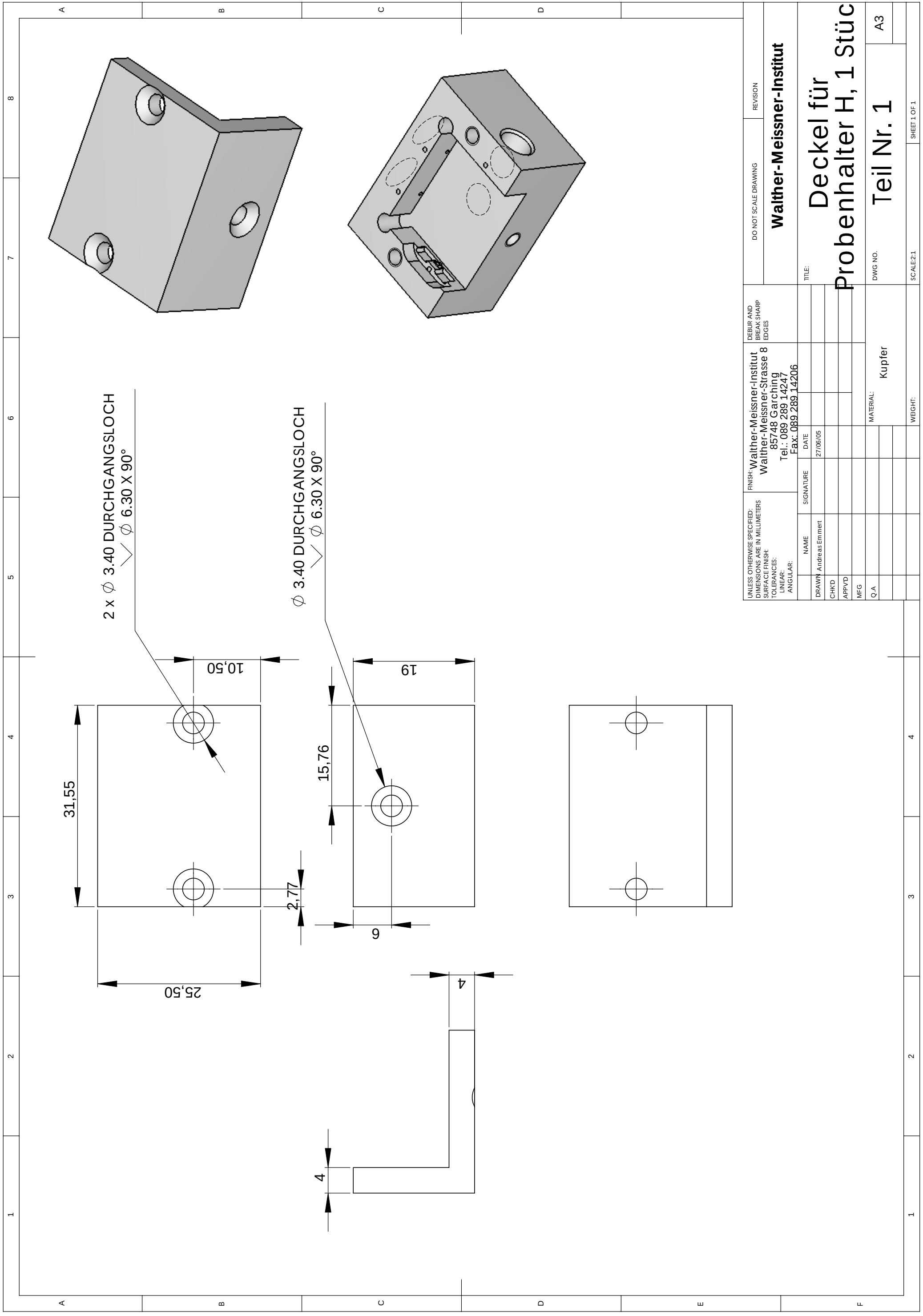

Bibliography

[1] Gross, R. & Marx, A. *Applied Superconductivity: Josephson Effect and Superconducting Electronics* (http://www.wmi.badw.de/E23/ lehre/skript/index.html, (Walther-Meissner-Institut, Garching b. München), 2006).

[2] Ou, Z. Y. & Mandel, L. Derivation of reciprocity relations for a beam splitter from energy balance. *Am. J. Phys.* **57**, 66 (1989).

[3] Collin, R. E. *Foundations for Microwave Engineering, Second Edition* (Wiley-IEEE Press, (New Jersey), 2000).

[4] Pozar, D. M. *Microwave Engineering, Third Edition* (John Wiley & Sons, Inc., (New York), 2005).

[5] Orlando, T. & Delin, K. *Foundations of Applied Superconductivity* (Addison-Wesley Publishing Company, (Reading, MA), 1990).

[6] London, F. & London, H. *Proc. Roy. Soc. London A* **149**, 71 (1935).

[7] *Annalen der Physik* **1**, 566 (1900).

[8] *Annalen der Physik* **3**, 369 (1900).

[9] Tinkham, M. *Introduction to Superconductivity* (Dover Publications, Inc., Mineola, New York, 1996).

[10] Wilker, C., Shen, Z.-Y. & ans M. S. Brenner, V. X. N. A sapphire resonator for microwave characterization of superconducting thin films. *IEEE Trans. Appl. Supercond.* **3**, 1457 (1993).

[11] Maxfield, B. W. & McLean, W. L. *Phys. Rev.* **139**, A1515 (1965).

[12] Ramo, S., Whinnery, J. & v. Duzer, T. *Fields and Waves in Communication Electroncis, Third Edition* (John Wiley & Sons, Inc., (New York), 1994).

[13] Matthaei, G. L., Young, L. & Jones, E. M. T. *Micorwave Filters, Impedance-Matching Networks, and Coupling Strucutres* (Artech House Books, (Dedham, Mass.), 1980).

[14] Mirshekar-Syahkal, D. Impedance calculations for modified coplanar waveguides. *Int. J. Electron.* **44**, 979 – 984 (1996).

[15] Mirshekar-Syahkal, D. *Spectral Domain Method for Microwave Integrated Circuits* (John Wiley & Sons, Inc., (New York), 1991).

[16] Hanington, R. F. *Field Computation by Moment Methods. Reprinted by IEEE Press, 1993* (Macmillan, (New York), 1968).

[17] Company, H.-P. Understanding the fundamental principles of vector network analysis. *Hewlett-Packard Application Note* **1287-1** (1999).

[18] Company, H.-P. Exploring the architectures of network analyzers. *Hewlett-Packard Application Note* **1287-2** (1999).

[19] Simons, R. N. *Coplanar Waveguide Circuits, Components, and Systems* (John Wiley & Sons, Inc., (New York), 2001).

[20] Frazita, R. F. *Transmission line properties of coplanar parallel strips on a dielectric sheet*. Master's thesis, Polytechnic Institute of Brooklyn, N. Y. (1965).

[21] Wen, C. P. Coplanar Waveguide: A surface strip transmission line suitable for non-reciprocal gyromagnetic device applications. *IEEE* **17**, 1087–1090 (1969).

[22] Spickermann, R. & Dagli, N. Experimental analysis of millimeter wave coplanar waveguide slow wave structures on gaas. *IEEE Trans. Microw. Theory Tech.* **42**, 1918–1924 (1994).

[23] Milanovic, V. *et al.* Characterization of broad-band transmission for coplanar waveguides on CMOS silicon substrates. *IEEE Trans. Microw. Theory Tech.* **42**, 632–640 (1998).

[24] Herrick, K., Schwarz, T. & Katehi, L. Si-micromachined coplanar waveguides for use in high-frequency circuits. *IEEE Trans. Microw. Theory Tech.* **46**, 762–768 (1998).

[25] Dehe, A., Klingbeil, H., Weil, C. & Hartnagel, H. Membrane supported coplanar waveguides for mmic and sensor application. *IEEE Microw. Guided Wave Lett.* **46**, 762–768 (1998).

[26] Browne, J. Membrane supported coplanar waveguides for mmic and sensor application. *Microwaves RF* **28**, 137–138 (1989).

[27] Ghione, G. & Naldi, C. U. Coplanar waveguides for mmic applications: Effects of upper shielded, conductor backing, finite-extent ground planes, and line-to-line coupling. *IEEE Trans. Microw. Theory Tech.* **35**, 260–267 (1987).

[28] Wallraff, A. *et al.* Strong coupling of a single photon to a superconducting qubit using circuit quantum electrodynamics. *Nature* **431**, 162–167 (2004).

[29] Hanna, V. & Thebault, D. Theoretical and experimental investigation of asymmetric coplanar waveguides. *IEEE Trans. Microw. Theory Tech.* **32**, 1649–1651 (1984).

[30] Bedair, S. & Wolff, I. Fast, accurate and simple approximate analytic formulas for calculating the parameters of supported coplanar waveguides for (m)mics. *IEEE Trans. Microw. Theory Tech.* **40**, 41–48 (1992).

[31] Kiang, J. F. Fast, quasi-TEM analysis of coplanar waveguides with an inhomogeneous semiconductor substrate. *IEEE Trans. Microw. Theory Tech.* **40**, 1586–1589 (1996).

[32] Fang, S. & Wang, B. Analysis of asymmetric coplanar waveguide with conductor backing. *IEEE Trans. Microw. Theory Tech.* **47**, 238–240 (1999).

[33] Veyres, C. & Hanna, V. Extension of the application of conformal mapping techniques to coplanar lines with finite dimensions. *Int. J. Electron.* **48**, 47–56 (1980).

[34] Knorr, J. & Kuchler, K. Analysis of coupled slots and coplanar strips on dielectric substrate. *IEEE Trans. Microw. Theory Tech.* **23**, 541–548 (1975).

[35] Davies, J. & Syahkal, D. Spectral domain solution of arbitrary coplanar transmission lines with multilayer substrate. *IEEE Trans. Microw. Theory Tech.* **25**, 143–149 (1977).

[36] Cheng, K. & Robertson, I. Numerically efficient spectral domain approach to the quasi-TEM analysis of supported coplanar waveguide structures. *IEEE Trans. Microw. Theory Tech.* **42**, 1958–1965 (1994).

[37] Schroeder, W. & Wolff, I. Full-wave analysis of the influence of conductor shape and structure details on losses in coplanar waveguide. *IEEE MTT-S Int. Microwave Symp. Dig.* **3**, 1273–1276 (1995).

[38] v. Duzer, T. & Turner, C. W. *Principles of superconducive devices and circuits* (Edward Arnold, (London), 1981).

[39] Haydl, W. H., Kitazawa, T., Braunstein, J., Bosch, R. & Schlechtweg, M. Millimeter-wave coplanar transmission lines on gallium arsenide, indium phosphide and quartz with finite metalization thickness. *IEEE MTT-S Int. Microwave Symp. Digest* **2**, 691 – 694 (10 - 14 June 1991).

[40] Rauch, W. *et al.* Microwave properties of $YBa_2Cu_30_{7-x}$ thin films studied with coplanar transmission line resonators. *J. Appl. Phys.* **73**, 1866–1872 (1993).

[41] Kyocera International, I. *Characteristic of Kyocera Fine Ceramics (I)* ((http://americas.kyocera.com/kicc/industrial/substrates.html), 2005).

[42] Booth, J. C. & Holloway, C. L. Conductor loss in superconducting planar structures: calculations and measurements. *IEEE Trans. Microw. Theory Tech.* **47**, 769 (1999).

[43] Holloway, C. L. & Kuester, E. F. A quasi-closed form expression for the conductor loss of cpw lines, with an investigation of edge shape effects. *IEEE Trans. Microw. Theory Tech.* **43**, 2695 (1995).

[44] Frunzio, L., Wallraff, A., Schuster, D., Majer, J. & Schoelkopf, R. Fabrication and characterization of superconducting circuit QED devices for quantum computation. *IEEE Trans. Appl. Supercond.* **15**, 860 (2005).

[45] Krupka, J. *Dielectric measurements on low-loss materials* (Instytut Mikroelektroniki i Optoelektroniki PW, (Warszawa, Poland), 2002).

[46] Hasnain, G., Dienes, A. & Whinnery, J. Dispersion of picosecond pulses in coplanar transmission lines. *IEEE Trans. Microw. Theory Tech.* **34**, 738 (1986).

[47] Alessandri, F., Goebel, U., Melai, F. & Sorrentino, R. Theoretical and experimental characterization of nonsymmetrically shielded coplanar waveguides for millimeter-wave circuits. *IEEE Trans. Microw. Theory Tech.* **37**, 2020 (1989).

[48] Kessler, J., Dill, R. & Russer, P. Field theory investigation of high-T_c superconducting coplanar waveguide transmission lines and resonators. *IEEE Trans. Microw. Theory Tech.* **39**, 1566 (1991).

[49] Qian, Y., Yamashita, E. & Atsuki, K. Modal dispersion control and distortion suppression of picosecond pulses in suspended coplanar waveguides. *IEEE Trans. Microw. Theory Tech.* **40**, 1903 (1992).

[50] Wallraff, A. *et al.* Approaching Unit Visibility for Control of a Superconducting Qubit with Dispersive Readout. *Phys. Rev. Lett.* **95**, 060501 (2005).

[51] Applied Wave Research, I. *Microwave Office 2002 (MWO-228)* **Version 5.01**.

[52] CST. *CST Microwave Studio* **Version 5.0.0** (January 2004).

[53] Weiland, T. A discretization method for the solution of maxwell's equations for six-component fields. *Electronics and Communication, (AE)* **31**, 116–120 (1977).

[54] Weiland, T. Time domain electromagnetic field computation with finite difference methods. *International Journal of Numerical Modelling* **9**, 295–319 (1996).

[55] Bazdar, M., Djordjevic, A., Harrington, R. & Sarkar, T. Evaluation of quasi-static matrix parameters for multiconductor transmission lines using galerkin's method. *IEEE Trans. Microw. Theory Tech.* **MTT-42**, 1223–1228 (1994).

[56] Lev, B. L. *Magnetic Microtraps for Cavity QED, Bose-Einstein Condensates, and Atom Optics*. Master's thesis, California Institute of Technology, Pasadena, California (2006).

[57] GmbH, M. *Company Homepage* (http://www.microchemicals.com, (Ulm), 2006).

[58] Company, H.-P. In-fixture measurements using vector network analyzers. *Hewlett-Packard Application Note* **1287-9** (1999).

[59] Company, H.-P. Applying error correction to network analyzer measurements. *Hewlett-Packard Application Note* **1287-3** (1999).

[60] Scarpa, G. & Lugli, P. Discussion about recent numerical simulations on CWG hybrid ring structures. *private communication* (2006).

[61] Mariantoni, M. *et al.* Generation of Microwave Single Photons and Homodyne Tomography on a Chip. *submitted to Phys. Rev. Lett., cond-mat/0509737* (2005).

[62] Doll, R. & Näbauer, M. Experimental proof of magnetic flux quantization in a superconducting ring. *Phys. Rev. Lett.* **7**, 51–52 (1961).

[63] Deaver, B. & Fairbank, W. Experimental evidence for quantized flux in superconducting cylinders. *Phys. Rev. Lett.* **7**, 43–46 (1961).

[64] Jackson, J. *Classical electrodynamics* (John Wiley & Sons, Inc., (New York, N.Y.), 1999, 3rd ed.).

Acknowledgements

An dieser Stelle möchte ich all denjenigen danken, die in direkter oder indirekter Weise zum Gelingen dieser Diplomarbeit beigetragen haben.
Bei *Prof. Dr. R. Gross* möchte ich mich bedanken, weil er mir die Gelegenheit gegeben hat, diese Arbeit am Walther-Meissner-Institut anzufertigen. Die Arbeitsbedingungen waren hervorragend. Ich hatte im nagelneuen Büro fast mehr Platz als bei mir Daheim. Auch möchte ich Prof. Gross danken für die unzähligen Gutachten, die er mir widerstandslos angefertigt hat.
Dr. Achim Marx danke ich für das Korrekturlesen meiner Diplomarbeit. Seine Hinweise in Sachen Layout, English und die leidige Frage ”to be *k*ursiv or not kursiv?” haben mir sehr viel geholfen. Es war mir ein Vergnügen, mit ihm in ”seiner” Qubit-Gruppe zu arbeiten.
Es war *Matteo Mariantoni* [3], der mich für circuit-CQED begeistern konnte. Das lag nicht zuletzt an seiner kommunikativen Art, mit der er es auch geschafft hat, neue spannende Kollaborationen mit anderen Gruppen zu initiieren, aus denen schließlich auch ein Paper herangewachsen ist.
Georg Wild danke ich, weil er mir weitergeholfen hat, wann immer ich Probleme in experimenteller Hinsicht hatte. So hat er etliche Stunden mit mir an der PLD verbracht, geröntgt und gereinraumt.
Gleiches gilt für Thomasz Niemczyk, der mich tatkräftig unterstützt hat, wann immer ich zeitliche Engpässe zu überwinden hatte. Nachdem wir schon Schulzeit, Studium und Diplomarbeit miteinander verbracht haben, hoffe ich nun, dass wir wenigstens unterschiedliche Frauen heiraten werden.
Renke Stolle und Dr. Dieter Andres danke ich für das angenehme Büroklima, das sie zu verbreiten wussten. So konnte ich viel lernen über Freizeitfußball, Marathon und durchzechte Nächte. Marwan Abbas hat uns Jordanien ein Stück näher gebracht.
Für die unterhaltsamen Reinraumgespräche oft bis tief in die Nacht möchte ich mich bei Martin Göppl bedanken.
Kompetente Ansprechpartner bei der Konstruktion des Zoos von Probenhaltern in dieser Arbeit waren Thomas Brenninger, Robert Müller, Helmut Thies und Christian Reichlmeier, wobei letzterer die Probenhalter – aller Widrigkeiten zum Trotz – mit Bravour herstellen konnte.
Zum Ablauf des Forschungsbetriebs tragen die Mitarbeiter des WMI ganz wesentlich bei. Besonders möchte ich mich bedanken bei Dr. Christian Probst, der stets ein offenes Ohr für mich hatte, wenn es um kalte Angelegenheiten ging. Ulrich Guggenberger für das Leihen

---

[3] Ti scrivo in tedesco così finalemente ti verrà la voglia di impararlo!

seiner Literatur in Sachen Elektrotechnik. Dieter Guratzsch für die Hilfe bei meinen Computerproblemen. Joachim Geismann – dem selbsternannten Mädchen für Alles – für Alles. Gabrielle Görblich für die Reinraumutensilien. Bei Brigitte Steinberg und Sybilla Plöderl möchte ich mich für den Saustall entschuldigen, den ich mit meinen Apfelschorleflaschen fabriziert habe.

Danken möchte ich auch meinen (Ex-) FreundenInnen dafür, dass sie meine schlechte Laune in den Prüfungsperioden ertragen haben und mich auch dann nicht vergessen haben, wenn ich tagelang wie vom Erdboden verschwunden schien. Merci bien pour ta comprhension et ton soutien, Grazi.

Dass ich überhaupt erst so weit gekommen bin, eine Diplomarbeit anfertigen zu können, lag ganz eindeutig an meiner Familie. Besonders hervorheben möchte ich meinen Bruder, in dessen Windschatten es sich so viel einfacher leben lässt. Wie viel Josef an meinen Erfolgen in Schule und Studium teilhatte, musste ich in den letzten Wochen meiner Diplomarbeit erfahren. Wie wichtig Menschen sind, merkt man leider erst oft dann, wenn sie einem fehlen.

Erklärung

des Diplomanden

Name: Emmert

Vorname: Andreas

Mit der Abgabe der Diplomarbeit versichere ich, dass ich die Arbeit selbständig verfasst und keine anderen als die angegebenen Quellen und Hilfsmittel benutzt habe.

München, den 21.Februar 2006

(Ort, Datum)

A. Emmert
....
(Unterschrift)